Printed Biodegradable Wireless Soil Nitrate Sensor Nodes

Carol Baumbauer

Electrical Engineering and Computer Sciences
University of California, Berkeley

Technical Report No. UCB/EECS-2023-57
http://www2.eecs.berkeley.edu/Pubs/TechRpts/2023/EECS-2023-57.html

May 1, 2023

Printed Biodegradable Wireless Soil Nitrate Sensor Nodes

by

Carol L. Baumbauer

A dissertation submitted in partial satisfaction of the

requirements for the degree of

Doctor of Philosophy

in

Electrical Engineering and Computer Science

in the

Graduate Division

of the

University of California, Berkeley

Committee in charge:

Professor Ana Claudia Arias, Chair
Professor Kris Pister
Professor Whendee Silver

Summer 2022

Printed Biodegradable Wireless Soil Nitrate Sensor Nodes

Abstract

Printed Biodegradable Wireless Soil Nitrate Sensor Nodes

by

Carol L. Baumbauer

Doctor of Philosophy in Electrical Engineering and Computer Science

University of California, Berkeley

Professor Ana Claudia Arias, Chair

Precision agriculture is a set of practices that seek to measure and understand different conditions in space and time across a field, in order to manage water and fertilizer efficiently. Precision agriculture requires high spatial and temporal resolution data, which comes from sensors. However, lack of simple, inexpensive, unobtrusive, low-maintenance sensors that can be widely distributed across a field is a challenge for precision agriculture producers. This thesis describes work towards a network of printed, biodegradable, wireless soil nitrate sensors to meet this need. Sensor nodes consist of potentiometric nitrate sensors, passive UHF-RFID antennas, and a silicon chip to manage power and data communication. Over 95% of the mass of the node is biodegradable.

The thesis includes a discussion of each part of the sensor stake. Fabrication techniques for biodegradable substrates, conductors, and encapsulants are discussed. A room-temperature process for printing highly conductive zinc on wood using beeswax encapsulants is a key enabling process. Nitrate sensor operation and development are described, and impacts of using biodegradable materials in nitrate sensors are explored. I show the design, fabrication, and testing of compact RF antennas, and discuss modifications which are required when using biodegradable materials. The printed antennas are integrated with silicon integrated circuits to form passive RFID tags. Requirements and challenges for integrating printed potentiometric sensors with these tags are also discussed. Finally, the impacts of field-deployment are explored. This includes materials lifetime characterization, measuring nitrate sensors in field soils, and validating passive RFID communication in growing crops.

Contents

List of Figures

List of Tables

Acknowledgments

This work is the product of many, many collaborations and support from many groups and individuals. Great challenges–such as reducing the environmental impacts of agriculture–involve innovations that happen at the intersections of many fields. The wireless soil sensors presented here are a great example of such innovative collaborations between engineers, materials scientists, manufacturing and design experts, soil scientists, and agriculturalists.

First and foremost, I'd like to thank my advisor, Dr. Ana Arias. Ana is a maestro, bringing together people from different backgrounds, with ideas for projects, and the resources to make them happen. She dreams big, and puts the pieces in place for her students to dream big, and turn those dreams into work on projects that matter to us. Thank you for cultivating the helpful, innovative, impactful group you have.

Another person who has shaped my work more than any other is my collaborator, Payton Goodrich. From the beginning of the agricultural sensors project, we have worked closely together on most parts of the project; prototyping hundreds of ways to process wax, measuring nitrate sensors, and discussion what was working, what wasn't, and how we could improve things. Along the way we've learned from each other, supported each other–Payton fabricated and mailed sensors to me while I was away during COVID, and I characterized them–and combined our complimentary strengths to create work that's stronger than either of us would have produced alone. Besides that, Payton is fun to work with, and reminded me not to take myself so seriously all the time.

My first real project in graduate school was about printed RFID tags. In that area, Arno Thielens was a terrific mentor. I learned not only about antenna design and measurement, but also the paper writing, submission, and revision process by working with Arno. I'd also like to thank our other co-authors on printed RFID tags: Igal Deckman, Jan Rabaey, Jonathan Ting, Matthew Anderson, and Akshay Sreekumar.

My work on antennas also let me get to know the researchers and support staff at the Berkeley Wireless Research Center. Thank you Candy Corpus-Steudeman, Mikaela Cavizo-Briggs, Jeff Anderson-Lee, Brian Richards, and James Dunn for all you do to support research and collaboration at BWRC.

The biodegradable soil sensors nodes work was part of a large collaboration funded by ARPA-e, the advanced research projects initiative in the US Department of Energy. The PI for this work was Greg Whiting at the University of Colorado–Boulder, who, like Ana, is able to dream up nearly impossible technologies and help turn them into reality. Greg's continued confidence in our work was vital to keeping the project going. I collaborated with Greg's students, particularly Madhur Atreya, Anupam

Gopalakrishnan, and Youngkun Sui, on the biodegradable materials side of things, a complicated project which took all of us.

Raj Khosla and his group, including Subash Dahal, Evan Phillippi, Jeff Siegfried, Dipankar Mandal, and Wub Yilma, have provided extremely valuable insights from the agronomic perspective. They have carried out greenhouse testing of materials and sensors, and let us know what sensors need to be able to do in order to be useful in the real world.

At Berkeley, a tremendous team of people have worked on the nitrate sensors. Maggie Payne did the initial groundwork for the sensors, then handed them off to Payton and me when she graduated. Anju Toor also assisted with potentiometric sensor development. Nitrate-in-soils testing has been made possible by collaborators in Berkeley's Environmental Science Policy and Management department–Whendee Silver's group, particularly Tyler Anthony and Claire Beckstoffer

In addition to those already named, the students and postdocs in the Arias group are and have been kind, helpful labmates and creative, innovated researchers. In no particular order, they are: Claire Lochner, Joe Corea, Natasha Yamamoto, Balthazar Lechene, Donggeon Han, Yasser Khan, Maruf Ahmed, Xiaodong Wu, Juan Zhu, Seiya Ono, Jasmine Jan, Karthik Gopalan, Jonathan Ting, Mahsa Sadeghi, Alla Zamarayeva, Natalie Tetrault, Yuhan Wen, and Julian Maravilla. Arias group undergraduates who have worked with me or on agriculture-related projects include: Emma Wawrzynek, Derek Wong, Alyssa Umino, Aashray Manchanda, Nihtila Poongovan. They have also been wonderful collaborators.

The COVID-19 pandemic hit in the middle of my graduate school experience, and created some upheaval, and also some unexpected opportunities. Thank you to the my family members who invited me into your homes for months in 2020 in Saint Paul, MN, and Bozeman, MT!

While I was in Bozeman, I was able to continue research thanks to collaborations with researches at Montana State University. Stephan Warnat hosted me as a visiting scholar, and offered me lab space to characterize nitrate sensors. His students Matthew McGlennen and Michael Neubauer especially welcomed me. The other researchers and support staff at the Center for Biofilm Engineering were incredibly helpful getting me set up with anything I needed.

My time in Bozeman and at MSU also enabled in-greenhouse and in-field experiments thanks to a collaboration with my dad, the first Dr. Baumbauer. Thanks for letting me use space and equipment at the Plant Growth Center and the Horticulture Farm, for helping me measure RFID read range in crops, and taking care of corn plants in the biodegreadation study. Thank you also for teaching me about research in agriculture, and the applications of sensors in that research. I hope we can collaborate again.

Finally, thank you to my teachers. The educators in the Bozeman Public Schools system taught me both technical and non-technical skills I've used every day in graduate school, and launched my on my academic journey. My undergraduate research mentor at Montana State University, Wataru Nakagawa, was and still is a true mentor. Labmates Ethan Keeler and Ben Moon taught me how to work in fabrication, and how to write nice lab reports, skills I've been grateful to have in grad school. Other MSU electrical engineering faculty including David Dickensheets and Joe Shaw also provided mentorship and encouragement along my academic path.

Chapter 1

Introduction

This thesis is about making wireless, passive, biodegradable soil nitrate sensors for precision agriculture. Such sensors could be used to reduce waste in agriculture and help scientists study soil biogeochemical processes. The constituent parts–passive RFID, potentiometric nitrate sensors, and biodegradable electronic material–are useful in a variety of areas as well. In the introduction, background information on technology in agriculture, nitrate in the environment, wireless sensor networks, and biodegradable electronics is presented.

1.1 Precision Agriculture Technology

Agriculture today is a high-tech business. From seeds which are carefully bred for high yield, drought tolerance, or pest-resistance, to GPS-enabled harvesters which produce spatial maps of yield data as they harvest, every step of the growing cycle is touched by technology. Conventional commercial operations are largely shaped by the advances of the Green Revolution of the 1940's and 50's: large monoculture fields, mechanized planters, tillers, and combine harvesters, increased use of herbicides and pesticides, and the substantial application of synthetic fertilizer, particularly to provide nitrogen, phosphorus, and potassium. These advancements increased average US corn yield from 26 bushels/acre in the 1920s to 125 bushels/acre in the early 2000s [1]. The increase in production is a remarkable and needed achievement, but it carries environmental costs. In particular, commercial farming can be inefficient in its use of water and fertilizer. Part of the problem is that conventional agriculture treats one field as a uniform piece of land, but in reality there are significant variations from one part of the field to another, which is evident in the areal color photograph of a 22 acre field in figure 1.1a.

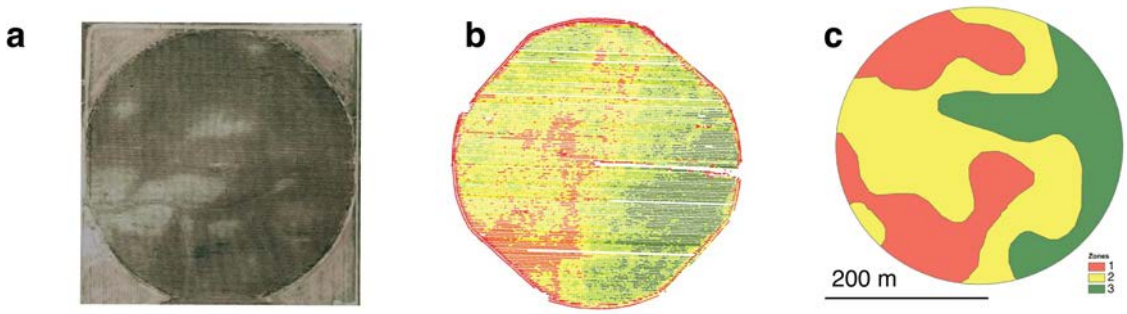

Figure 1.1: a) Variations in field soil and crop conditions are visible through simple color areal photography. b) A yield map is generated as the harvester harvests a crop at the end of the season. Sensors mounted on the harvester estimate yield on-the-go, which is paired with geolocation data from GPS mounted on the harvester. c) Management zones can be drawn to divide areas of the field which will be treated similarly. Historical yield data and soil data are used to designate management zones.

To improve efficiency of large-scale agriculture, the field of Precision Agriculture (PA) has emerged, which is a set of practices that seek to measure and understand temporal and spatial heterogeneity within a field, in order to adjust treatments accordingly [2]. Early PA research and development dates back to the 1980's when researchers studying soil spatial variability took soil core samples every 30 m. In the 1980's and 90's, PA was primarily confined to academic research because the technology was expensive, slow, and labor-intensive. This meant that practices were not profitable and therefore not commercially adopted on a large scale [3]. Significant technological advances in the past 30 years have expanded what is possible with PA. In particular, GPS with meter-scale accuracy, optical remote sensing capabilities, and variable rate technology have made significant impacts.

PA begins with data, which comes from sensors. Recent and ongoing advances in sensing can generate on the order of millions of data points per field per day. All that data is processed either throughout the growing season or after harvest in preparation for the next season. Statistical analyses are run; additionally machine learning algorithms are being developed to find trends in the vast amount of data that can be collected today. Information that comes from data processing is used by growers to inform management practices. Once a decision has been made–for

example, to fertilize at a certain rate on a certain day–equipment such as variable-rate fertilizer sprayers can be used to implement that practice. Each of these steps: sensing, management decisions, and actuation is described in more detail below.

Sensing

Agricultural sensors generally fall into two broad classes: remote and proximal sensors. Remote sensors are optical imagers that rely on reflected sunlight and which are mounted on satellites, airplanes, towers, or unmanned aerial vehicles (UAVs or drones) which are far from the plants and soil. Simple visible-light color images of bare soil provide information on soil texture and organic matter content, while color images of growing crops can be used to spot nutrient deficiencies. Advances in optics have enabled resolution of 40 cm from commercial satellite images, while publicly available Landsat 8 images have 30 m resolution. Quantitative analysis is done using normalized indices: ratios of light intensity between two or three spectral bands. The Normalized Difference Vegetation Index (NDVI) is one widely used index which compares intensity in the red and near-infrared (NIR) bands. Multi-spectral imagers, which divide the optical spectrum into bands of 50 nm wavelength ranges, and hyper-spectral imagers, which have bands of only 10 nm, as well as cameras with extended sensitivity to ultraviolet and infrared wavelengths are providing data for a growing number of indices. These indices are more directly correlated with specific crops, diseases, or deficiencies.

Proximal sensors are ground-based sensors which are located in or near the soil or plants they are measuring. Proximal sensors for plant material are often optical sensors, gathering data at the plant or row scale, rather than the field scale, as remote sensing can do. Commercially available proximal soil sensors measure soil moisture, electrical conductivity (EC) and temperature at a variety of depths, frequencies, and spacial scales using a number of different techniques. Many soil moisture and EC sensors rely on the principle that increasing soil water content increases the relative permittivity of soil, which impacts how electromagnetic waves propagate through the soil and determines the strength and location electric fields created in or near the soil. Capacitive, time-domain reflectomertry (TDR), and frequency-domain reflectometry (FDR) are all based on this fundamental physical relationship between soil moisture and soil relative permittivity.

Another source of crop data is yield monitors mounted on combine harvesters. As grain (or another crop) is harvested, the yield is measured and this data is tagged with the GPS location of the combine at that moment in time. Several kinds of sensors are used: impact plates which measure the force of grain landing on them, and optical sensors where incoming grain blocks some or all of the light source.

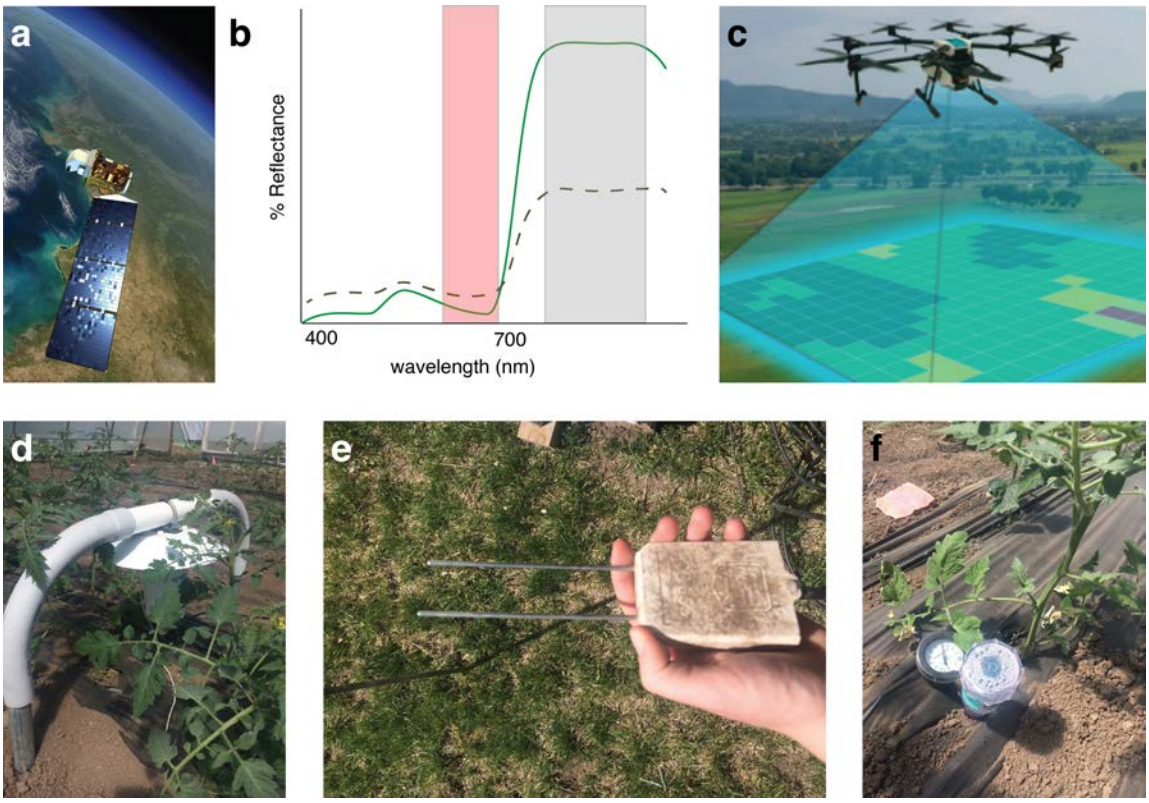

Figure 1.2: a) Landsat8 is a NASA satellite whose color images are publicly available data. Image from [4]. b) Reflectance spectra of healthy plants (solid green) and stressed plants (dashed brown). The Normalized Vegetative Difference Index compares reflection from the red (red highlighted box) and near-IR (gray highlighted box) to provide quantitative data about plant health. c) Drones offer a platform higher-resolution, lower-area imaging. Image from [5]. d-f) Proximal sensors at the Montana State University Horticulture farm d) shaded and aspirated air temperature and humidity, e) soil moisture and electrical conductivity, f) soil water potential.

These sensors give a harvest rate in mass per unit time, which must be corrected by moisture content of the crop material, and divided by the harvester's speed [6]. After harvest, the yield for each point in space is assembled to form a map like the one shown in figure 1.1b. Spacial resolution is limited by the cutting width of the harvester.

To measure chemical concentrations of field soil, soil cores must be collected and

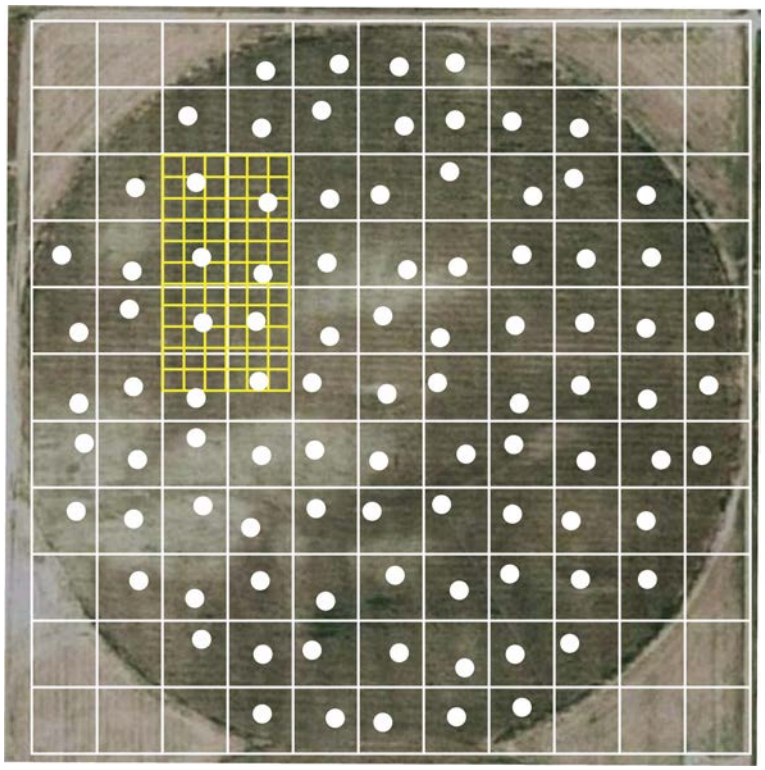

Figure 1.3: To measure spacial variation of soil properties, soil cores are taken from each square in a grid. The white circles represent sampling locations. If no correlation is found between neighboring measurement points, a finer grid may be overlaid on part of the field to find the range of variation.

brought back to a laboratory. There, samples are dried, ground, and filtered. Liquids are run through the prepared soil sample obtain extracts which can be analysed spectrographically or using other chemical techniques. Soil chemistry reports might include a dozen or more elements, such as nitrate, phosphorus, potassium, magnesium, calcium, and sodium.

To measure the spacial variation of soil properties, a field is divided into a grid, and samples are taken at random locations within each grid square, as shown in figure 1.3. After chemical analysis has been done on each sample, the sample-to-sample variation is calculated as a function of distance between sampling locations. If near neighbors' values are not more similar than samples from across the field, this suggests that the spacial variation of that element is greater than the resolution of the

grid. A finer sampling grid can be overlaid on the field, and more samples collected. In this way, researchers have studied spacial variation of a variety of elements, across soil types and geographies. For example, spacial variation for potassium in Montreal is 574 m [7], electrical conductivity in the UK is 163 m [8], organic matter in Missouri is 147 m [9], nitrogen uptake in China is 85 m [10], and phosphorus content in Spain is 30 m [11]. Kerry et al report that measuring at half the spacial variation range is sufficient for precision agriculture management [12]. Therefore, for nitrogen with a spacial variation range of 85 m, one measurement would be needed every 43 m, or 2 sensors/acre.

Management

Management is the decision-making stage. Farmers manage, or make decision about, which crops to plant where, when, and how densely; the type, timing, location, and amount of fertilizer to use; when, where, and how much to water; the use of pesticides, herbicides, or other chemicals; the use of cover crops, beneficial insects, and other practices to improve yield, reduce waste, or provide other benefits to the farm and farmer. The information provided by the analysis of data generated by sensors enables farmers to fine-tune their management to account for variations in time, space, or both.

Irrigation and fertilization events can be scheduled to account for temporal variation in weather patterns and plant growth. For example, irrigation schedules can be adjusted so less water is used following a rainstorm. Weather station data can be used as an input to such schedules, but real-time soil-moisture monitoring can allow for even greater efficiency. For example, Blonquist et al found that adjusting irrigation of a turfgrass plot in Utah using soil-moisture sensor data used 16% less water than a system based on weather station data and evaporation modeling, and 53% less water than a fixed rate system [13].

Other management techniques primarily address spacial variation. Site-specific management zones have been a central concept in PA since 1986 [3]. When a field is treated uniformly, variations arise from differences in soil as shown by the color photograph in figure 1.1a and yield map in figure 1.1b. A grower using management zones would divide the field into two to four zones based on a combination of historical yield data, remote sensing imagery, topography, and sometimes other specific soil properties. Figure 1.1c shows a map of management zones. The following season, the farmer will treat zone 1 differently from zone 2 or 3, but treatment with a zone will be uniform. The use of management zones allows growers to address spacial variation without the need for a large number of sensors or soil sampling locations, but it is not perfect. Yield maps can change from year to year, different data types might

suggest conflicting zone boundaries, and zones for optimal nitrogen application might not align with those for irrigation or pest management. Sensor-based management offers adaptable management accounting for both temporal and spacial variation at very fine scales, but it requires a large number of sensors or sampling points: on the order of hundreds of sensors per field. Sensor-based management of water and nitrogen fertilizer in maize has been shown to improve nitrogen use efficiency without significantly decreasing yield, compared to a management-zone strategy [14].

Actuation

Some technologies used in PA now include variable rate irrigation systems and variable rate fertilization. Center pivot irrigation systems can be programmed to provide a specific amount of water to each approximately 5 x 5 m area. Variable rate sprayers are mounted on GPS-enabled tractors and can be programmed for precision fertilizer or pesticide application using spatially-tagged input data. The tools for precision application have greater spatial resolution than the data that today's proximal sensors can measure. This means that if we had better sensors, we could operate the tools that already exist more efficiently.

The Impact of Precision

While some studies have shown yield increases as a result of variable-rate fertilizer application, many others show no significant difference in yield between uniform and variable rate application. The efficiency improvement comes by eliminating waste–by not applying excess fertilizer in low-producing areas, where it would not be taken up by plants anyway, and by reducing over-application of fertilizer as insurance.

Nitrogen use efficiency (NUE) is defined in agriculture as the fraction of N applied as fertilizer which is utilised by the plant and harvested as yield, represented by equation 1.1

$$\mathrm{NUE}_{CROP} = \frac{\mathrm{Yield}_N}{\mathrm{Fertilizer}_N} \tag{1.1}$$

NUE ranges from 17-50% depending on management strategies, environmental factors, and soil conditions [15]. At low fertilizer rates, NUE is high, as shown by the steep slope in the lower left hand corner of figure 1.4a. When nitrogen is limited, the plants use most of it. When nitrogen is abundant, each additional unit of nitrogen added offers diminishing returns; the plants do not take up as much of the nitrogen, shown by the flat part of the curve in figure 1.4a.

Figure 1.4b shows the yield and expected profit margin as a function of fertilizer application. While there is one clear peak of maximum profit, the price for applying

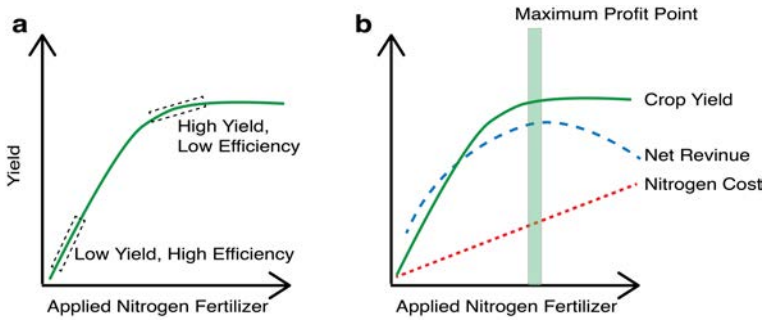

Figure 1.4: a)Fertilizer application dramatically increases crop yields, though there are diminishing returns. At low fertilizer levels, nearly all the additional nitrate is translated into yield improvements, which is represented by the steep slope of the line. At high fertilizer levels, overall yield is high, but nitrogen use efficiency is low, as each unit of added nitrogen does not translate to as great of an increase in crop yields. Adapted from [16] b) The total fertilizer cost increases linearly with amount of fertilizer applied because fertilizer has a fixed price per ton. Because the yield increases diminish, there is a singular maximum profit point. Farmers target this point, although nitrogen use efficiency is typically low. Adapted from [17]

slightly more is minimal, while the risk of applying slightly not enough and losing out on extra yield is significant. Therefore, farmers over-apply nitrogen to avoid profit loss from sub-optimal yield. Increased certainty about how much nitrogen is already available could reduce reliance on over-fertilization as insurance. While over-fertilization makes sense on the individual farm scale, at the landscape scale, it causes problems.

1.2 Nitrate in Agriculture and the Environment

Nitrogen is a vital element for plant growth. It forms part of the chlorophyll compound, which enables photosythesis–the process by which plants convert solar energy to sugars. Nitrogen also is part of proteins and the DNA molecule, making it foundational for all life on earth.

Plants can take in nitrogen from the soil in the form of nitrate or ammonium. Before the invention of chemical fertilizers, biological processes governed the conversion of nitrogen between its many forms. These processes make up the nitrogen cycle, which is illustrated in figure 1.5. Nitrogen in the form of N_2 makes up 80%

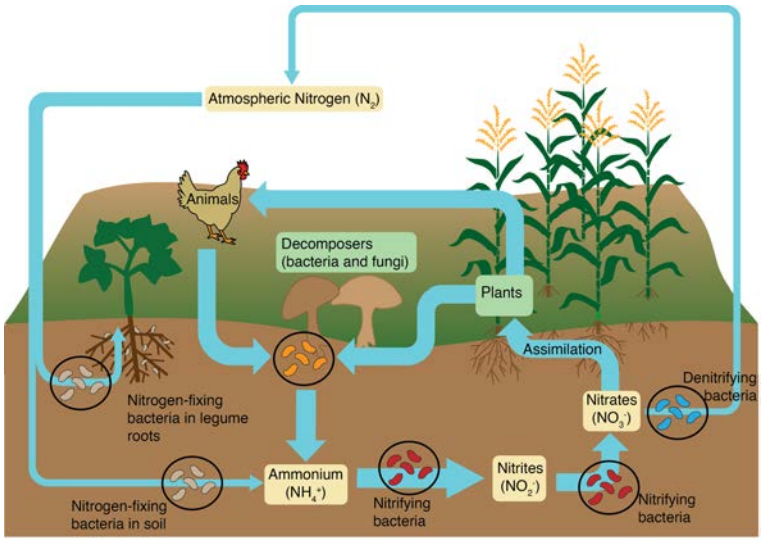

Figure 1.5: Nitrogen is converted from N_2 gas to ammonium, nitrate, nitrite, and compounds in tissues through a complex web of relationships involving bacteria and other microorganisms, fungi, plants, and animals.

of earth's atmosphere, but N_2 cannot be directly used by most living things. A few classes of prokayotes, known as nitrogen fixers, have the ability to convert N_2 to ammonia, NH_3. This is an energetically demanding process, and nitrogen fixation ability is rare. Some nitrogen fixing bacteria live freely in the soil, while many others for symbiotic relationships with legumes such as clover, beans, and peas. The roots of legumes form nodules for the nitrogen-fixing microbes to live in. Another group of micro-organisms in the soil facilitate nitrification, or the conversion of NH_3 to nitrite, NO_2^-, while yet other bacteria and archea transform NO_2^- to nitrate, NO_3^-. Denitrification and anammox are processes, again run by microbes, by which "fixed" nitrogen in the forms of NO_3^-, NO_2^-, and NH_4^+ are converted back to N_2 gas. Incomplete denitrification produces nitrous oxide (N_2O) a potent greenhouse gas. The breakdown of biological materials, such as decaying plant matter and dead organisms, includes ammonification, the process by which nitrogen in larger organic molecules is converted to NH_4^+, which re-enters the cycle [18]

For millennia, the biological processes of the nitrogen cycle governed all ecosystems. Human agricultural practices such as leaving fields fallow, crop rotation, the application of compost, animal manure, or bone meal as fertilizer, and growing corn and beans together, are all techniques to ensure adequate nitrogen for plant growth.

Organic growers still rely on these methods, but large-scale agriculture production uses synthetic chemical fertilizer to vastly increase yield. The application of nitrogen fertilizer to maize can increase yield 60% or more [14].

Nitrogen fertilizer relies on the Haber-Bosch process, which converts N_2 gas to ammonia gas NH_3 using a metal catalyst under high temperature and pressure. Maintaining the conditions necessary for the reaction is extremely energy intensive: at 30 GJ per ton of NH_3 produced, Haber-Bosch nitrogen fixation accounts for 1% of the world's total energy use [19, 20]. The process also produces more than 2.16 kg CO_2-equivalent in greenhouse gas emissions per kg NH3 fixed, which was 1.4% of global carbon emissions in 2019 [19, 20].

Grain growers apply on the order of a hundred to a few hundred pounds of nitrogen per acre, depending on the crop and field conditions [21]. At a cost of tens of cents to a dollar (USD) per pound, with prices rapidly increasing in recent months, it is the second highest cost for many crops, outdone only by seeds [22].

The nitrogen applied in fertilizer does not stay where it is applied. Nitrate in particular is highly mobile, and is a commonly used form in fertilize. Some nitrate is taken up by the plants, as intended. The rest either undergoes denitrification–returning to atmospheric N_2 or problematic N_2O–or leaches to groundwater, or runs off into surface water, as illustrated in figure 1.6. Groundwater polluted with nitrate can pose health risks for rural communities who get their drinking water from wells [23]. Elevated nitrate in drinking water has been found to be associated with Blue Baby Syndrome, cancer, and adverse reproductive outcomes [24]. Municipal water systems, which usually draw from surface water, have filtration processes to keep nitrate levels in check, but downstream ecosystems are impacted by excess nitrate. In ponds, lakes, and coastal areas, abundant nitrate causes eutrophication and toxic algae blooms [25].

These problems are well known and studied, but the tools for measuring nitrate are limited. Nitrate concentrations in water can be measured using chromatography or spectrographic methods in a laboratory [26, 27]. In order to use these tools, water samples must be collected from the stream, lake, or aquifer. To measure nitrate in soil, soil samples are collected from the field and potassium chloride (KCl) extractions can be used to get a liquid exudate which contains all the nitrate that had been in the soil. Nitrogen uptake by plants can be estimated by optical remote or proximal sensing using NDVI or other indecies. At the landscape scale, mass balance equations are used. Taking a known amount of nitrogen applied as fertilizer and subtracting the amount taken up by plants and running off in streams can provide and estimate of the amount leached to groundwater. [28].

To prevent the consequences of excess nitrate in the environment, nitrate levels must be monitored. To better characterize the nitrate problem, and better tailor

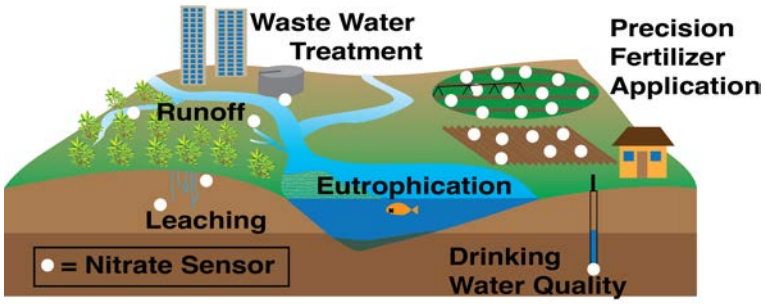

Figure 1.6: Nitrate enters an ecosystem through fertilizer application in agricultural settings or from wastewater. From there, it leaches to groundwater, contaminating wells used for drinking water, or runs downstream to cause eutrophication in surface waters. Improved monitoring through a distributed sensor network could help map the movement of nitrate through the landscape.

nitrogen fertilizer inputs in agriculture, more frequent measurements over large areas is needed. This could be achieved with a network of distributed wireless sensors.

1.3 Wireless Sensor Networks

A wireless sensor network (WSN) is a system of electronic objects which communicate with each other wirelessly using electromagnetic waves, typically in the radio-frequency bands. Wireless communications are designed, regulated, studied, and built at several levels of abstractions, as illustrated in figure 1.7a. At the highest level, the host layer governs user interface requirements for apps or programs that want to run on the network, shown in figure1.7b. Below that is the network layer, which addresses network architecture: which nodes can communicate with which other nodes, and how data is routed through the network. One simple network architecture is a star network, where one central hub can communicate with many nodes, but each node cannot communicate with the other peripheral nodes. Alternatively, in a distributed network, every node can communicate with every other node. In a multi-hop system, data from far-flung nodes can be transmitted to a near neighbor which relays that data towards the data collection center. These architectures are shown in figure 1.7c. One level of abstraction below the network layer is the Data Link Layer, which governs protocols, controls, multiplexing strategies, and collision avoidance. IEEE 802 international standards that define WiFi, Bluetooth, 5G, and

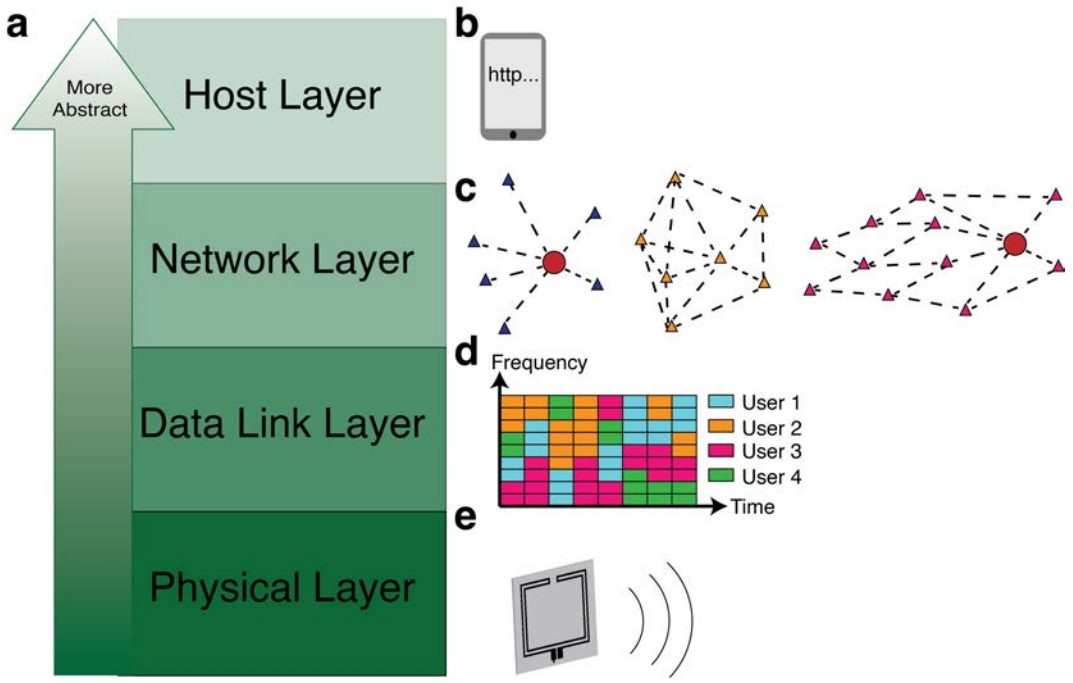

Figure 1.7: a) The ISO model divides a wireless network into four layers of abstraction: b) The host layer interfaces with user applications, c) The network layer determines which nodes can talk to which other nodes, d) the data link layer defines protocols, and e) the physical layer is concerned with antennas and the wireless channel.

other broadly-used wireless protocols are defined at this level. Figure 1.7d shows a schematic of orthogonal frequency-division multiple access (OFDMA) multiplexing, which is a way to encode multiple users' data in the same wireless channel, and is an example of the type of protocol defined at the Data Link Layer. The least abstract layer is the physical layer, which is concerned with antennas' physical shapes, wave propagation, and power loss in the environment. A physical antenna transmitting RF waves is illustrated in figure 1.7e. Chapters (4-6) describes practical concerns at the physical layer for antenna fabrication and deployment in the field, but the constraints on the physical system design are partly defined by requirements of higher layers of abstraction.

In the United States, the Federal Communications Commission (FCC) governs use of the electromagnetic spectrum by dividing it into frequency bands. Most bands are reserved for specific uses, such as marine communications, or commercially li-

censed TV broadcasts. There are two bands centered at 915 MHz and 2.4 GHz which allow unlicensed access for industrial, scientific, and medical uses. The wireless protocols relevant for agricultural WSNs fall into these two bands.

There are many types of protocols defined at the Data Link Layer that have been or could be used in agricultural settings. Table 1.1 lists ten of them. ZigBee is well suited for many agricultural applications because it is energy efficient, reliable, relatively low cost, and able to form mesh networks which can cover large areas despite the moderate node-to-node communication range. ZigBee nodes have a low duty cycle, and sleep most of the time except to periodically transmit data. This makes the protocol compatible with battery-powered nodes as the sleep mode preserves battery life. SigFox is an ultra-narrowband, long distance, low data-rate protocol which has been used in some agricultural applications despite its relatively high power and low datarate. LoRa (Long range Radio) is a protocol designed for low power, wide area communications. It uses a gateway or gateways to transfer information from the LoRa network to a 3G/4G protocol to communicate with the outside world.

More familiar wireless protocols include Wifi, which is widely used and compatible with many different types of devices. However, its short range and high power requirements make it a poor choice for most agricultural applications. Bluetooth is another ubiquitous protocol, offering easy integration with most smartphones and other "smart" devices. Classic Bluetooth has relatively high power requirements, while Bluetooth Low Energy (BLE) uses similar protocols at lower power. Like ZigBee, BLE nodes have sleep cycles which help preserve battery life. Both Bluetooth and BLE have limited read ranges of about 10 m.

GPRS/3G/4G are packet-based protocols that operate on cellular networks. Nodes communicate with cell towers, so node-to-node spacing is not a limiting factor, but the field must be covered by cell networks. Communication delays can be relatively long and depend on the number of users at a given time.

The protocols listed above (ZigBee, SigFox, LoRa, WiFi, Bluetooth, and BLE) all require each and every node to have on-board power. The components required for power management increase the cost, complexity, and size of each sensor node, limiting deployment at the high spatial resolution needed for precision agriculture. Even the cheapest or smallest batteries are ill suited for large scale deployment, as they are non-rechargeable, so the nodes would need to be replaced or picked up to prevent build-up of dangerous chemicals. By contrast, a system with one active reader and many passive (battery-free) nodes is attractive for widespread deployment of nodes. Battery-free wireless communication protocols work on backscatter principles, where the passive nodes harvests energy from the RF signal sent by the reader, uses that energy for power to take a sensor reading, and modulates its impedance to encode data in the reflected signal back to the reader. Passive RFID is a commercially avail-

Table 1.1: Wireless network protocols

Protocol	Range	Sensitivity	Power	Frequency	Data Rate	Reference
ZigBee	10-100 m	-100 dB	10-37 mW	915 MHz or 2.4GHz	20-250 kbps	[29, 30, 31]
SigFox	10 km	-126 dBm	122 mW	915 MHz	100 bps	[32]
LoRa	10 km	-149 dBm	50-100 mW	915 MHz	18 pbs-37 kbps	[29, 32]
WiFi	20-100 m	-95 dBm	100 mW	2.4 GHz	2-54 Mbps	[29, 32, 31]
Bluetooth	8-10 m	-97 dBm	10-30 mW	2.4 GHz	1-24 Mpbs	[29, 31]
BLE	10 m		10 mW	2.4 GHz	1 Mbps	[32]
GPRS/3G/4G	anywhere w/ cell service			915 MHz or 2.4GHz	50-200 kpbs	[31]
Passive RFID	10 m	-85 dBm	5-10 μW	915 MHz	40-640 kpbs	[29]
LoRa Backscatter	230m or 2km	-159 dBm	10 μW	915 MHz	18 pbs-37 kpbs	[29]
NFC	10 cm		passive	13.6 MHz	424kbps	[33]

able battery-free, backscatter system. LoRa backscatter is an area of active research which could enable long-range battery-free wireless communication, but is not commercially viable [29]. Near-field communication (NFC) is another widely used form of communicating with passive objects in everyday life, but it is limited to very short distances–10 cm or less–making it not suitable for use in agriculture.

Many sensors in agricultural settings today are not wireless networks at all, but single-point hubs with one wireless uplink. For example, a typical weather station like the one shown in figure 1.8a-b has a central modem which uses cellular networks to upload data to an internet database. The individual sensors, such as temperature, humidity, anemometers, soil moisture probes, and rain gauges, are physically wired to a the central hub which includes a multichannel data logger, rechargeable batteries, a solar panel, and a modem. Figure 1.8c shows one node using cellular networks. If multiple nodes like this are spread across an area, they could form a network.

Figure 1.8d shows several soil moisture sensor nodes which communicate using a general packet radio service (GPRS) based network within the field and one gateway node which reports data to a farmer. Figure 1.8e shows a soil sensor node compatible with RFID communications.

In conclusion, although many options exist for wireless sensor networks for agriculture, there are trade offs between power consumption/battery life, data rate, and read range. Most systems involve complex nodes with onboard power, which requires regular maintenance. Maintenance-free, widely distributed nodes should be battery-free, which today means to passive RFID systems.

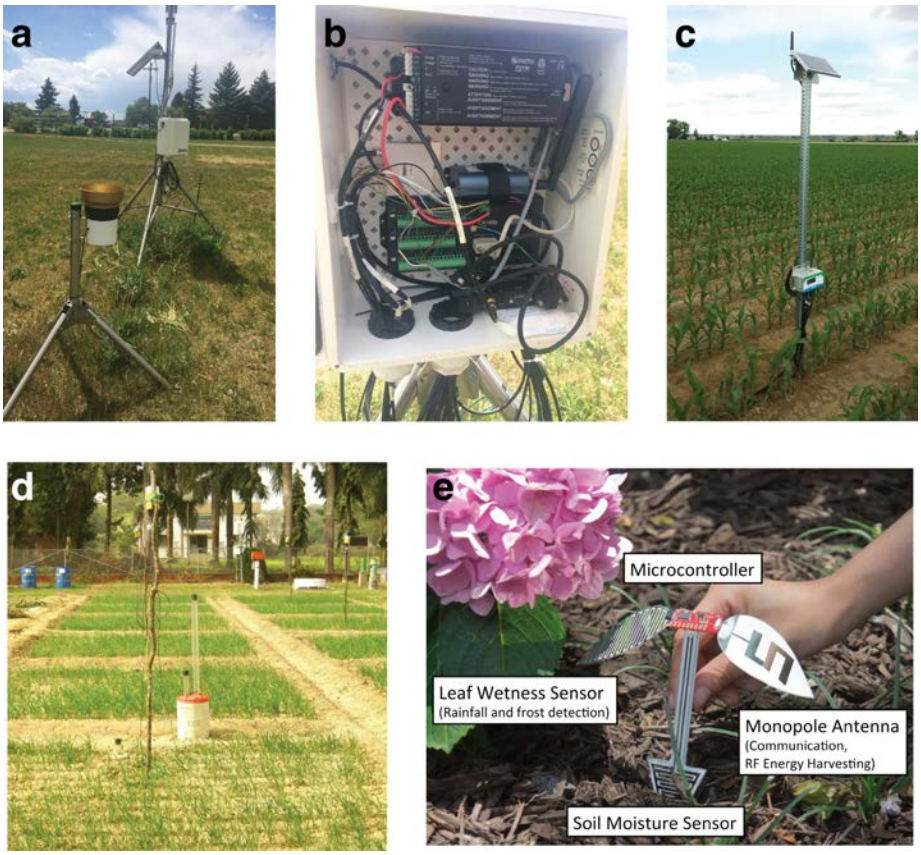

Figure 1.8: a) single-point weather station with a temperature, anemometer, solar radiation, rainfall, and other sensors wired to a central hub. b) The data logger and cellular up-link modem inside the hub of the weather station. c) A stand-alone soil moisture installation with solar power and cellular data upload capability. d) Cellular-based soil moisture sensors deployed at IIT Kharagpur from [31] e) inkjet printed soil moisture and leaf wetness sensor with RFID communication from [34].

1.4 Printing Technology

Printing enables mass manufacturing of low-cost devices at scale.

Printing encompasses many types of solution processing techniques, including blade coating, inkjet printing, stencil printing, spray coating, screen printing, grauvure printing, and slot die casting. All are additive manufacturing techniques, meaning that material is only deposited where it will be used. Many printing techniques

are scalable to roll-to-roll processing, which is a high-throughput, low cost mass fabrication technique. Printing processes operate at substantially lower temperatures than conventional PCB/silicon fabrication. This makes printing compatible with unconventional substrates like flexible plastic and biodegradable materials which would melt at high temperate. Printed devices, whether working with thin or thick films, have a planar geometry, and can be flexible and/or conformal. These attributes of printing can turn into important advantages in different application spaces. In environmental monitoring, the mass-production element of printing and compatibility with biodegradable materials is important.

Ink

All printing involves ink. Inks are liquid solutions containing a functional material that gives the ink the desired electrical properties, a polymer binder to hold everything together after the ink dries, additives such as surfactants to improve dispersion, or other fluid properties, and a solvent system in which everything is dissolved. Inks for printed electronics include conductive inks, often made from silver, gold, or carbon, semiconducting polymers, and insulators. Figure 1.9 illustrates the components of a conductive ink. There are many commercially available inks that are specially formulated for a particular printing technique. Inkjet ink is a thin liquid with viscosity around 10-15 cps and solid content 30-40%. Spray coating ink is also a thin liquid with viscosity 50-100 cps and silver content 35-40%. Additives in spray coating ink can help with adhesion and mechanical flexibility. Screen printing ink (which can also be used for stencil printing) is a paste-like ink with high viscosity on the order of 30,000 cps and silver content $> 80\%$ after curing. Varieties of screen printing ink are developed for adhesion to specific substrates, for very fine feature resolution, or for particularly high conductivity.

To print materials or material combinations outside of what is commercially available, a researcher can make their own inks by mixing fillers, binders, solvents, and additives in different ratios to achieve the desired viscosity, surface tension, adhesion, and electronic behavior. The ink-making process specifically for conductive zinc ink is described in more detail in section 2.2.

Once an ink has been made or selected, there are several printing techniques available for ink deposition.

Blade Coating

In blade coating, a blade of controllable, fixed height pushes ink at a steady rate across the substrate, as shown in figure 1.10a. Thin films of 100 nm or less are possi-

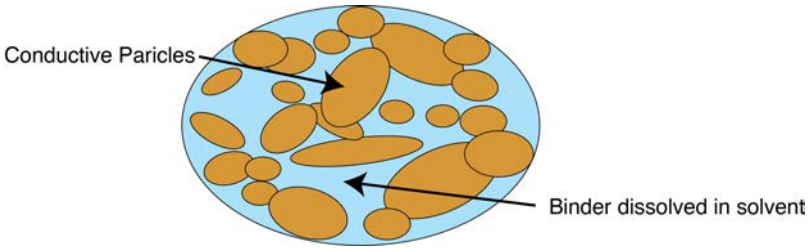

Figure 1.9: Conductive inks are made of discrete micro- or nano- particles of the conductive material, dispersed in a solution of solvent, polymer binder, and additives.

ble, and the thickness is determined by ink viscosity, blade speed, and blade height. There is no patterning mechanism inherent in blade coating: the ink covers the full area of the substrate unless the substrate is treated before printing. Hydrophillic wells can be created where ink will wet, separated by hydrophobic barrier layers. This allows patterning using blade coating [35, 36].

Inkjet Printing

In inkjet printing, ink is contained in a cartridge which has piezoelectric nozzles to dispense the ink drop by drop onto the substrate as shown in Fig.1.10b [37]. The pattern printed by an inkjet printer is digitally generated and can easily be modified, which makes inkjet printing an attractive candidate for prototyping. A disadvantage of inkjet printing is that, because patterns are produced drop by drop, it can be much slower than other printing options. Inkjet printing typically produces metal traces with thickness of a few hundred nanometers at most. Minimum feature size depends on drop volume, ink viscosity and chemistry, and substrate surface energy, but is generally in the range of 10 to 50 μm. Surface chemistry can be modified with monolayer or plasma treatments to improve print quality and resolution for a specific ink [38].

Spray Coating and Stencil Printing

Stencil printing and spray coating both use a stencil mask to define the pattern. Stencils can be made of metal or plastic films or tapes. Plastic film or tape stencils can be created with a laser engraver [39]. These types of stencils are easily modified for prototyping but can have limited feature resolution, on the order of 500 µm.

Once the stencil is prepared, ink is applied through either spray coating or stencil printing. In spray coating, an air brush is used to apply ink as an aerosol as shown

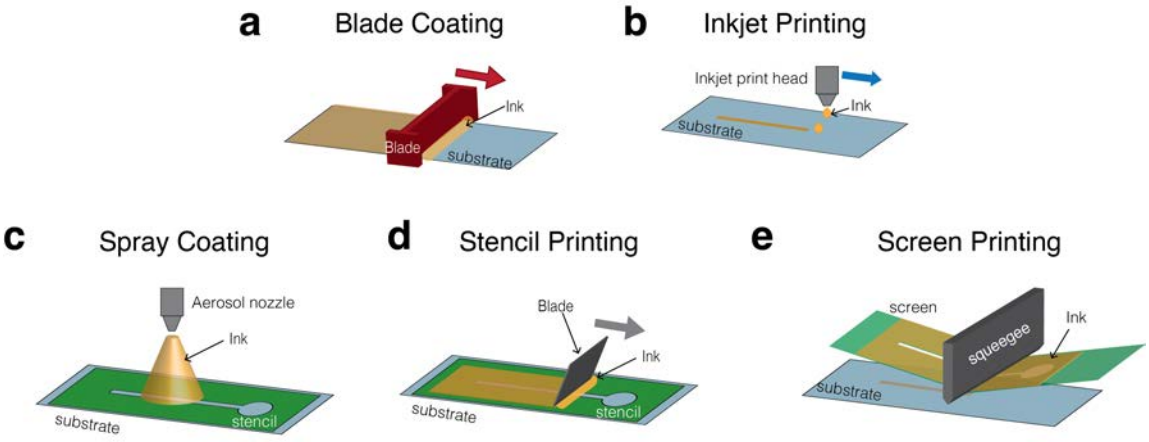

Figure 1.10: a) Blade coating uses a blade of a fixed height and speed to create a broad coat of ink. b) In inkjet printing, ink is deposited drop by drop from a cartridge. c) In spray coating ink is applied as an aerosol, and pattern features are defined with a stencil. d) In stencil printing ink is applied with a blade in direct physical contact with the pattern-defining stencil. e) In screen printing ink is forced through a patterned mesh screen with a squeegee.

in Fig.1.10c. Final layer thickness is determined by the distance between the brush and the substrate, the speed that the brush is moved across the substrate, the flow rate of air and ink, and the number of the passes of the brush over a certain area. Spraying can be controlled by an automatic sprayer, or done by hand.

Stencil printing uses ink formulated for screen printing. The ink is spread across the top of the substrate and dragged with a blade over the pattern as shown in Fig.1.10d. The thickness is set by the speed of the blade, the thickness of the stencil–which sets blade height–and the viscosity of the ink. Automated set ups can control the blade speed, or the blade can be moved by hand. Production by hand allows for fine tuning the angle between the blade and the substrate and the pressure of the blade in order to get a clean print, but can be less reproducible than automated printing.

Screen Printing

Screen printing uses a mesh screen to define the pattern. These screens are specially made with emulsion layers and mesh size chosen based on the ink properties. A flood bar spreads the ink over the screen, then a squeegee forces the ink through the holes in

the mesh, transferring the pattern onto the substrate as shown in Fig.1.10e [40]. This technique is very fast and scalable to roll to roll (R2R) processing. Minimum feature size is about 50 μm. Thickness is determined by the ink and process parameters, such as ink viscosity, squeegee pressure, and screen height, and is generally on the order of 10's of μm. Screen printing is not suited to early prototype work because changing the design requires fabricating or purchasing a new custom screen.

Curing

Conductive inks contain discrete solid particles, so many metallic traces are not conductive immediately after printing. A curing or annealing step is required to fuse the discrete particles together into a single conductive trace [41]. Curing can be thermal, UV, or laser-based. In thermal annealing of silver traces, higher temperatures generally yield higher conductivity traces. The annealing temperature should not be above the glass transition temperature of the substrate or the substrate will be deformed. Photonic sintering can avoid the heat-impacts of thermal curing, but requires specific curing tools.

1.5 Transient Electronics

For widespread deployment of sensors in a field, hundreds or thousands of nodes could be needed. That number of electronic devices made of conventional electronic materials and plastics would create either an arduous chore for someone to collect them all before harvest, or a large quantity of potentially hazardous trash, and likely both, particularly as some nodes are likely to be broken by weather or farm equipment, strewing micro-trash around the field. In order to avoid the problems of pollution and the need for retrieval, the sensor nodes can be made from biodegradable materials.

Transient electronics are electronics which are designed to have a limited operational lifetime, then breakdown into biologically or environmentally compatible materials. Much of the pioneering work in the field was motivated by medical applications, where temporary sensors or therapeutics could be ingested or implanted, without the need for their surgical removal later. In these applications, functional lifetimes of hours or days are sufficient and rapid breakdown is often desirable. Transient electronics also has applications in sending sensitive data–the information will be completely unavaialbe after the life of the device.

To make wireless sensor nodes for agriculture, conductors and insulators are needed. Conductors form the RF antennas and the wires or connecting traces to

Table 1.2: Biodegradable conductive materials for transient electronics

Conductor	**Binder**	**Conductivity**	**Reference**
LIG		25 S/m	[42]
Carbon Black		x S/m	
PEDOT:PSS		10 S/m	[43]
PEDOT:PSS w/ sulfuric acid		1000 S/m	[43]
W	PLA	5000 S/m	[44]
W	PEO	3500 S/m	[45]
Fe	PCL	1000 S/m	[46]
Mo	PBAT	1200 S/m	[47]
Mo	PBTPA	1000 S/m	[47]
Mo	Candalila Wax	130 S/m	[47]
Zn	PVP	4×10^4S/m	[48]
Zn		1×10^6 S/m	[49]
Zn	PVP	3×10^5 S/m	[50]
Zn	PVB	1×10^5 S/m	[51]

attach sensors to the chip. Conductors can be metallic, various forms of carbon, or conductive polymers. Metals typically have much higher conductivity than carbon or polymeric materials. Conductive materials are listed in table 1.2. Metals which are suitable for biodegradable electronics readily form oxides, which make their traces less conductive or not conductive at all.

In printed electronics, insulators form the structural supports, printing substrates, encapsulation layers, and binders in many conductive inks. They make up the vast majority of the mass of a system, so finding fully degradable materials is crucial for the degradation of the system as a whole. Some biodegradable insulator options are summarized in table 1.3. These can be sourced from plant and animal products, such as silk, chitosan, and cellulose, or synthetically made polymers.

Whatever their sources, insulators can break down in a variety of ways. The first distinction in breakdown mechanisms is between physical and chemical changes.

Table 1.3: Biodegradable non-conductive materials for transient electronics

Class	**Material**	**Usage**	**Water Soluble**	**Melting Temperature**	**Degradation Pathways**	**Reference**
Synthetic	PLA	substrate, encapsulation, ink binder	No	150-160°C	Hydrolysis, Thermal, UV	[44]
Synthetic	PCL	substrate, encapsulation, ink binder	No	60°C	slow hydrolysis, Enzymatic	[52]
Synthetic	PVP	substrate, encapsulation, ink binder	Yes	150-180°C	Enzymatic, Thermal	[53, 54]
Synthetic* Produced by bacteria	PHBV	substrate	No	101-172°C	slow hydrolysis, Bacterial	[55, 56]
Natural	Paper	substrate	No	N/A		
Natural	Wood	substrate	No	N/A		
Natural	Beeswax	encapsulation	No	63 °C	Enzymatic, Hydrolysis	[57, 58]
Natural	Candalila Wax	encapsulation	No	65-68 °C		

Physical degradation, including dissolution in water and mechanical disintegration can allow residual parts of a system to be excreted from the body in a medical use case, and are effective end-of-life mechanisms for destroying sensitive information. However, they do not constitute full degradation as the polymer chains are still chemically intact. Chemical breakdown involves cleaving of chemical bonds such that the polymer breaks into oligomers and monomers, or even more basic compounds like CO_2 and water. Chemical breakdown is often via hydrolysis, or the reaction of water with ester, anhydride, acetal, ketal, or imine bonds. Other forms of chemical breakdown include thermal decomposition, at elevated temperatures, and photodegredation from exposure to UV radiation. In soil, microbial activity and enzymes can facilitate chemical decomposition of polymers, waxes, and natural materials.

Poly(lactic acid) (PLA) is a widely used polymer, including for 3D printing, and is often combined with plant-based starches to form compostable eating utensils and other "green" consumer goods. It breaks down through hydrolysis and thermal decomposition, but requires the elevated temperatures of managed composting facilities for significant breakdown. Under ambient conditions it does not degrade.

Polyvinylpyrrolidone (PVP) is a water-soluble polymer used in pharmaceuticals,

contact lenses, and many other household products. Because PVP is water soluble, devices made with it easily dissolve, but chemical decomposition of the PVP molecules themselves requires enzymes or elevated temperature [53].

Polycaprolactone (PCL) is a slow-degrading, hydrophobic polymer which is hydrolyzable over the course of a few years and can be degraded more quickly by the enzyme lipase [52].

Poly(3-hydroxybutyrate-co-3-hydroxyvalerate) (PHBV) is a natural polymer produced by bacteria. It is a combination of 3-hydroxybutyrate and 3-hydroxyvalerate, and the ratio of these components can be used to tune the properties of PHBV. It is biocompatible and biodegradable, broken down by bacteria, but is brittle and lacks mechanical strength [55].

Beeswax is naturally sourced, hydrophobic, and composed primarily of wax esters, hydrocarbons, and fatty acids [57, 58, 59, 60]. It breaks down primarily through hydrolysis, facilitated by several enzymes specific to the constituent wax esters and fatty acids.

Composite materials might experience degradation or disintegration of the structural matrix or binding element holding the material together. As this matrix structure breaks down, the small, functional, non-degradable microparticles formerly held within the matrix are released, as shown in Figure 1.11 [61].

Discussing and comparing different transient electronic systems' biodegradability can be challenging because of a lack of clarity in definitions for words like "degradable," "biodegradable," "compostable," or "bio-based." In the scientific literature, "biodegradable" often means "able to be broken down into smaller pieces at biologically benign or physiological conditions," and is used in contexts where the device is inside the body of a person or an animal. "Environmental biodegradation" happens outside of a human or animal body, and refers to materials which break down in the presence of microbes, although the specifics of degradation environments vary widely. "Compostable" materials can be broken down in municipal or industrial composting sites which are actively managed and typically include initial mechanical chopping or shredding of input stocks, and temperatures of around 50-60°C produced by microbial activity inside the compost pile.

International standards for biodegradable plastic packaging provide some scientific rigour and consistency to definitions, though few scientific papers carry out testing in accordance with these industrial standards. In the United States, standard ASTM-D6400 and internationally, ISO-17088 are widely used to certify materials which are aerobically composted in municipal or industrial composting facilities. Other standards govern breakdown in freshwater and saltwater environments. Degradation in unmanaged terrestrial environments and soil, which can experience a wide range of environmental conditions, is not well covered by existing standards.

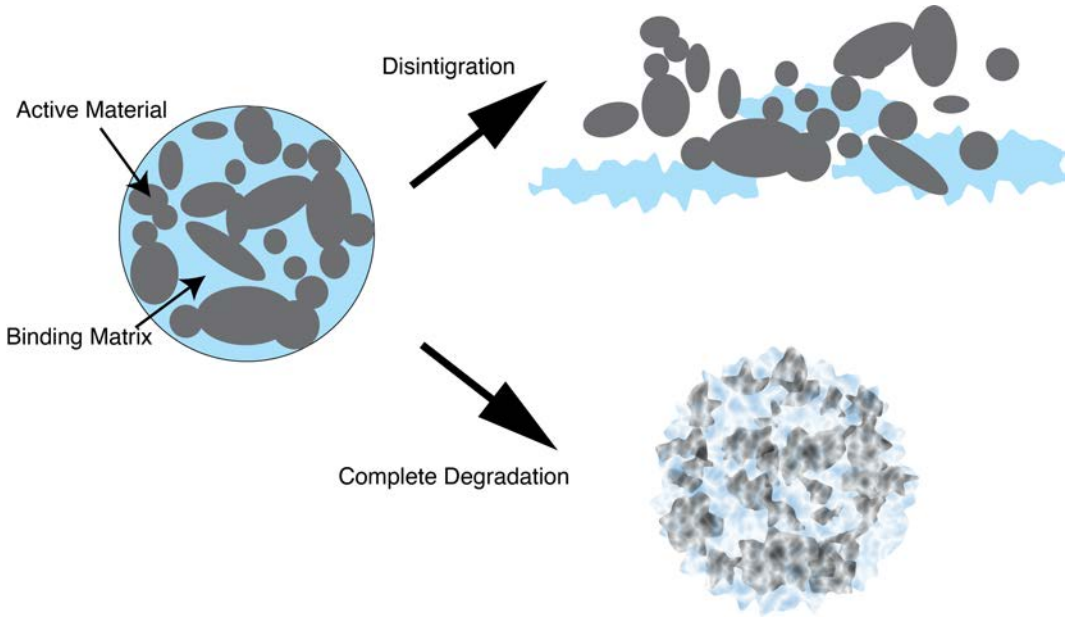

Figure 1.11: A composite material might experience disintegration if the binding matrix is made of a biodegradable material while the active material inside does not degrade. Complete biodegradation involves the molecular breakdown of all constituent parts.

More research is needed to show how breakdown times of materials under controlled conditions in a lab relate to real-world lifetimes.

The central challenge of transient electronics is achieving stable performance of a devices' functional lifetime followed by breakdown. That is: the device must degrade entirely, but it cannot start breaking down too soon, or the measurements will be erroneous. figure 1.12a illustrates desirable performance for a conductive element: high conductivity over the defined lifetime, followed by distinctive failure. In order to achieve this kind of behavior, rapidly-degrading inner materials can be protected by slowly-degrading encapsulants, as shown in figure 1.12b. Once the encapsulant is breached, cracked, or worn away, then and only then will the inner material break down.

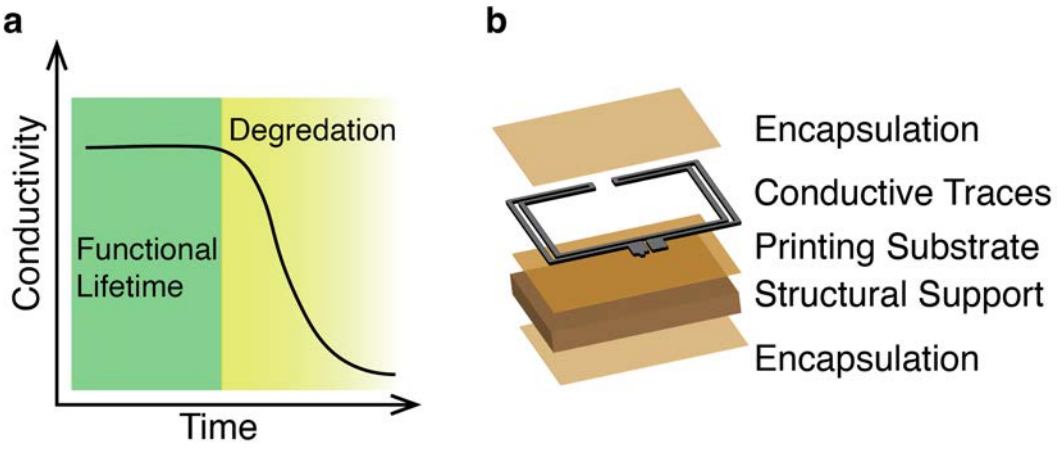

Figure 1.12: a) Transient electronics should have stable, high performance during their lifetime, and fail distinctively when they begin to degrade. b) A biodegradable antenna consists of support and substrate layers, the conductive antenna itself, and front- and back- encapsulation layers. The encapsulation ensures stable performance over the lifetime of the device, and its failure triggers breakdown of the rest of the layers.

1.6 Scope of this Thesis

This thesis describes the design, fabrication, and characterization of the constituent parts of a printed, biodegradable, wireless soil nitrate sensor, as well as the integration of the parts to form a node for precision agriculture applications. The main topics of the thesis are:

1. Chapter 2: Print-based fabrication with biodegradable materials
2. Chapters 3-4: design, fabrication, and characterization of conventional and biodegradable versions of the constituent parts of the sensor node: the nitrate sensors and the RF antennas
3. Chapters 5-6: Integration of the constituent parts and deployment in field and greenhouse studies.

Figure 1.13 illustrates the focus areas of each chapter and how they come together to create a complete sensor node.

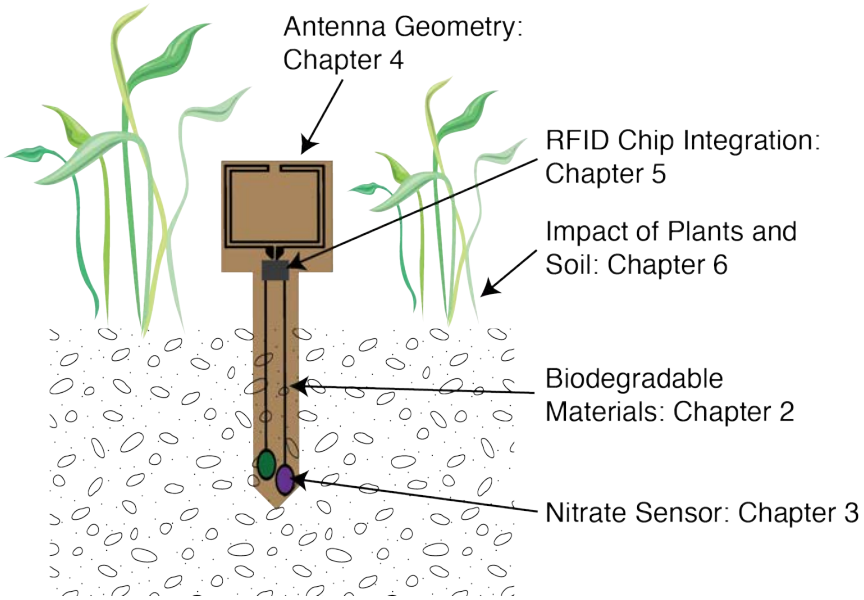

Figure 1.13: Pictorial overview of the thesis

Chapter 2 describes fabrication processes for printing biodegradable electronic devices. We discuss substrate options, desired properties of substrates, and techniques available to create suitable printed surfaces out of wood and wax. Next, we turn our attention to biodegradable conductors, adapting a room temperature chemical sintering process for making conductive zinc traces. The ink composition, printing, and chemical treatment are optimized for high conductivity and trace longevity.

Chapter 3 describes the nitrate sensors. We have developed fully printed potentiometric nitrate sensors and characterized their sensitivity and selectivity to nitrate. Each sensor comprises an ion-selective electrode and a reference electrode that are functionalized with polymeric membranes. The sensitivity of the printed ion-selective electrodes was characterized by measuring their potential with respect to a commercial silver/silver chloride reference electrode in varying concentrations of nitrate solutions. The sensitivity of the printed reference electrodes to nitrate was minimized with a membrane containing polyvinyl butyral (PVB), sodium chloride, and sodium nitrate. Selectivity studies with sulphate, chloride, phosphate, nitrite, ammonium, calcium, potassium, and magnesium showed that high concentrations of calcium can influence sensor behavior. The printed ion-selective and reference electrodes were combined to form a fully printed sensor with sensitivity of -48.0 ± 3.3 mV/dec. Biodegradable nitrate sensors made with printed carbon on paper with

beeswax encapsulation showed similarly high sensitivity to nitrate, and the use of carbon as a transducer layer improved the sensor stability. Both gold- and carbon-based nitrate sensors showed good linearity and sensitivity to nitrate in small-scale soil tests.

Chapter 4 covers antennas for UHF-RFID systems. Here we demonstrate compact, flexible RFID antennas. We compare fabrication techniques for printed antennas and demonstrate that screen and stencil printing are both suitable for fabricating antennas; these different techniques are most useful at different points in the design cycle. We characterize two versions of flexible, screen printed folded dipoles and a meandered monopole operating in the 915 MHz band. Antenna designs are then modified for implementation on wooden substrates with wax encapsulation layers. We present a technique for scaling the geometry of an existing antenna design given planned substrate and encapsulation materials and thicknesses. Minimum conductivity requirements for antennas were determined and the conductive zinc from chapter 2 was shown to meet these thresholds. This zinc ink was finally used to print functional biodegradable antennas.

Chapter 5 is about system integration of the printed antennas and printed nitrate sensors with commercial, not-printed electronics. The printed antennas from chapter 4 were integrated with conventional silicon RFICs to form passive, battery-free RFID tags. Physical and electrical connection approaches were explored and a process for improving power flow through partial impedance matching was established. These processes are chip-agnostic, enabling connection between any packaged commercial UHF-RFIC and our printed antenna. Requirements for readout electronics for potetiometric nitrate sensors are also discussed. As an intermediate step, printed nitrate sensors were combined with Arduino boards to form hybrid stakes suitable for greenhouse testing.

In chapter 6, considerations for moving from the lab to the field are discussed. Wooden stakes with and without beeswax encapsulation layers were placed in pots with growing corn for 90 days. Un-encapsulated balsa wood stakes experienced significant degradation below the soil line, while encapsulated stakes showed no signs of degradation. This demonstrates both the degradation of the main body of the stake and the effectiveness of beeswax as an encapsulant. Second, the nitrate sensors were measured in soil of different textures and water contents. We found that nitrate sensors require a certain minimum water content in order to provide a meaningful measurement, and this minimum water content depends on soil type. These studies also highlighted the need for reduced sensor-to-sensor variation and improved lifetimes of nitrate sensors. Finally, we measured wireless link strength of passive UHF-RFID in and around soil and crops. Although tall, dense crop canopies obscure line-of-sight between reader and tag, the presence of crops did not significantly

reduce read range for the passive RFID link. Proximity to wet soil, however, substantially reduced read range. This effect was mitigated by placing the antenna a few centimeters above the soil surface. Taken together, chapter 6 shows that although growing crops and real field soils introduce many variables into the sensor node's environment, there are techniques available to mitigate impacts to each constituent part. This provides a solid foundation for full deployment in an outdoor field in the near future.

The next steps for integrated node fabrication are laid out in the conclusion. Other applications of the constituent parts are briefly discussed. Finally, ideas for use cases are presented, together with opportunities and challenges associated with different system architectures.

Chapter 2

Biodegradable Materials

This chapter explores considerations for creating biodegradable electronics by focusing on the case study of the optimization of highly conductive zinc traces on biodegradable substrates. The process consists of five major steps–substrate preparation, ink formulation, printing, acid treatment, and drying–which are listed in figure 2.1. For each step, the desired properties are described and the controllable parameters explored. The complete process involves combinations of the conductive and insulating materials which were described in section 1.5.

2.1 Substrates

The substrate is the foundation of a device, the layer on which ink is printed, so a substrate's properties determine numerous aspects of the device's fabrication, operation, and degradation. Important properties of substrates include surface roughness, thickness and uniformity, surface energy, temperature limits, biodegradation mechanisms, and solvent compatibility.

All printed devices have a substrate, which could be thin and flexible to be compatible with roll-to-roll processing. Additionally, the agricultural sensor nodes have a stake, which is a rigid material that planted in the field, and provides mechanical support for above-ground wireless communication components and protection for below-ground traces to subsurface sensors. We chose wood as a stake material because it is completely biodegradable, is not eco-toxic, does not melt, cannot be physically dissolved in a solvent, is not chemically degraded by chemicals commonly used in printing processes, and is not brittle.

In conventional industrial printing, the substrate is a thin and flexible material which is compatible with roll-to-roll processing. Flexible substrates such as paper or

a

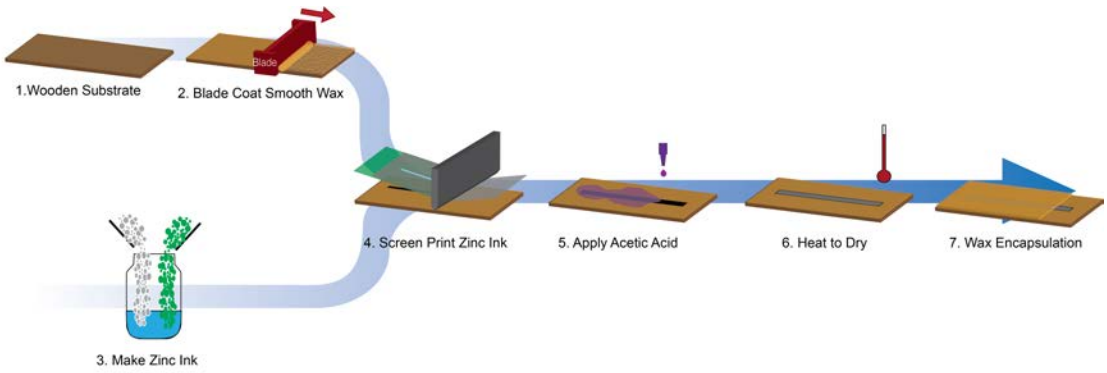

b

Step	Optimizing For	Control Knobs
Substrate	• Smoothness, • Uniform thickness, • Surface energy for low slump and good adhesion	• Substrate type (balsa/bass/pine woods, Bristol paper, PET, etc) • Coatings (wax, PCL solution) • Coating application method (dip, blade coat, iron, press, molds)
Ink	• Low slump • Many prints without drying in screen • Lifetime of finished conductive trace	• Binder • Solvent • Binder:solvent ratio
Printing	• Clean edges • Pattern fidelity • Thick traces • Fine features resolution	• Snap-off • Squeegee pressure • Flood and squeegee speed • Ink volume
Acid Treatment	• High conductivity • High yield • Good adhesion • Lifetime	• Acid concentration • Wet time • Wetting technique • Temperature during wetting
Drying	• High conductivity • High yield • Lifetime	• Drying temperature • Drying technique (hot plate, heat gun, nitrogen gun, oven) • Drying time

Figure 2.1: Creating conductive zinc traces is a multi-variable optimization process of five major steps: substrate preparation, ink formulation, printing, acid treatment, and drying. Each step influences final performance in different ways and later steps may need to be re-optimized after changes in earlier steps. a) Pictorial overview of fabrication process. b) List of independent and dependant variables in the optimization of each step.

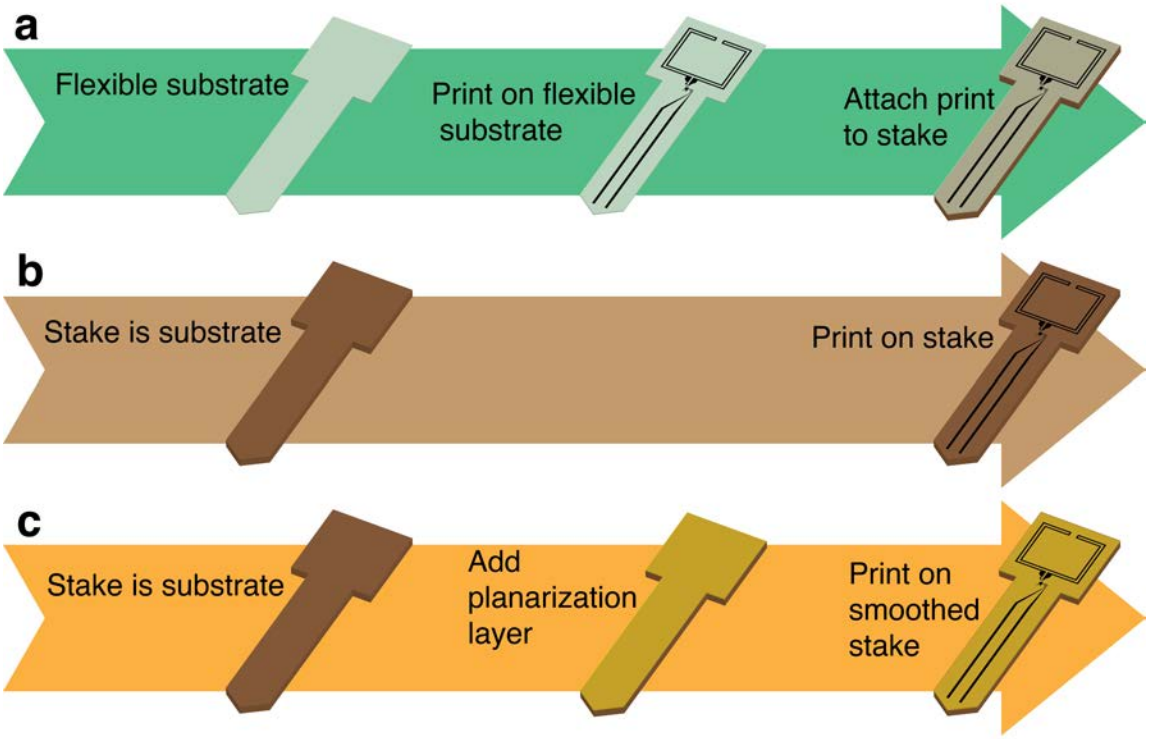

Figure 2.2: a) patterns can be printed on a flexible substrate, and later adhered to a rigid backing stake. b) patterns can be printed directly on a rigid material which serves as both substrate and stake. c) the surface of the rigid backing stake can be treated with another material to improving printability, then patterns can be printed onto it.

biodegradable polymers could be used for biodegradable sensor nodes. Inks printed on flexible materials should be designed for flexibility to avoid cracking when the substrate is bent. In this case the device would be printed on the substrate, and later adhered to the rigid stake, illustrated in figure 2.2a. Alternatively, the stake itself can serve as the printing substrate, which simplifies the fabrication process by avoiding the adhesion step and any damage from bending brittle traces, illustrated in figure 2.2b. However, this approach requires that the stake have suitable properties for printing, which is challenging for natural stake materials like wood. A third, intermediate approach is to soak or coat the stake in a non-conductive material to improve printability, as shown in figure 2.2c. These treatments are described below.

Surface Roughness

A good printing substrate's surface roughness should be significantly smaller than the width and thickness of the features printed on it. Untreated wood has a rough, anisotropic surface dominated by the grain pattern in the wood, illustrated by the profiles in the left-most columns of figure 2.3. The balsa wood had slightly greater surface roughness than pine, which came from larger pores in balsa wood. The high surface roughness led to gaps in printed traces, significant edge roughness, and poor print quality of fine features, as shown in the left column of figure 2.4.

One way to improve print quality is to print on a substrate other than wood and attach the printed pattern to the stake later. This allows for a greater selection of substrate materials because the substrate does not need to provide structural support. Paper is an example of a biodegradable substrate suitable for printing. Bristol paper was chosen; this material had a surface roughness of about 3 μm and no anisotropy, as shown in the third column of figure 2.3. Features printed on paper, shown in the second column of figure 2.4 showed smooth edges and good definition of small features. Paper was a good substrate for printing, but paper's ability to wick liquids and hold water complicated the wet processing of later steps: traces on paper substrates did not become conductive when treated with acetic acid solution.

In order to improve surface roughness of wood substrate, and provide a non-wicking surface for later wet chemical processing, a layer of wax was added as a planarization layer on top of the wood. There are many techniques for coating wood with wax, each of which has its own surface properties.

The simplest wax coating technique is dipping wood in a vat of molten wax. However, this created bubbles from air escaping from the pore space of the wood. To avoid these bubbles, wood samples were soaked in wax for at least 15 minutes before removal, allowing time for the wax to fill the pore space in the wood. The surface of the wax-soaked wood was smoother on the fine scale (horizontal distance of 10 μm or less) but had more bumps and waviness on the order of 100's of μm widths and 10's of μm in height. These bumps impacted the print quality, particularly on smaller features.

One way to flatten the wax is to immediately press it against a cold, flat, metal plate when it is removed from the melted wax. Because the metal is cold, the wax does not stick to the metal, and the wax hardens with a smooth surface. Both parallel to and perpendicular to the grain of the wood, the cold-pressed wax was smoother than the soaked substrates. The cold-pressed samples had undulations and waviness at longer horizontal scales than the soaked samples. A variation on the cold-press technique is pressing the wet samples against a smooth layer of silicone, whose nonstick surface can be peeled away once the wax hardens. An advantage

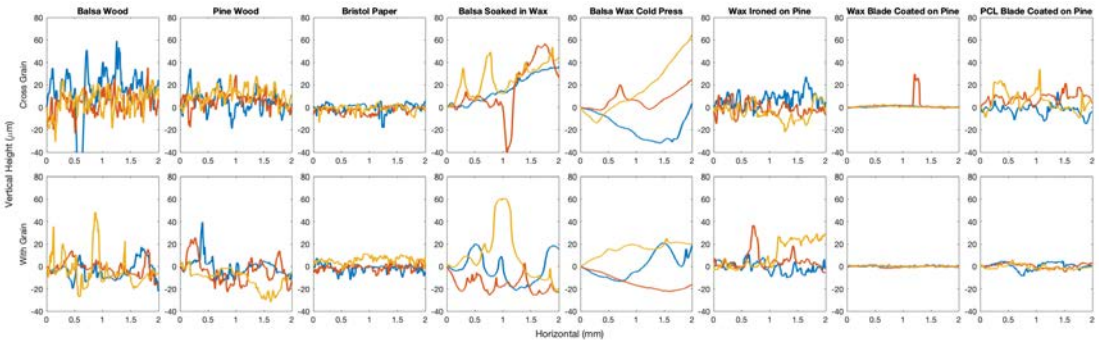

Figure 2.3: Representative profiles with and across the grain for 8 types of biodegradable substrates

Table 2.1: Surface roughness of biodegradable substrates (standard deviation)

Method	Cross-grain Roughness (μm)	With-grain Roughness (μm)
Balsa	16.4	9.5
Pine	7.5	9.3
Paper	3.3	3.0
Soaked	16.3	14.0
Pressed	13.3	7.7
Ironed	6.4	8.2
Blade Wax	2.2	0.6
PCL	5.8	2.4

to this technique is that no active cooling is required, so press-plates can be reused frequently. Patterns printed on pressed wax had smooth edges and good fine feature fidelity, as shown in the center column of figure 2.4. Hand-pressed substrates can be up to about 5 by 5 cm, but larger substrates would require automated processing in order to achieve even pressure across the full area.

In order to create larger area substrates with smooth surfaces, a blade coating technique was used. In this process, the titanium doctor blade (Zehtner ZUA 2000) was heated on a hotplate at 300 °C , which is well above the 67 °C melting point of wax. Molten wax was poured on a wooden board of 18 cm by 18 cm and left for the wax to cool. Any wax on the back of the board was removed with a razor blade or by melting it with a heat gun. The wax-coated board was placed on two rails of bare wood of the same thickness as the base wooden substrate, with the rails positioned

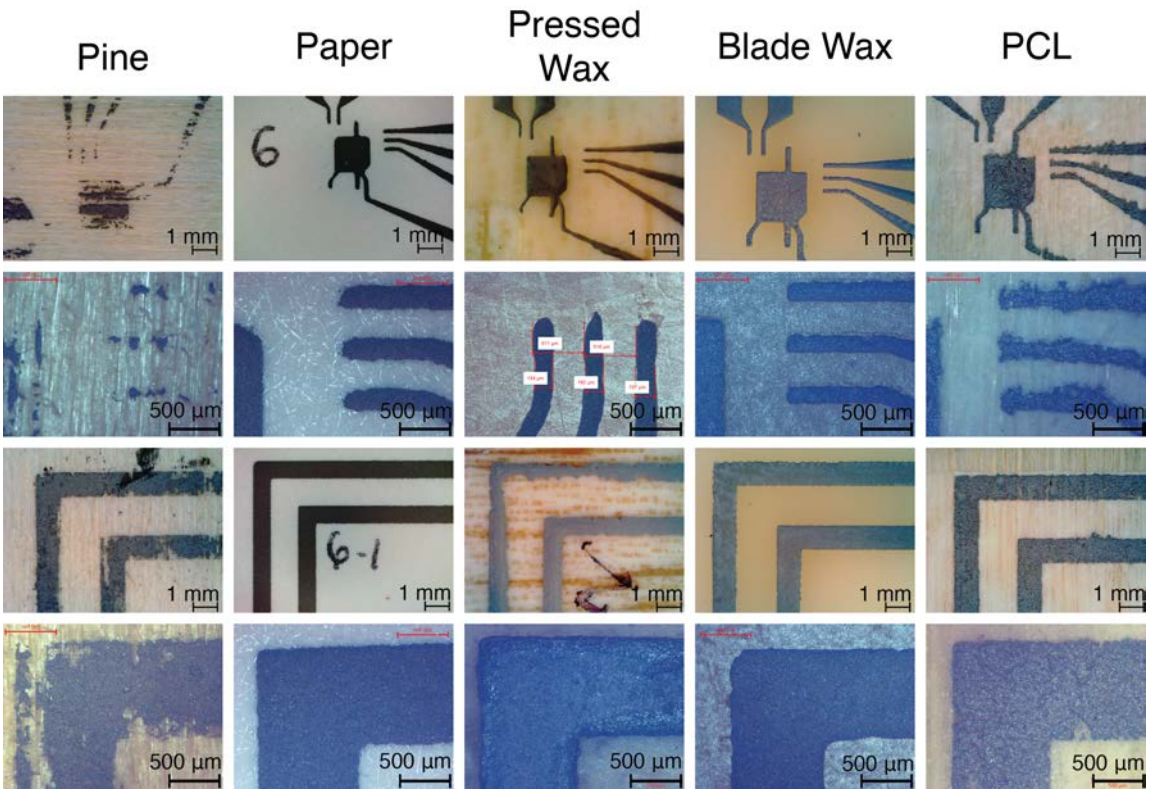

Figure 2.4: Although large features print decently well on all substrates, fine features and edge roughness are improved when printing on smoother substrates: blade coated wax, pressed wax, and PCL-coated wood as compared to raw wood or soaked wood.

under the runners of the doctor blade. This allowed the final thickness of the wax to be controlled by the height of the blade. The hot blade moved across the wax surface, melting the wax. Some of the re-melted wax ran off the side, while other areas reflowed and covered lower spots in the substrate. The resulting wax layer had surface roughness of less than 1 µm excluding anomalies, which was much smoother than any other technique. However, the blade cooled as it moved, so the depth to which the wax melted changed across the length of the pass, leading to variations in final wax layer thickness. Additionally, large variations in initial pour height created lasting hills and valleys, which sometimes caused misprints that are discussed below.

To avoid the changes in melting temperature over time that cause thickness variations, a ski waxing iron with controllable temperature was used in place of the doctor blade. However, the iron lacked the height-control of a doctor blade, and instead

came in direct contact with the wood. Thus, the wax melted to the surface of the board, creating a surface with roughness of about 7 μm, similar to that of untreated pine wood.

Instead of wax, which must be heated in order to flow, a solution of a biodegradable polymer can be used as the planarization layer. In this technique, a solution of 1:8 PCL:anisole by mass was applied using a doctor blade at room temperature. After coating, the anisole solvent dried, leaving behind a thin film of PCL. The smoothness of this layer depended on its thickness because the layer must be thick enough to fill in the valleys in the wooden substrate. This technique can significantly reduce surface roughness, especially in the direction parallel to the wood grain. A disadvantage of this technique is that the substrate material is the same as the ink, so it can be partially dissolved by the ink's solvent. Features printed on PCL-on-wood had good definition but showed some bleeding along the direction of the wood grain, as shown in the rightmost column of figure 2.4.

Thickness and Uniformity

In screen printing, the substrate is mounted on a sample plate which is loaded under the screen. The ink is flooded across the mesh while the screen is held well above the substrate. The screen is then lowered to a position slightly above the substrate. The distance between the screen and substrate, typically no more than a millimeter, is known as "snap-off" and is an important parameter for print quality. During the print, the squeegee depresses the screen so that it makes contact with the substrate, transferring the ink from the screen to the substrate. As the squeegee passes, the already-printed area of the screen snaps back to its set height.

This mechanism works well only if the substrate is the same distance below the screen at all x-y locations. Tilted or wedge-shaped substrates will print differently left-to-right or top-to-bottom. Substrates with hills or valleys will have misprint areas or areas that do not print at all if the squeegee cannot press against part of the substrate.

For each substrate type and wax-coating process, the macro-scale waviness and thickness variations are important as well as the micro-scale roughness. Raw pine and balsa had even thickness from planing by the manufacturer. Paper was also produced with even thicknesses. Hand-pressed wax had uneven thickness when pressure was not applied uniformly during pressing. Blade coated wax had significant thickness variation; the thickest part of a board was typically 0.3 mm thicker than the thinnest part Soaking and ironing wax produced substrates with the same dimensions as the original boards. Thus, the techniques used to create smooth surfaces are more likely

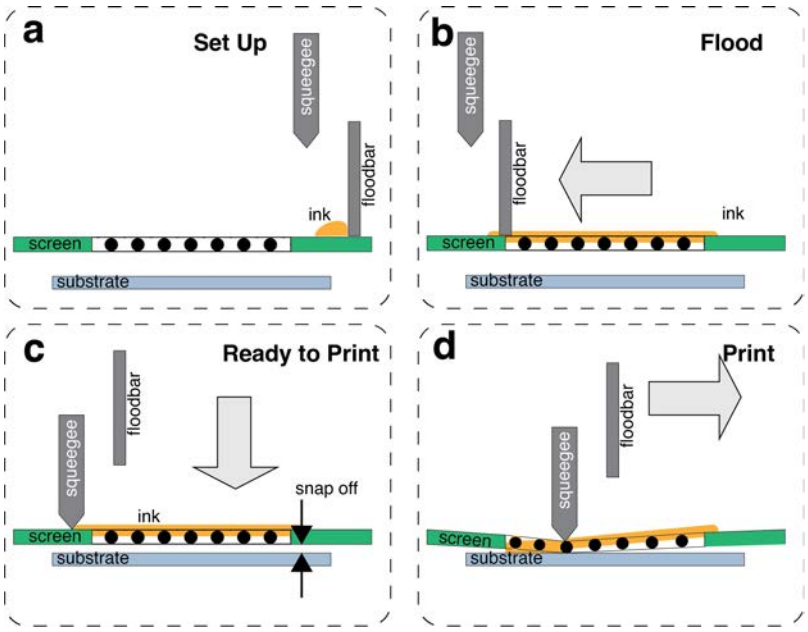

Figure 2.5: a) At the beginning of a print, ink is deposited on the screen just in front of the flood bar. The screen is held above the substrate. b) During the flood stage, the flood bar pushes ink across the screen, and the ink partially fills the holes in the mesh. c) Prior to printing, the screen is lowered so that it is almost–but not quite–touching the substrate. The gap between the screen and substrate is controlled parameter known as the snap-off. d) During the print, the squeegee moves across the screen, pressing the mesh down so that it touches the substrate. As the squeegee passes, ink from the holes in the mesh is deposited on the substrate. The tension of the screen causes it to snap back to its original height. Ink deposited on the substrate spreads out until it dries.

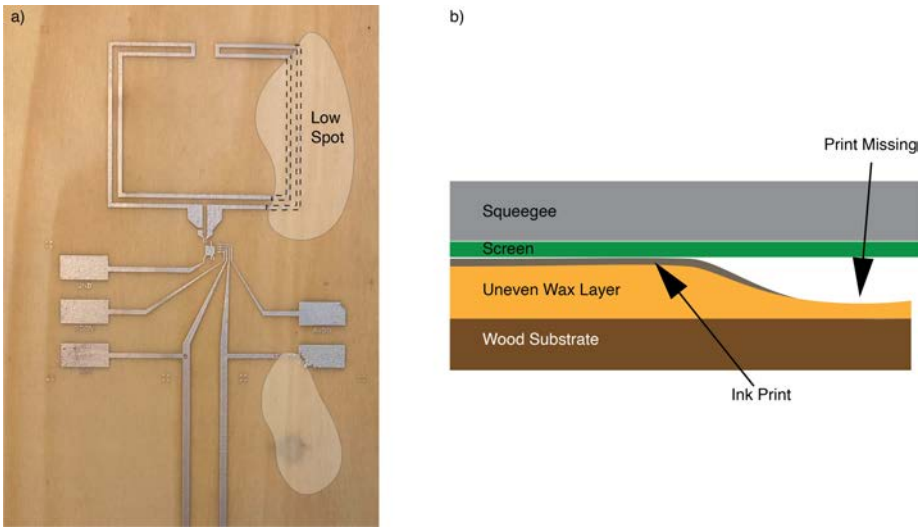

Figure 2.6: a) A substrate with uneven thickness has areas that did not print. b) A cross-sectional view of an uneven substrate illustrating how thickness variations can cause misprints like the one seen in (a).

to create uneven thickness, but both smooth and uniform substrates are needed for printing fine features over large areas.

None of the substrate preparation techniques are ideal for every scenario. To create a large number of small substrates for process optimization, a large board can be treated with blade-coated wax, then cut into smaller samples. This provides a very smooth surface to each sample, and the thickness variation can be managed by measuring the actual thickness of each sample and adjusting the screen printer settings for each sample. For large-area substrates, an improved mechanism that offers both uniform temperature and controlled blade height is needed.

Surface Energy

Ink spreading is defined by the surface energy of the substrate, the surface tension of the ink, and the ink's viscosity. At equilibrium, the contact angle of a drop of liquid on a solid surface is given by

$$\gamma_s = \gamma_{s-l} + \gamma_l cos(\theta) \tag{2.1}$$

where γ_l is the surface tension of the liquid, γ_s is the surface energy of the solid-air interface, and γ_{s-l} is the energy at the surface between the solid and the liquid.

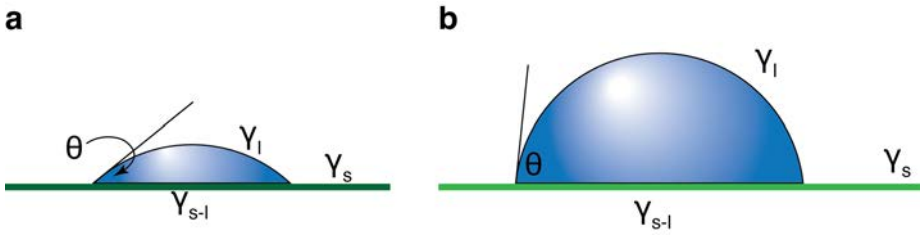

Figure 2.7: The amount of spreading of a drop of liquid, including inks, is determined by the surface tension of the liquid, γ_l, the surface energy of the solid-air interface, γ_s, and the energy at the surface between the solid and the liquid, γ_{s-l}. The contact angle of a drop on a solid surface is used to quantify surface energy. a) High surface energy, low contact angle substrate. b) Low surface energy, high contact angle substrate.

On substrates with high surface energy, the molecules in the liquid are attracted to the substrate, the drop spreads out, and a low contact angle is observed, as shown in figure 2.7a. The reverse is true for substrates with low surface energy, illustrated on the right in figure 2.7b. Systems with low contact angles have higher adhesion between ink and substrate.

When ink first lands on a surface, it has an initial contact angle, then the ink spreads out until the lowest energy state is reached according to equation 2.1. Inks with low viscosity quickly spread to their equilibrium position, so the difference between initial and final contact angle very challenging to measure. High-viscosity inks spread more slowly, drying as they do. Attention is most often payed to surface energy modification for controlling spreading of thin inks for inkjet printing and doctor blade coating because they spread rapidly [35]. However, surface energy still impacts spreading of screen printing inks.

During optimization of ink properties and printing processes, PET was used as a control substrate for its smooth surface, availability, and because it has been well studied. When changing substrates from PET to wax-soaked wood, surface energy comparisons between the substrates were needed to understand how this change would impact print quality and adhesion. In order to study this, videos of a drop of ink spreading on PET, wax-dipped PET, and wax-soaked wood were taken. The wax-dipped PET had a very smooth surface (roughness of about 0.12 μm) so differences between PET and wax-dipped PET were primarily due to the surface energy differences of the two materials. The wax-soaked wood had a rougher surface, as described above, so spreading differences between smooth wax and wax-soaked wood were due to surface roughness.

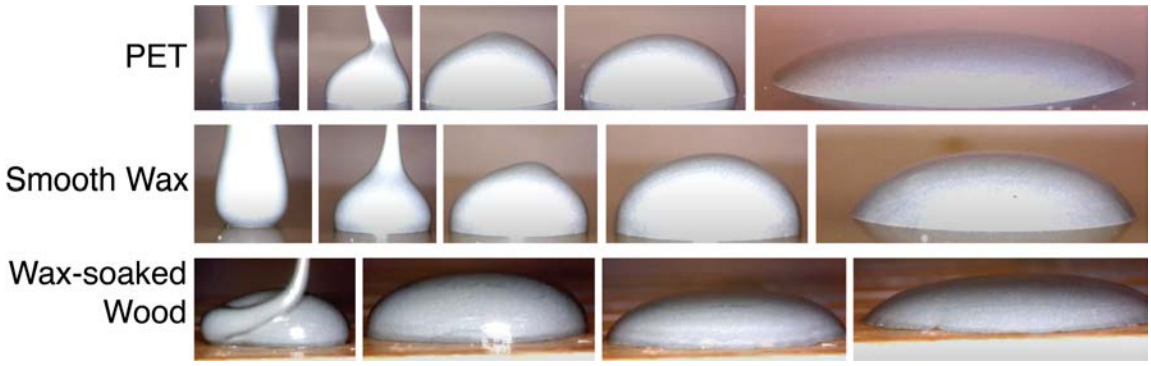

Figure 2.8: Zinc ink spreading on (top row) PET substrate, (middle row) PET dipped in beeswax to create a smooth wax surface, and (bottom row) balsa wood soaked in beeswax to create a rough waxy surface. From initial contact to final steady state formation, the contact angle shrinks.

Table 2.2: Surface energy and contact angle of PET and wax

Substrate	Initial Angle	Final Angle
PET	80.5	44.2
Smooth Wax	89.4	47.0
Wax-soaked wood	87.1	42.5

All three substrates started with contact angles above 80°, and reached equilibrium after about 45 seconds. Figure 2.8 shows screenshots of ink spreading on the three substrates from the moment of contact until 1 minute later. The increased drop diameter and corresponding decrease in contact angle over time is evident.

The wax substrates had somewhat higher initial contact angles. Because the ink was very viscous, it spread slowly and dried quickly in the small volumes used for screen printing. Therefore, the initial contact angle was the primary determinant of slump. Given the higher initial contact angle of ink on wax, we expected features printed on wax-soaked wood to spread slightly less than on PET, which was indeed observed. Test features printed on PET with designed width of 500 μm were measured at 620 μm, or 120 μm spreading, while the same features printed with the same ink on wax-soaked wood measured just under 500 μm.

Temperature Limits

The glass transition temperature of polymers, and the melting temperature of polymers or waxes dictate maximum processing temperatures for subsequent steps. Below its glass transition temperature, a polymer is glassy and brittle, while above that temperature, it is soft and rubbery. If a pattern is printed on a polymer in its glassy phase, and later transitions to the soft phase and back again from temporary exposure to heat, the pattern can warp. The glass transition temperature of PCL is $-60°C$, so it is in its soft phase at room temperature, and crossing the glass transition is not a concern. PCL melts at about 60°C . PVP's melting and glass transition temperatures are between 150-180 °C . Beeswax melts at 63°C . The similar melting temperatures of PCL and beeswax cause some challenges in fabrication because the wax needs to be melted in order to flow, but molten wax can also melt the PCL.

Biodegradability

Substrate materials need to be biodegradable, but robust enough to last through a growing season. They must not cause harmful ecological impacts or hinder plant growth. Refer to table 1.3 for suitable materials. PHBV, balsa wood, beeswax, and soy wax have all been shown to have no adverse effects on corn growth. [62].

Solvent Compatibility

It is desirable to have a substrate which is not readily dissolved by the solvent in the ink or any chemical used in the processing of the printed traces. For example, a later step in the room-temperature zinc process involves treatment with a solution of acetic acid in water. Water soluble plastics are thus not suitable substrates for zinc traces fabricated in this manner.

Wood is not a polymer and cannot undergo the physical change of dissolution, though it can be chemically or biologically broken down. Time scales for significant wood breakdown in chemicals that are used as polymer solvents are typically significantly longer than the wet exposure times of most printing processes. Additionally, the hydrophobicity of wax is an advantage as wax will not be degraded by water. Wax can be slowly dissolved by some solvents, acetone for example.

2.2 Ink Formulation

Zinc ink, like all inks, has a filler, a binder, and a solvent. Zinc ink was not commercially available, so the ink optimization for printing was necessary. This involved

selecting the materials used as binders and solvents which print well without clogging the screen and have good adhesion to the substrate. Solvent to binder to filler ratios were also adjusted to achieve an ink with the desired viscosity, adhesion, and conductivity.

Filler

The filler is the metal. In this case it was powered zinc, 5 μm diameter or smaller (1–5 μm particle size, Goodfellow Co). This was held constant throughout the ink optimization process. In most formulations, it made up more than 75% of the ink by mass.

Binders

Binders are polymers which hold the conductive particles in place and glue everything together. Important properties of biodegradable binders for zinc ink are their solubility in various solvents, the processes through which they degrade and the rate of degradation, and their glass transition and melting temperatures.

An ink's binder should be chosen for the properties it offers to the finished printed trace. Depending on the application, this might include thermal or chemical stability, flexibility, or adhesion. In the case of zinc ink for biodegradable agricultural sensors, the binder should provide the ink with physical stability during wet chemical processing, long lifetime, and eventual biodegradability. The printability of the ink–its viscosity, surface tension, and drying time–can be tuned by choice of solvents and additives after a binder has been selected.

This work used PVP and PCL binders. PVP was chosen to because it had been demonstrated in the literature [50, 63]. PCL was chosen because of its relatively slow degradation and stability in water. The impact of the binder on ink conductivity and lifetime is discussed in section 2.4 on acid treatment.

Solvents

The filler and binder are dissolved in a solvent to create an ink. Important aspects of a solvent are its ability to dissolve the binder, its viscosity, the manner and speed it dries, its compatibility with substrates and other materials, and its toxicity to people and the environment, each of which is discussed in more detail below. The solvent evaporates completely after printing, so it does not directly impact processes that follow. However, because the solvent does greatly impact the print, it influences the

profile of the printed traces, which in turn impacts the rest of the processing and operation of the device.

Ability to Dissolve the Binder

The most important function of a solvent is to dissolve the binder. Different binders are more or less soluble in different solvents depending on the chemical characteristics of both the binder (solute) and the solvent. Generally speaking, "Like dissolves like." The Hansen Solubility Parameters quantify three properties of solvents–polarity (P), dispersion (D), and hydrogen bonding(H)–which are key aspects of solubility. These numeric values formalize the degree of "likeness" between a solvent and a solute. The parameters of many solvents are listed in databases which can be used to find solvents with similar properties [64].

PVP is soluble in water and polar solvents, including isopropyl alcohol (IPA) and n-methyl-2-pyrrolidone (NMP). According to a study by Bartnikowski, PCL is soluble in toluene, benzene, chloroform, cyclohexanone, carbon tetrachloride, tetrahydrofuran (THF), dimethyl carbonate (DMC), dioxane, 2-nitropropane, and dichloromethane (DCM), and partially soluble in acetone, ethyl acetate, dimethyl formamide (DMF), 2-butanone, and acetonitrile, [65], while others have dissolved PCL in anisole [66, 46]. These good solvents for PCL have relatively high D, low to moderate P, and low to moderate H.

The theory provides a starting point for solvent selection, but experiments are still needed to understand how a combination of solvent and binder behaves as an ink. The dissolution of polymers in solvents is more complicated and slower than the dissolution of small molecules. Polymer dissolution takes place in two steps: first the solvent diffuses into the pore spaces within the polymer, creating a swollen layer near the interface. Next, the polymer chains disentangle, completing the dissolution. Increased temperature can speed up this process as the polymer chains relax. Stirring also makes the process faster as the solvent diffusion is followed immediately by polymer desorption, without the buildup of a gel layer on the surface [67]. Because polymers dissolution can take up to a few days, it can be advantageous to study pre-mixes of solvent and binder before studying complete inks. The pre-mix gel can later be mixed with zinc powered to create ink as it is needed.

Pre-mixes of PVP were successfully made with isopropyl alcohol and NMP. Differences in ink behavior of these inks was primarily due to different drying properties of the solvents, as discussed in the following subsection.

Six solvents for PCL were tested as pre-mixes. The three which made gels were also tested as screen printing inks. The six solvents used were NMP, toluene, acetone, DMSO, ethyl alcohol, and anisole. Each solvent was mixed with a one to eight by

Table 2.3: Hansen Solubility Parameters and hazards for solvents, data from [64, 68]

Chemical	D	P	H	Boiling Point	Safety Score	Health Score	Env. Score	Ranking after discussion
Water	15	16	42.3	100	1	1	1	Recommended
IPA	15.8	6.1	16.4	82	4	3	3	Recommended
Acetone	15.5	0.4	7	56	5	3	5	Recommended
Ethyl Alcohol	15.8	8.8	19.4	78	4	3	3	Recommended
Ethyl Acetate	15.8	5.3	7.2	77	5	3	3	Recommended
Anisole	17.8	7.8	6.7	154	4	1	5	Recommended
NMP	18	12.3	7.2	202	1	9	7	Hazardous
Toluene	18	1.4	2	111	5	6	3	Problematic
Benzene	18.4	0	2	80	6	10	3	High hazard
Chloroform	17.8	3.1	5.7	61	2	7	5	High hazard
Cyclohexanone	17.8	8.4	5.1	156	6	3	7	Problematic
CCl4	17.8	0	0.6	77	2	7	10	High hazard
THF	16.8	55.7	8	66	6	7	5	Problematic
DCM	17	7.3	7.1	40	1	7	7	Hazardous
DMSO	18.4	16.4	10.2	189	1	1	5	Problematic

weight ratio of PCL to solvent. As expected from solubility reported in the literature, DMSO and EtOH did not dissolve the PCL,as shown on the right in figure 2.9. NMP and acetone were able to dissolve PCL to form a gel at 40°C . At room temperature, this gel solidified into a solid, which could be liquefied with gentle heating. The solidified Acetone:PCL mixture is shown on the left in figure 2.9. Anisole and toluene dissolved the PCL, and remained as gels at room temperature, as shown for anisole in figure 2.9, the white pellet in the vial was a magnetic stir bar.

The PCL pre-mixes of NMP, toulene, and anisole were used to make inks with 30:1:8 Zn:PCL:Solvent ratios by weight. The NMP-based ink was warmed before printing, but the ink cooled rapidly when it was spread in a thin layer across the screen. It re-solidified, clogging the screen after one print. The toulene ink also dried or cooled after 1-2 prints. The anisole ink stayed wet for up to 12 passes, so it was chosen as the solvent for Zinc:PCL ink.

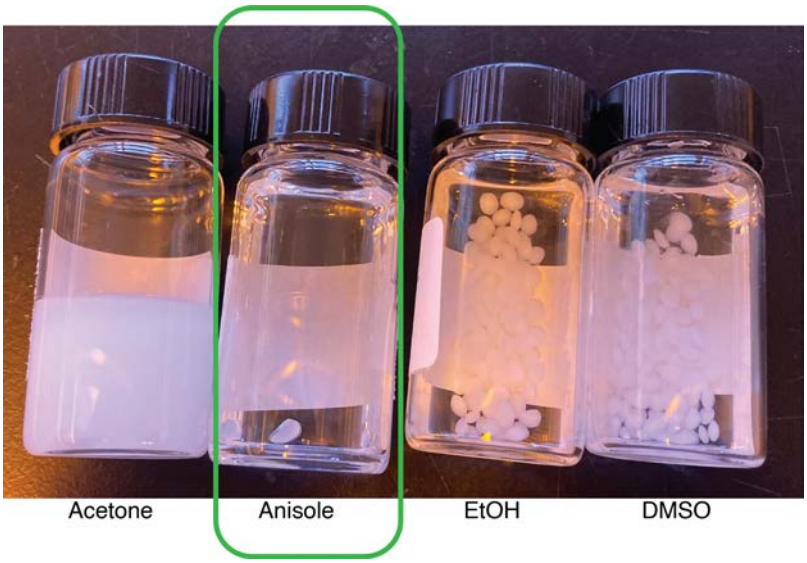

Figure 2.9: 1:8 by weight PCL in acetone solidifies at room temperature. 1:8 PCL in anisole dissolves well. 1:8 PCL in Ethyl Alcohol and and 1:8 PCL in DMSO does not dissolve.

Drying Properties

Screen printable ink should dry slowly to enable many prints before ink on the screen dries and clogs the mesh. Commercial inks use additives to slow drying. This adds more complexity, so basic homemade inks typically rely on choice of solvent to control drying properties. For materials which are good solvents for their solute, the boiling point provides information about how quickly the solvent will dry. Liquids with higher boiling points require more energy to evaporate and will dry more slowly. For example, both IPA and NMP are good solvents for PVP. NMP has a boiling point of 202°C while IPA has a boiling point of 82°C . PVP:IPA inks dried after about one minute, or 1-2 prints, while PVP:NMP inks stayed wet for at least 24 prints, about 15 minutes or more.

Toxicity

In addition to their functional properties–solubility parameters and boiling points– the hazards and toxicity of solvents should be considered when designing an ink. Many effective solvents for PCL include chlorinated solvents which present significant health and safety risks. The Globally Harmonized System of Classification

and Labelling of Chemicals is a way of communicating chemical hazards through pictographs and numbered warnings for specific dangers such as flammability, explosiveness, and radioactivity. Industry consortia, such as GSK and CHEM21, have ranked chemicals for environmental, physical danger, and human health concerns. Table 2.3 includes CHEM21 ratings for the three risk categories: environmental, physical danger, and health. Higher numbers correspond to higher risk. In the table, cyclohexanone and anisole have similar solubility parameters and boiling points, indicating either could be use as a solvent for PCL, but anisole has lower risk numbers, so it is preferred over cyclohexanone.

Viscosity

Viscosity is a fundamental property of a solvent, but when mixed with a polymer, viscosity becomes a function of the solvent-to-binder ratio. Generally, the more binder is present, the more viscous the liquid or gel, up to the solubility limit of that binder in that solvent. If a material is not very soluble in the chosen solvent, it may not be possible to achieve a high viscosity.

The thickness and shape of the wet ink deposit produced by screen printing is set primarily by the parameters of the screen, and can be influenced by the squeegee pressure and height [69]. The ink viscosity primarily impacts the spreading of wet ink after the squeegee passes. Inks with low viscosity will spread, or "slump" significantly during the time between ink deposition and ink drying. Slump creates final features which are shorter and wider than desired, and can be especially problematic for fine features where resolution is key. Higher viscosity inks limit slump by slowing the flow rate of ink after deposition, allowing the ink to dry on the substrate before it spreads to the equilibrium contact angle.

Prior to printing, the rheology of Zn:PVP:NMP inks with various binder-to-solvent ratios was studied by my collaborators Sui et al. [63]. Inks were identified by the weight ratios of zinc to PVP to NMP, for example, 30g zinc to 1g PVP to 6g NMP (30:1:6). Inks' viscosity at low shear rates increased with increased PVP concentration, from 12 Pa-s for 30:1:7 ink to 300 Pa-s for 30:1:4 ink. The inks with higher solid loading experienced greater shear thinning, while less viscous inks tended toward Newtonian behavior. In thixotropy tests to simulate shear rates experienced during screen printing (rest, high shear during the squeegee pass, low shear during slump) the inks with higher solid loading took more time to regain their resting viscosity. The viscosity studies showed 30:16 Zn:PVP:NMP to be the most printable ink [63]. With these rheology results, we turned to printing studies.

The top micrograph in figure 2.10a shows printed 30:1:6 Zn:PVP:NMP on PET substrate which should be nominally 500 μm wide. The lower micrograph in the

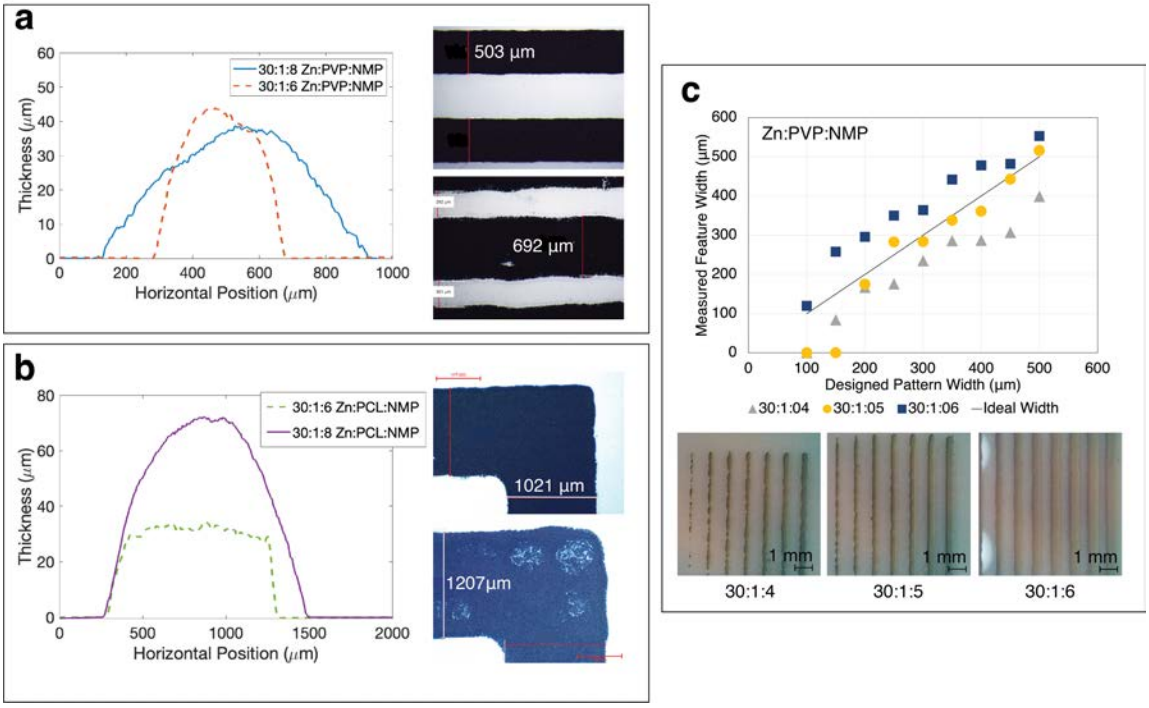

Figure 2.10: a) Nominally 500 μm lines printed in 30:1:6 Zn:PVP:NMP are relatively smooth with minimal spreading (top inset). Nominally 500 μm lines printed with 30:1:8 Zn:PVP:NMP have significant spreading and uneven edges (lower inset). The slump of the less viscous ink is readily apparent in its pyramid shaped profile, while the more viscous ink has straighter sidewalls and a somewhat more uniform thickness. b) Zinc ink with PCL binder shows similar trends, shown here for a nominally 1 mm wide trace. 30:1:8 ink has a rounded profile and wider footprint than 30:1:6 ink. The more viscous ink creates prints with solid features (top inset), while the less viscous ink has porous areas (bottom inset). c) Quantifying the spreading seen when printing fine features (down to 100 μm wide) in Zn:PVP:NMP inks. 30:1:6 has about 80 μm of spreading, 30:1:5 gives features near the desired width, and 30:1:4 features are about 60 μm narrower than desired.

same figure shows similar 500 μm lines printed with 30:1:8 ink. The 30:1:8 ink had more solvent, so was less viscous, and slumped more between deposition and drying. This resulted in considerable ink spreading: the lines are about 150 μm or 30% larger than designed. The profiles in figure 2.10a are of representative 500 μm traces printed with both inks. The slump of the 30:1:8 ink was clearly visible in its broader, pyramid shaped profile. There was not a flattish area in the center of this print, as is normally observed for clean prints. The 30:1:6 ink was narrower and slightly taller, with sidewalls that were steeper; all in all this was a higher quality print. Figure 2.10b shows a similar pattern for PCL-based ink. The top micrograph is the more viscous 30:1:6 Zn:PCL:NMP ink, with solid printed traces, crisp edges, and trace width of 1.02 mm, for a designed trace of 1 mm. The bottom microgaph in figure 2.10b shows the same feature printed with less viscous 30:1:8 Zn:PCL:NMP, which spread to 1.2 mm in width and had somewhat porous areas. The profiles show the spreading of the less viscous ink and its slumping shape, compared to the more even thickness and defined sidewalls of the more viscous ink.

The impact of viscosity on trace width is further quantified by narrow test features between 100 μm and 500 μm design widths in figure 2.10c. The least viscous ink (30:1:6) created features which were nearly 100 μm wider than designed. The most viscous ink did not flow easily through the mesh and features were about 20-100 μm narrower than designed. Ink with 30:1:5 produced lines whose widths were approximately equal to the designed width.

Tuning of the solvent:binder ratio is unique for each solvent-binder pair, and depended on the viscosity of the solvent, the properties–such as molecular weight–of the polymer, and the solubility limit of the polymer in the particular solvent. For zinc:PVP:NMP inks, 30:1:5 was chosen for printing, while zinc:PCL:anisole, 30:1:8 was used, which produced profiles described in more detail in section 2.4 and figure 2.14.

2.3 Printing

The screen printing process overview is illustrated in figure 2.5. It involves flooding ink across the mesh, the squeegee pushing the ink in the mesh in contact with the substrate, and the release of the screen from the ink. Primary process control variables are snap-off, flood pressure, flood speed, squeegee pressure, and print speed. Printing parameters must be optimized for each ink formulation. Printing parameter adjustment is process optimization, not novel research, but poor quality or misprinted samples are unsuitable for further tests, so the optimization is important.

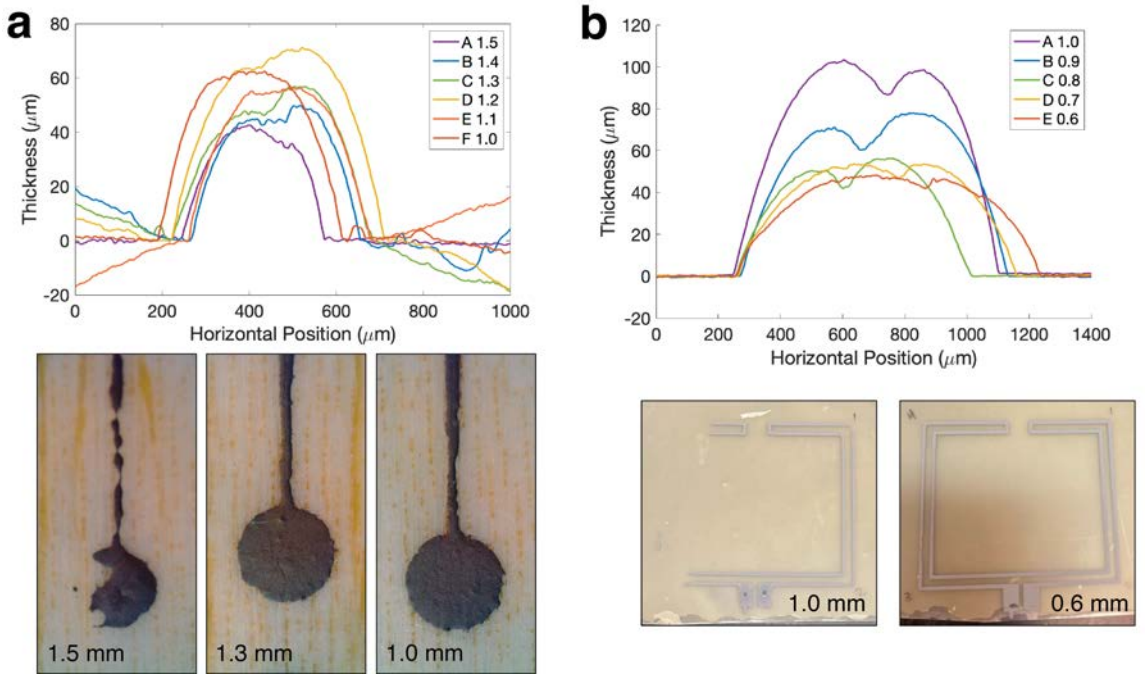

Figure 2.11: With well-adjusted snap off, the full pattern prints and thickness is uniform across the width of the printed trace. When snap off is too high, the thickness is greater, but the print is poorly controlled. a) 500 μm wide traces of zinc on wax-soaked balsa wood with varying snap off. b) 1 mm wide traces of zinc on blade-coated wax substrates with varying snap-off.

Snap Off

Snap off is the distance between the screen and the substrate when the squeegee passes. If the snap off is too high, there is a significant distance between the squeegee and the substrate, which creates thick but poorly controlled traces, as shown in figure 2.11. In places where the substrate is low and the snap off is high, no ink will be deposited. If the snap-off is too low, the mesh patterns are pressed against the substrate, and messy edges can result.

Pressure and Speed

Print and flood speed also impact print quality. For more viscous inks, slower print and flood speed produce higher quality prints because the ink has more time to flow.

Printing high-viscosity inks at high speed can cause gaps in printed traces.

2.4 Acid Treatment Conditions

Once a printable ink formulation has been developed, and printing conditions optimized, the printed trace needs to be treated to become conductive. In silver and gold inks, thermal or photonic sintering is used to transform a matrix of discrete metal microparticles into a continuous conductive pathway. Treatment of zinc ink is more complicated for two reasons. First, the thermal budgets of biodegradable polymers and waxes do not allow for thermal sintering. Second, an more importantly, zinc forms a passivisation layer of zinc oxides, hydroxides, and carbonates. This passivisation layer forms a shell around each discrete zinc microparticle. A freshly printed trace of zinc microparticles in a binder is not conductive because the metal particles are isolated from each other, as illustrated in Figure 2.12a. Lee et al. described a room temperature chemical method to create conductive zinc traces, which has been further studied and adapted by Majee et al, Jayasayee et al., and Sui et al. [50, 51, 70, 63].

Zinc oxides, hydroxides, and carbonates are soluble in acidic solutions. When a printed zinc trace comes in contact with dilute acetic acid, the acid dissolves the passivisation layer, exposing the zinc, as in equation 2.2

$$\mathrm{ZnO} + 2\mathrm{H}^{+} \rightleftharpoons \mathrm{Zn}^{2+} + \mathrm{H_2O} \tag{2.2}$$

The exposed zinc releases Zn^{2+} ions into solution. Some of these Zn^{2+} are chelated with acetate, influencing the equilibrium point of the equation 2.3

$$\mathrm{Zn}^{2+} + 3\mathrm{oAc}^{-} \rightleftharpoons \mathrm{Zn(oAc)}_3^{-} \tag{2.3}$$

and driving self-exchange between zinc in solution and zinc solid. The dissolution and deposition of zinc allows atoms to relocate, forming connecting bridges between particles. When the acetic acid solution evaporates, and new passivation layer, including zinc acetate, forms around the zinc matrix, and the distinct particles have been connected to form a conductive network, as shown in figure 2.12b [50, 51, 70]. This process depends on acetic acid concentration, wet time or dose, drying conditions, and the polymer used as the ink's binder. These variables interact with each other in complex ways. For example, the optimal treatment time depends on the acetic acid concentration used, and both of these parameters are different for inks with different polymer binders.

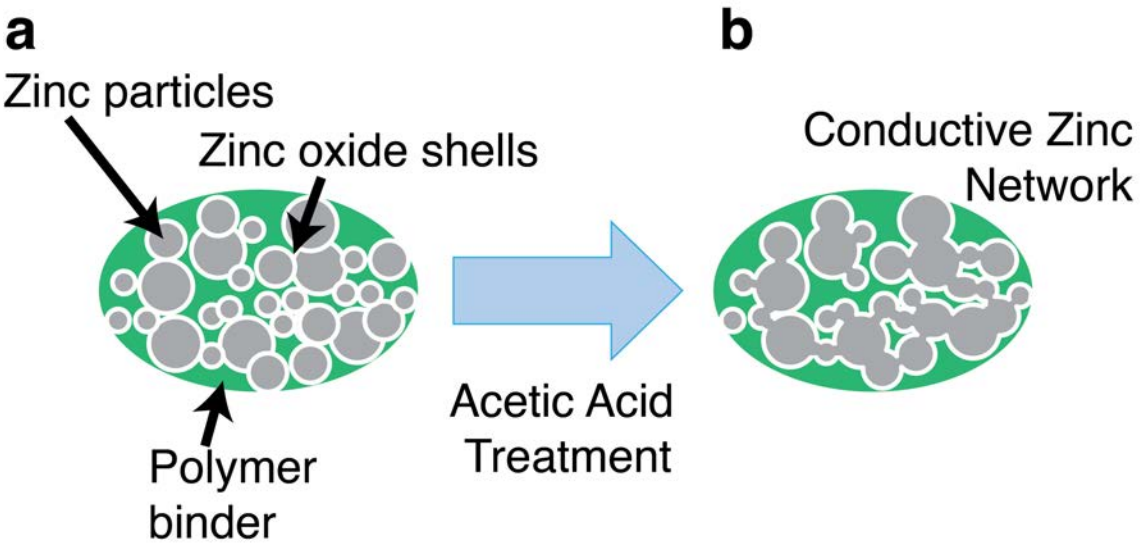

Figure 2.12: a) As-printed zinc ink consists of discrete zinc micro particles, each with an oxide shell. This matrix is not conductive. b) After treatment with a solution of acetic acid, which reacts with the oxide layer, a conductive network of zinc is formed. A new passivisation layer forms on the outside of network.

In the literature, low-temperature acetic acid treatment of printed traces has been reported by three groups, whose experiments and key findings are summarized in table 2.4. The foundational paper of Lee et al. used a PVP binder and an isopropyl alcohol solvent, with drop casting as the deposition technique for acid solution. This work centered on the chemical conditions that allow for low temperature chemical sintering, comparing different metals and types of acid solutions. They did not present optimization of zinc ink formulation, printing, acetic acid concentration, or time [50]. Sui et al. used the concepts from Lee and optimized screen printable zinc-PVP ink with an NMP solvent. They further developed an inkjetting method for acetic acid solution deposition, which was more controllable than drop casting. Acetic acid concentration was kept at the 9% reported by Lee, and many passes with the inkjet printer were found to be needed for high conductivity. Curing at 45°C was found to produce higher conductivity traces than room temperature drying [63]. Similarly, Majee et al. adapted Lee's original chemistry, optimizing both the zinc ink and the acetic acid solution for inkjet printing. They used a PVB binder and combination of solvents and surfactants to achieve zinc ink properties suitable for

jetting. In acid treatment optimization studies, they found different results from Sui: a single inkjet pass gave optimal conductivity. They also varied acetic acid concentration and identified 3-10% as the optimal range. Curing was done at elevated temperature, with the lowest temperature reported of 60°C [71]. Both inkjet printing papers report slightly lower conductivity than the original drop-casting paper.

In this work, we optimized acid treatment conditions for PVP- and PCL-based inks. PCL-based inks were able to withstand harsher treatment conditions, which enabled higher conductivity.

Wet Time, Concentration and Application Method: PVP

When working with PVP, we first compared acetic acid application by spray coating to drop casting volumes around 20 μL. Samples were stencil printed by hand using laser cut stencils and a razor blade to apply 30:1:10 Zn:PVP:IPA ink. Spraying used 5% acetic acid by volume, and was done with an airbrush by hand. Samples were dried at 45-50°C for one minute before measurement. Conductivity was measured after each pass with the airbrush, and the maximum conductivity achieved was about 0.5 S/m, after four passes. The acidic solution corroded the metal airbrush. We also used a pipette to drop cast about 20 μL of 5% solution along the 50 mm length of a 1 mm wide trace. These samples were dried at room temperature. Conductivity for this method was about 100-200 S/m. Because of the low conductivity acheived with spray coating and low-volume drop casting, we sought methods for applying greater volumes of solution.

Dipping is a simple and repeatable high volume solution treatment method. One key variable in dipping is the wet time, which was optimized in the following way. Zinc ink (30:1:5 Zn:PVP:NMP) was printed on wood soaked in beeswax and smoothed either by pressing while wet or by heated-blade reflow. Some samples used a 1 mm wide by 320 mm long folded trace, while others were straight rectangles, either 0.5 mm, 1 mm, or 10 mm wide by 50 mm long. Samples were treated with 9% acetic acid solution for times ranging from 10 seconds to 4 minutes. After removal from the acetic acid solution, samples were dried at room temperature. Some samples were dried with a nitrogen gun for about 5 minutes, while others were left in ambient conditions for at least 15 minutes. Treatment time optimization was repeated for five batches on different days with different line widths. For most batches, the highest conductivity was achieved with dipping times of 1-3 minutes. Wet times longer than 3 minutes resulted in marked decreases in yield. The highest conductivity achieved with PVP ink was 1.5×10^5 S/m, which is comparable to that reported by Majee et al. but about three times lower than the highest conductivity found with PCL-based ink[71].

Table 2.4: Comparison of zinc/acetic acid processes in literature

Reference	Lee[50]	Majee[51]	Sui[63]	This Work	This Work
Substrate	PLGA	PET	Glass	Beeswax	PET
Binder	PVP	PVB	PVP	PVP	PCL
Solvent	IPA	EGBE and DPG[1]	NMP	NMP	Anisole
Ink Ratio (Zn:Binder:Solvent)	30:1:10	40.8:1:40.5:17.4	30:1:6	30:1:6	30:1:8
Printing method	screen?	inkjet	screen	screen	screen
Thickness (μm)	50	20	50	30	38
Vary Acid Concentration?	no	yes 0-100%	no	no	yes: 9-50%
Best Acid Concentration	9%	5%	9%	9%	50%
Acid Application	drop	inkjet	inkjet	dip	drop
Vary Acid Dose?	no	yes 1-10 passes	yes 1-20 passes	yes 10-240 sec	yes 1-17 min
Best Acid Dose	10 sec	1 pass	10 passes	120 sec	13 min
Vary Curing Temperature?	no	yes 60-150°C	yes 25-45°C	no	yes 40-65°C
Best Curing Temperature	room	60°C	45°C	room	45-55°C
Conductivity	3.0E5 S/m	1.0E5 S/m	4.0E4 S/m	1.5E5 S/m	4.0E5 S/m

[1] ethylene glycol butyl ether and dipropylene glycol

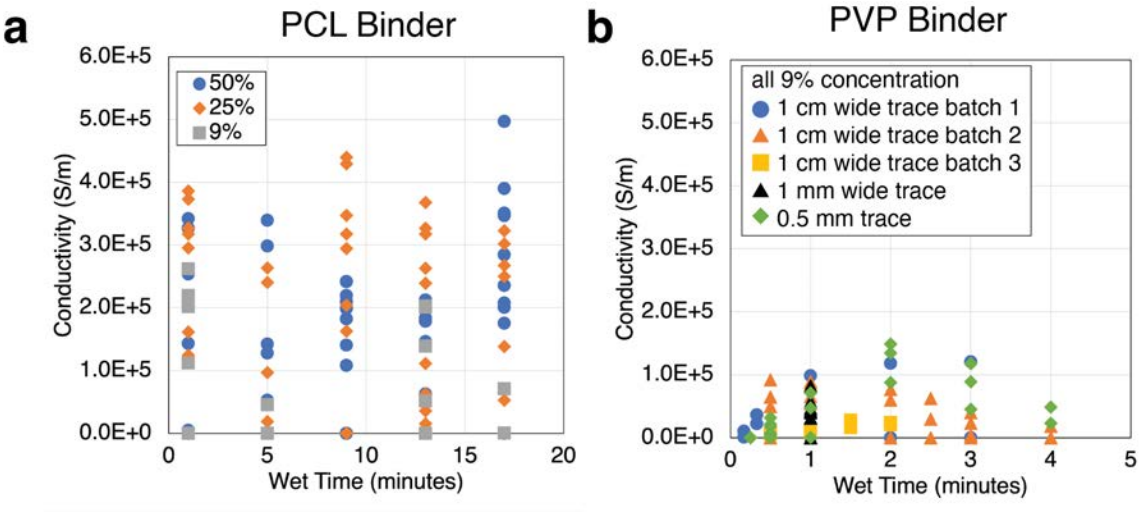

Figure 2.13: a) Ranges of conductivity of printed 30:1:8 Zn:PCL:Anisole traces on PET as a function of acetic acid concentration and time. (This is the raw data which was averaged to produce figure 2.15b. Although conductivity varies significantly within each treatment, most samples in the high and moderate concentration treatments have conductivity above 1 $\times 10^5$ S/m. By contrast, b) shows that the highest conductivity achieved for 30:1:6 Zn:PVP:NMP inks on wood/wax substrates is 1 $\times 10^5$ S/m, while most samples are less conductive than that.

These PVP-based samples also showed significant batch-to-batch and within-batch variation in final conductivity. Some of this variability can be explained by poorly controlled parameters during drying, which is described in more detail in section 2.5.

Acetic Acid Application Method: PCL

We compared dip-treatment to drop casting with a 1-mL syringe, using 50% acetic acid solution and 13 minute wet times for both cases (N=8). No significant difference was found in conductivity, though drop-casting had slightly higher yield. Conductivity for the drop casting method was 1.4 $\times 10^5$ S/m to 6.6 $\times 10^5$ S/m, and for dipping it was 2 $\times 10^5$ S/m to 5 $\times 10^5$ S/m. All eight drop-cast samples became conductive, while one of seven of the dipped samples failed. Notably, all samples were treated with relatively large volumes of acetic acid solution, which covered the traces and the neighboring substrate area. Careful control of acetic acid treatment locations was

not needed for PCL-based traces, contrary to Sui's work, where precision in acetic acid volume and location was important [63]. Compared to dipping, drop casting allowed for treating a greater number of samples simultaneously with lower total volumes of acetic acid solution at the lab scale.

Wet Time and Concentration: PCL

In order to systematically study the impact of acetic acid concentration and wet time on conductivity, a set of 45 folded dipole antennas were screen printed using 30:1:8 Zn:PCL:Anisole by weight ink on PET substrates. Test conductive traces were based on the design of a folded dipole antenna, discussed in more detail in chapter 4. It was a single line 1 mm wide and 320 mm long, which can equally be understood as two 160-mm segments or 5 lines of about 40 mm each. Once the prints were dry, profilometry data and microscope images were collected from a representative sub-section of the samples. Figure 2.14b shows 12 of the printed samples. Figure 2.14c shows a micrograph of a corner of one sample with smooth edges and a solid print. Figure 2.14d shows profile data from four corners of on sample, with average thickness of around 35 µm. The prints were randomly assigned to one of three acid concentrations: 9%, 25%, or 50% acetic acid by volume in DI water. Each concentration was further subdivided into five wet times: 1, 5, 9, 13, and 17 minutes. The samples were laid flat in a tray and a 1-mL syringe was used to deposit about 1 mL of acid solution onto each antenna. The samples were monitored to ensure all printed areas remained covered by solution, and additional solution was added if any areas became exposed. At the end of the allotted time, samples were transferred to a 50°C oven and baked for 15 minutes.

A digital multimeter was used to measure resistance first of the full 320-square trace, then each of the sub-components. For each treatment condition, two principle figures of merit are reported: conductivity and yield. To calculate conductivity, the number of squares was used to first calculate sheet resistance, (R_s) using $R_s = R\frac{L}{w}$, where R is the measured DC resistance, L the length of the trace and w the width. Conductivity (σ), was found using $\sigma = \frac{1}{R_s \times th}$ where th is the average thickness measured by the profilometer. The yield was defined as the percentage of linear segments (each sample contained 5 such segments) that had finite resistance. The yield was an important parameter when interpreting results, because conditions that led to high conductivity but low yield were unpredictable, uncontrolled, and ultimately undesirable. Figure 2.15 shows the yield and conductivity as a function of acid concentration and wet time.

For the highest concentration treatment (50%), increasing wet time increased conductivity considerably. All samples treated for 5 minutes or longer had finite re-

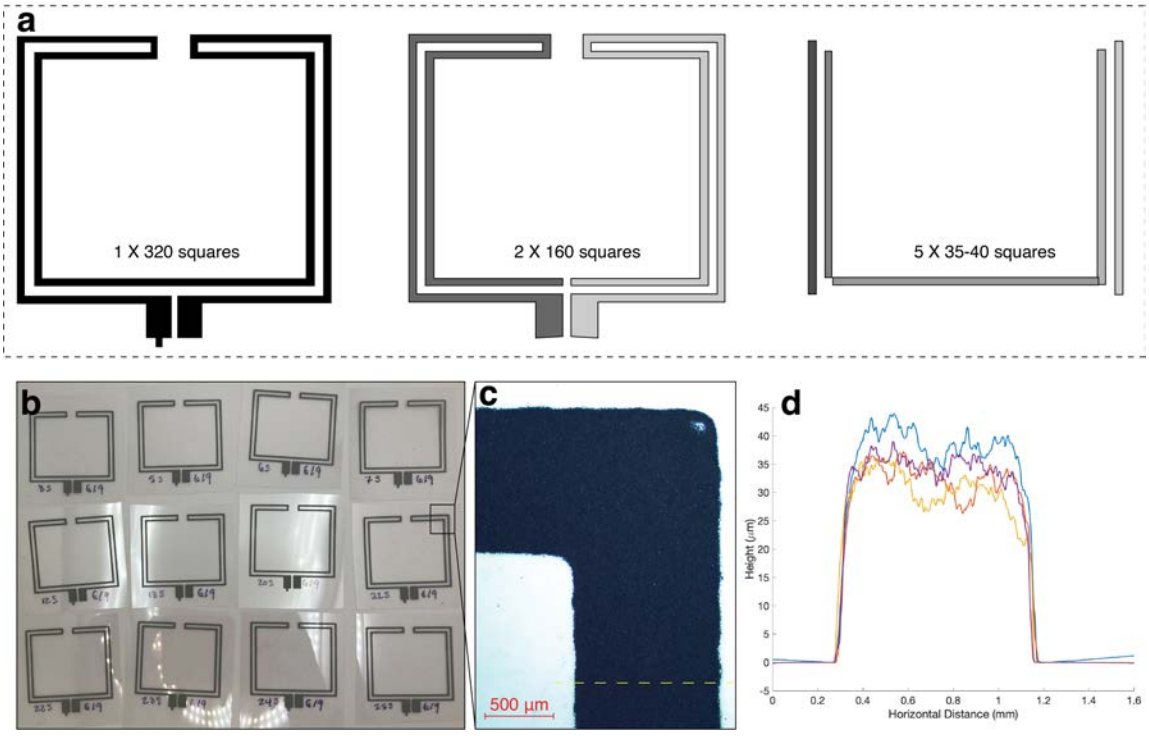

Figure 2.14: a) Traces used for conductivity tests can be seen as a single line of 320 squares, two lines of 160 squares, or five lines of 34, 34, 40, 41, and 41 squares each. b) A dozen printed zinc antennas on PET substrates. c) Microscope image showing the corner of one printed 30:1:8 Zn:PCL:Anisole trace on PET. d) Profiles of four corners of one antenna showing average thickness of 35 µm.

sistance, only about two-thirds of the segments in the 1-minute group did. Increasing wet time from 5 to 17 minutes resulted in more than tripling of the conductivity, with longer wet times consistently leading to higher conductivity.

The the 25% acid concentration group experienced different trends. For this concentration, the highest yield was for the 1 minute wet time, the lowest yield at 5 minutes, with yield increasing as a function of wet time up to 13 minutes. Conductivity follows a similar trend: notably high conductivity for the 1 minute wet time, then moderate conductivity increasing as a function of time between 5 and 13 minutes. The 17 minute treatment in both the 25% and 9% concentrations had markedly lower yield and conductivity than shorter time treatments. This suggests that 17 minutes is too long, and the printed trace is beginning to break down. That

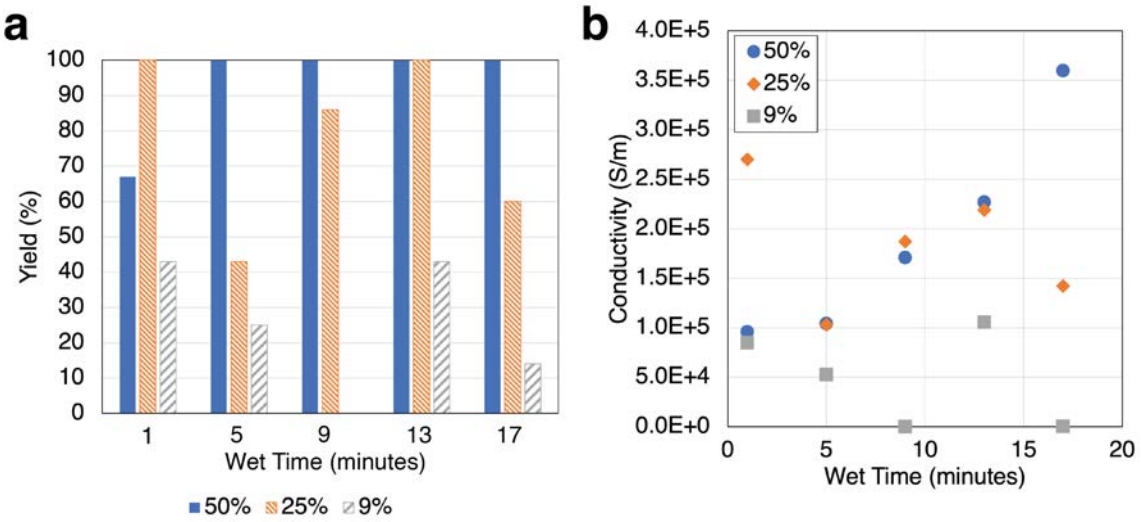

Figure 2.15: a) Yield of printed 30:1:8 Zn:PCL:Anisole traces on PET as a function of acid treatment time and acetic acid concentration in water. Higher concentration generally improves yield. For low and moderate acid concentration, increased treatment time improves yield somewhat. b) Average conductivity of 10-15 printed segments as a function of acid treatment time and acetic acid concentration. At the high concentration, a increasing treatment time increases conductivity. At low and moderate concentration, conductivity has no clear relationship with time. All traces were dried in an oven at 50°C for 15 minutes.

this trend is not seen in the 50% acetic acid group might suggest that long exposure to water leads to water absorption and polymer swelling, which disconnected the networks.

The 9% acetic acid group had consistently lower yield and lower conductivity than either of the higher concentration groups. We did not see strong relationships between wet time and yield of conductivity for this group. Lee et al. used 9% acetic acid in water and about one minute treatment time, and stated that "the effect of exposure time is minimal since the removal of the surface oxide layer and the particle welding are completed in a short time," [50]. Our results suggest Lee's explanation is incomplete.

In general, increasing wet time increased conductivity to a point. Once the binder swelled or began to dissolve, conductivity decreased again. Different binders were able to withstand different wet times, and those which could tolerate longer wet times before swelling were able to produce traces with higher conductivity. PCL traces

had higher conductivity because of the longer treatment times available with this hydrophobic and slow-degrading binder. Additionally, careful control of all process variables is important because the treatment is highly sensitive to local variations in conditions.

2.5 Drying Conditions

The drying process had a significant impact on the conductivity of acetic acid-treated zinc traces. Samples could be dried at room temperature by leaving them in ambient conditions, which took about 15-20 minutes depending on airflow, or with an air- or nitrogen-gun, which took about 2-5 minutes, again depending on the velocity of the gun's air-stream and the distance between the gun and the sample. Changes in drying speed effectively altered the trace's wet time, which changed the conductivity. Hand-crafted drying methods were difficult to reproduce exactly, which led to high sample-to-sample variation of conductivity.

Samples could alternatively be dried with exposure to heat: with a heat gun, on a hot plate, or in an oven. Time of exposure to heat and temperature are independent variables for any of these methods.

The chemical reactions that lead to conductive traces do not require elevated temperature in theory–indeed, traces with PVP binder in Lee, Sui, and this work were found to be conductive when dried at room temperature. However, traces dried at elevated temperature had higher conductivity. Traces using a PCL binder required heat.

Drying Temperature for PCL

To study the impact of drying conditions, the 320-mm long folded traces illustrated in figure 2.14a were printed with 30:1:8 Zn:PCL:Anisole ink on PET substrates. They were treated with 50% acetic acid solution for 13 minutes, then dried on a hotplate for 15 minutes. The temperature of the hotplate was varied from batch to batch. Additionally, due to spacial variations in heat across the surface of the hotplate, individual samples experienced different local temperatures. The actual temperature of each sample was recorded using an IR thermometer. Data was recorded for each full 320-mm trace as well as each 160-mm half-trace. Yield and conductivity were calculated using the method described in the concentration and wet time experiment. Figure 2.16 shows the yield and conductivity as a function of drying temperature.

Samples dried at less than 45°C or more than 55°C usually were nonconductive. The high temperature limit is likely set by the melting point of the binder: in this

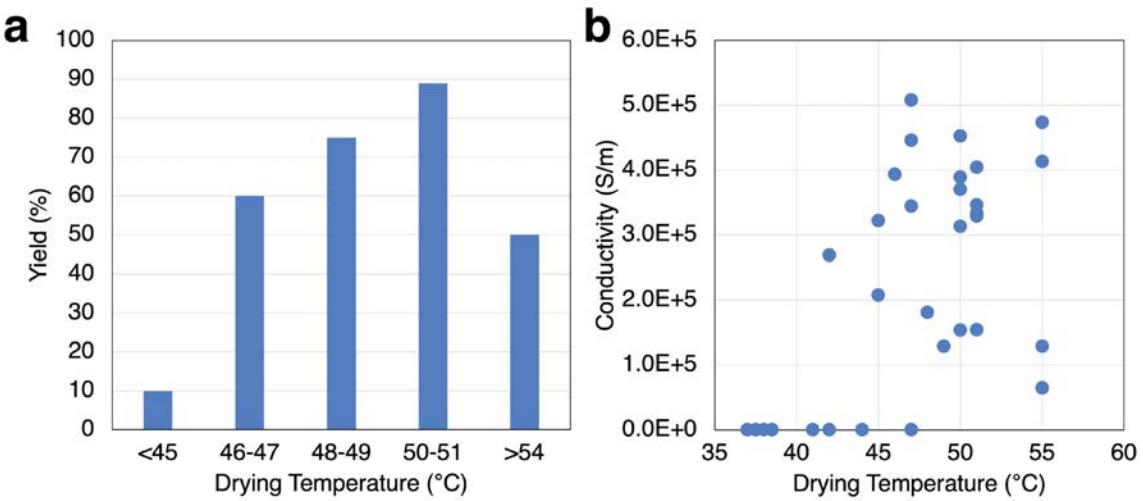

Figure 2.16: a) Yield as a function of drying temperature for 31 printed 30:1:8 Zn:PCL:Anisole traces on PET which were treated with 50% acetic acid solution for 13 minutes. Each bin includes n=4 to n=20 samples. These samples were dried on a hotplate with local heat variation and individual samples' temperatures were measured. b) Conductivity of the traces shown in (a) as a function of drying temperature. Temperatures below 45°C or above 55°C produce mainly non-conductive traces. Within the optimal temperature window, there is not a clear relationship between temperature and conductivity.

case PCL melts at about 60°C . Majee et al used a PVB binder with a melting point of 90-120°C and found that for their traces, conductivity remained high up to 90°C [71]. When the binder melts, the zinc particles can move around, which prevents stable conductive networks from forming or disrupts connections made during the acid treatment process.

For high acid concentration and a PCL binder, exposure to at least 45°C after acid treatment is required; traces were never conducive when dried at less than 40 °C . This is different from PVP-traces, which had some conductivity after room-temperature drying, though heating to 45°C was found to be helpful for improving conductivity.

2.6 Stability

High humidity is known to degrade conductivity of printed zinc traces because the water vapor in the air accelerates zinc oxide and hydroxide growth [51]. Printed zinc traces for use as antennas and connectors in agricultural sensors will need to survive exposure to high heat and humidity in the field over a period of months. They will rely on encapsulation layers to prolong their functional lifetime.

The prior works on chemically treated zinc traces all reported some lifetime metrics. Lee et al., working with a PVP binder, reported physical degradation after 3 days immersed in water. Loss of electrical conductivity happens prior to physical degradation. Sui et al. also used a PVP binder and reported an exponential increase in resistance of unencapsulated printed traces over time, with resistance increasing by an order of magnitude after 6 days in air. Traces encapsulated with wax were reported to maintain their conductivity for 30-35 days in air. Majee et al., using a PVB binder, reported some conductivity over 250 days, with a significant loss of conductivity after 40 days, when humidity in their lab increased.

PVP Stability

We found different results for Zn-PVP trace lifetimes than Sui et al. Unencapsulated traces lost conductivity within one day, and beeswax encapsulated samples' conductance decreased by an order of magnitude after 3-9 days.Figure 2.17 shows the conductivity over time of PVP traces and PCL traces for two weeks, normalized by the initial conductivity of each trace. These different results may be due to the difference in humidity between our lab and Sui's, as ours was likely more humid.

PCL Stability

To characterize the lifetime of printed zinc traces with PCL binder, the impact of humidity, and the effectiveness of beeswax as an encapsulation layer, four treatment conditions were set up. First, traces were divided into two groups; one group was kept in an environmental chamber at 19°C and 10% RH, while the other was kept in the uncontrolled lab environment, at about 26°C and 30-40% RH. With each location, some traces were not encapsulated, and some were dip-coated in beeswax. The resistance of the full 320-mm trace was recorded every minute using a 2-point technique by a multichannel Data Acquisition System (Keysight DAQ970A).

Figure 2.18 shows the loss of conductivity over a period of 60 days for samples with and without wax encapsulation layers under low and high humidity conditions. Because the samples at high humidity experienced changing environmental condi-

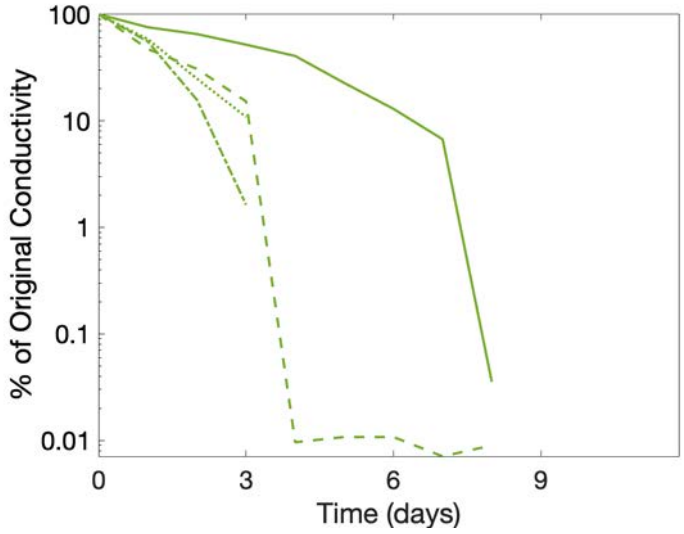

Figure 2.17: PVP-based traces, even when encapsulated with beeswax, lost their conductivity completely within 3-7 days or less.

tions, the actual measured humidity data is included on the right axis of the top plot. Generally, samples kept at low temperature and low humidity retained their conductivity to a greater degree than the samples subject to higher temperature and humidity. This is expected, given the known impact of humidity on loss of conductivity. Of those samples which were exposed to high temperature and humidity, those which were not encapsulated lost their conductivity more rapidly and to a greater extent than those which were encapsulated, demonstrating the effectiveness of the wax encapsulant. By days 25-30, the encapsulated samples in high-humidity environments had experienced the same proportional loss of conductivity as the encapsulated sample in the low-humidity environment. Moreover, periods of high humidity, for example on days 3-4, correspond to marked drops in conductivity for those samples which were not encapsulated.

For applications in agriculture, conductivity lifetimes should match a growing season—60-100 days—which PVP-based inks do not provide, even with encapsulation. PCL was capable of producing traces with lifetimes suitable for agricultural applications, provided that they are encapsulated to maintain conductivity in humid environments.

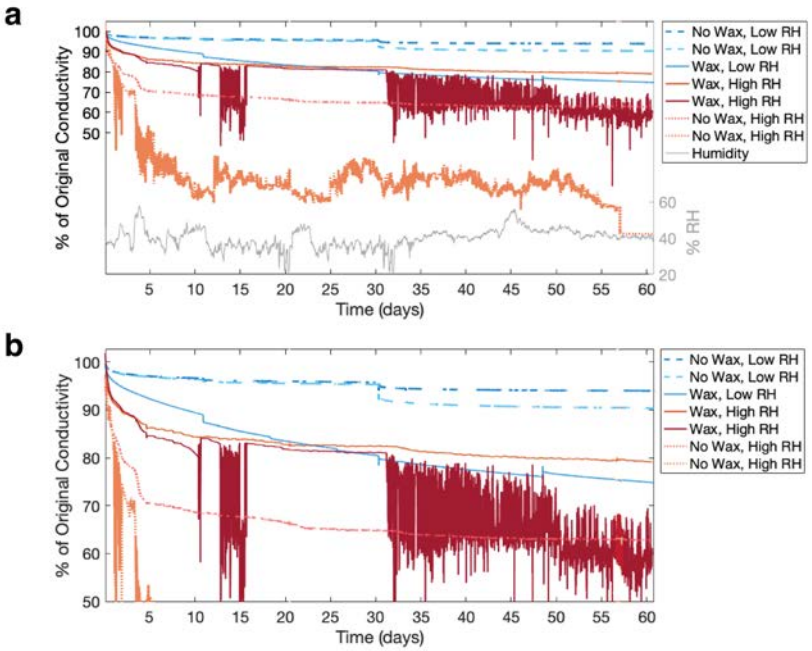

Figure 2.18: Zn-PCL traces relative conductivity over time. Samples exposed to high humidity lost their conductivity faster than those in controlled-humidity environments. Beeswax encapsulation helped samples in the high-humidity environment maintain their conductivity longer than unencapsulated samples in the same environment. a) Periods of high relative humidity (data show on the right axis) corresponded to loss-of-conductivity in unencapsulated samples. b) Zooming in on the y-axis to more clearly see small changes in conductivity.

2.7 Conclusions and Future Work

Printed biodegradable electronics are a complex set of interrelated optimization challenges, where changing one process can necessitate re-optimization of another process. Working with biodegradable materials introduces a set of trade-offs between lifetime, functionality, and degree of degradation: materials that work well for a long time degrade slowly. Because natural materials have inherent variability, precise control of all processing steps is important to limit variation in the final products.

Highly conductive, biodegradable zinc ink is a viable material for wireless agricultural sensor nodes. Wooden substrates treated with wax can be used as printing substrates. The next step is to re-optimize zinc parameters for processing on wooden

substrates.

Interfacing between printed zinc and commercial ICs, or printed zinc and other printed materials is another area for future work. Finally, the complete fabrication process of the integrated sensor node will need to be streamlined.

Chapter 3

Nitrate Sensors

As discussed in section 1.2, nitrate is a key component of fertilizer, necessary for plant growth, and, when applied in excess, it causes harm to both people and the environment. Current techniques for measuring nitrate in water and soil are complex, expensive, and labor intensive, so are limited in the breadth of coverage and frequency of measurement.

Environmental quality monitoring and precision agriculture require nitrate sensors that are sensitive, selective, mass-producible, easy-to-read, involve few or no moving parts, and are robust enough to survive field deployment and soil insertion. Printed solid-state potentiometric ion-selective electrodes have the potential to meet these criteria. Potentiometric ion-selective electrodes output a voltage that corresponds to the concentration of ion present in a solution. They have been well-studied and used in both medical and environmental applications. The use of printing methods for sensor fabrication offers several advantages, such as low cost, high throughput, and ease of fabrication.

This chapter describes the operation and fabrication of gold- and carbon-based ion selective electrodes, the optimization of a stable reference electrode, and characterization of fully printed nitrate sensors in aqueous solution and soil media. Portions of this chapter were previously published as "Printed Potentiometric Nitrate Sensors for Use in Soil" [72].

3.1 Introduction

Potentiometric sensors are composed of two electrodes: an ion-selective electrode (ISE) and a reference electrode (RE). The signal output is the potential difference between the two electrodes at zero-current conditions. Conventionally, these elec-

trodes are glass tubes filled with salt solutions and containting a wire, often made of silver/silver-chloride, as shown in Figure 3.1a. Solid state potentiometirc sensors, including the printed sensors described here, replace the liquid phases with solid polymer films, as illustrated in Figure 3.1c. In both cases, the ISE has a polymer membrane doped with an ionophore—a chemical designed to selectively and reversibly bind to the ion of interest [73, 74, 75, 76, 77, 78, 79, 80, 81]. As the concentration of the ion of interest, NO_3^- in this case, in the sample solution increases, the potential that develops at the boundary between the ion-selective membrane and the sample increases. The origin of the boundary potential is the separation of cations into one side of the boundary and anions to the other at the very narrow (a few nm) width of the boundary. In bulk solutions and membrane volumes, electroneutrality dictates equal concentrations of positive and negative charges, but right at the boundary, the different Gibbs free energy of partition for an ion in a solvent creates the thin space-charge layer. The potential developed here depends on the concentration of ion in aqueous solution only if the concentration of ion in the membrane is kept constant. The ionophore binding sites, together with an oppositely charged ion bound in the membrane, buffer the ion concentration in the membrane. More details of this process can be found in Buhlmann and Chen's review [82]. The result is that the potential at the ISE is described by the Nernst equation:

$$E = E_0 + 2.3026\frac{RT}{zF}log_{10}(a_{ion}) \tag{3.1}$$

where E is the potential measured across the electrodes, E_0 is the cell potential, R is the ideal gas constant, T is the temperature, F is Faraday's constant, z is the charge of the ion of interest, and a_{ion} is the ion activity. The ion activity is a function of the concentration of the ion in solution and the activity coefficient, which is 1 for sufficiently dilute solutions. Thus, an ideal potentiometric sensor for a monovalent anion, such as NO_3^-, at room temperature is expected to exhibit a -59.1 mV change for every factor of ten increase in NO_3^- concentration. The potential difference measured between the ISE and RE is the sum of the potentials developed at each metal–metal, metal–solid, and solid–liquid boundary, as illustrated in figure 3.1b,d. Ideally, only the ion-selective membrane–sample boundary potential depends on the nitrate concentration; the other boundary potentials are accounted for by E_0 in the Nernst equation. Because measurements are taken at very low current conditions, there are no ohmic drops within single phases; only the boundary potentials contribute to the overall measured potential.

REs are typically made of silver/silver-chloride (Ag/AgCl) and maintain a constant potential in varying ionic environments [83]. Commercially available reference electrodes are glass tubes described above and illustrated in figure 3.1a. Most po-

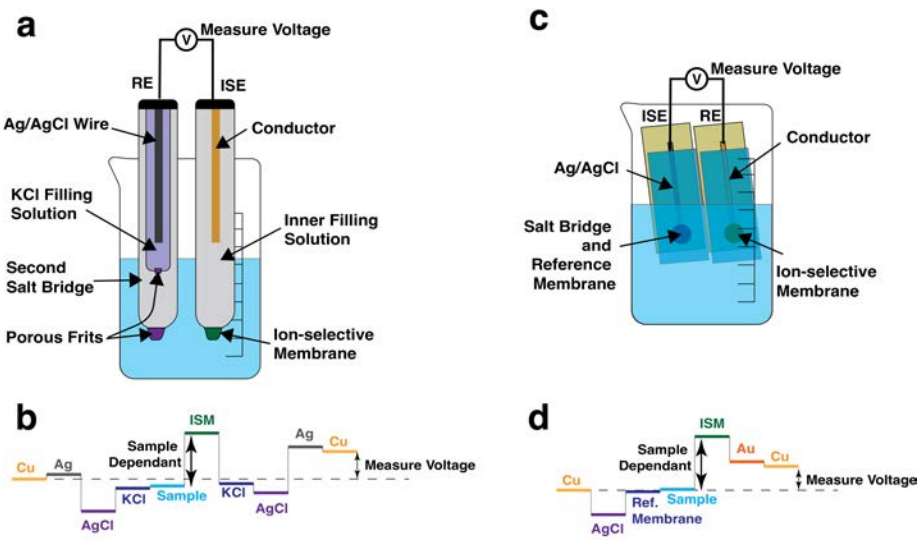

Figure 3.1: a) Conventional potentiometric ion sensors are made of two liquid-filled glass electrodes. The reference electrode has a silver wire coated in silver chloride suspended in a concentrated chloride solution. Porous frits provide electrochemical contact with the test solution while keeping the inner filling solution inside. Two junctions improve isolation of the electrode to increase stability. The ion selective electrode has a conductor which can also be silver/silver-chloride in a filling solution. The end of the glass tube is capped by an ion-selective membrane. b) The potential difference measured between the two electrodes is the sum of the potentials developed at each boundary. c) Solid state potentiometric sensors replace the glass and liquid parts of conventional electrodes with polymer membranes and solid films. d) The potential between the electrodes is again the sum of the potentials developed at each interface.

tentiometric sensor studies that present solid-state ISEs rely on such liquid-based reference electrodes. Solid-state reference electrodes are more suitable for field deployment because they have the neither the liquid filling nor the fragile glass tube, but solid-state references are typically less stable than commercial references. Significant challenges remain in the development of solid-state reference electrodes, yet relatively few studies characterize printed references with the same rigor as ISEs [84].

Because soil is a complex environment containing many ions that could interfere with a nitrate sensor, selectivity is particularly important for sensors intended for use in soil [85]. Selectivity studies for anion ISEs such as nitrate typically focus on ions from the Hoffmeister series, which are most likely to interfere. While these characterizations are important, soil can contain high concentrations of other ions, so both the ISE and RE must be characterized for sensitivity to ions found in soil. ISEs obtain their selectivity from specially designed synthetic ionophores, although even these have nonidealities. Ions present in the environment can also interfere with ion binding sites or charge transport materials in the membrane, hindering the functionality of the ISE.

Table 3.1 compares potentiometric nitrate-selective electrode measurements from the literature. Several works use scalable fabrication techniques such as screen or stencil printing to fabricate electrodes and drop-cast membranes similar to this work. Three of these use commercial references and demonstrate measurements in liquid samples. Three more use solid-state references and show applications in soil or soil slurries; however, only one work characterizes the reference electrode's stability, and none report stability in varying nitrate concentrations or the impact of interfering ions. Another group of works explore transducing layer materials for improved stability. These works are based on glassy carbon electrodes, do not use printing techniques, and most do not demonstrate performance in real-world conditions.

Table 3.1: Comparison of sensitivity, selectivity, and reference electrodes for nitrate-selective potentiometric sensors.

Fabrication Technique	**ISE Materials**	**Sensitivity (mV/dec)**	**Selectivity Ions**	**Reference Electrode Materials**	**Reference Electrode Characterization**	**Application**	**Reference**
Screen print, Drop cast	AgCl,gel	−54	$H_2PO_4^-$, SO_4^{2-}, NO_2^-, CO_2^-	Commercial		Soil extraction	[79]
Screen print	PTFE membrane	−57.2	$H_2PO_4^-$, SO_4^{2-},Cl^-	Not specified		Wastewater	[86]
Drawing,Drop cast	Pencil Graphite	−49.4	SO_4^{2-}, Cl^-, NO_2^-, OH^-	Commercial		Soil extraction	[87]
Stencil print	Silver	−57	$H_2PO_4^-$, SO_4^{2-},Cl^-	Ag/AgCl		Soil slurry,Pulses in soil	[88]
Laser, Drop cast	LIG	−54.8		Ag/AgCl paint		Soil slurry,Pulses in soil	[89]
Evaporation, Dispenser robot	Gold/POT-MOS_2	−64	PO_4^{3-}, SO_4^{2-}, Cl^-,NO_2^-, HCO_3^-	Screen printed Ag/AgCl with Nafion	versus Cl^-	Soil Slurry, Pulses in soil	[90]
	Glassy carbon, Graphene	−57.9	SO_4^{2-}, Cl^-	Commercial		Drinking water	[91]
Electrodeposition	Au-NP and PPy on glassy carbon	−50.4	PO_4^{3-}, SO_4^{2-}, Cl^-, Br^-	Commercial			[92]
Electrodeposition	Au-NP, PPy, graphene oxide	−50	$H_2PO_4^-$, SO_4^{2-}, CH_3COO, HCO_3	Commercial		Soil Percolate	[93]
Drop cast	Graphene/TTF on glassy carbon	−59.1		Commercial			[94]
	CNT/ionic liquid on glassy carbon	−52.3 to −57.1	$H_2PO_4^-$, SO_4^{2-}, Cl^-, NO_2^-, CO_3^-, CH_3COO, F^-, Br^-	Commercial			[95]
Electrodeposition	PPy on wire	−54.1		Commercial		Pulses in	[96]
Inkjet and screen print	Gold	−54.1	PO_4^{3-}, SO_4^{2-}, Cl^-,NO_2^-, NH_4^+, K^+, Mg^{2+}, Ca^{2+}	Screen printed Ag/AgCl with CNT and $NaCl/NaNO_3$	versus NO_3^-, other ion interference	Field soil sensitivity	This Work [72]

In this work, we characterized the intermediate steps between nitrate ISE demonstration in aqueous solution and the deployment of a fully printed sensor in the field. ISEs were printed with both non-biodegradable materials (gold on PEN) and biodegradable materials (carbon on Bristol paper). The sensitivity of both types of ISEs was measured against commercially available REs and demonstrated a near-Nernstian response to nitrate. Carbon-based ISEs were more stable than gold ISEs as carbon acted as both a capacitive transducer layer an a conductor. Printed REs were optimized for stability across a range of nitrate concentrations. Both ISEs and REs were independently tested in solutions containing eight potentially interfering ions, which were chosen for their prevalence in soil. Calcium had the most significant impact on both ISEs and REs. The printed nitrate ISEs were paired with printed REs to create fully printed nitrate sensors, which were slightly less sensitive to nitrate in aqueous solutions than printed ISEs paired with glass references. Fully printed nitrate sensors were measured in a high-organic-matter field soil, and demonstrated sensitivity equal to their sensitivity in solution.

3.2 Fabrication

Ion-Selective Electrode Fabrication

ISEs were fabricated according to the process illustrated in Figure 3.2a. Gold electrodes, which were 3.5-mm-diameter circles connected to a 1-mm-wide trace, were printed on 25-µm-thick PQA2 PEN using Harima Nanopaste(Au) NPG-J gold ink in a Dimatix DMP-2850 inkjet printer (Fujifilm Dimatix, Santa Clara, CA, USA) using a 10 pL cartridge and no platten heating. Printed gold electrodes were sintered at 250 °C for 50 min and then encapsulated with 75-µm-thick laser-cut Teflon tape with circular windows of 5 mm diameter for the active area. The window in the encapsulant was larger than the electrode to allow space for the membrane to seal to the substrate, preventing bubbles or delamination of the membrane. ISE membranes were fabricated by mixing 5.2 wt% nitrate ionophore VI, 47.1 wt% dibutyl phthalate, 0.6 wt% tetaroctylammonium chloride, and 47.1 wt% PVC. A total of 0.2 g of this mixture was dissolved in 1.3 mL of tetrahydrofuran (THF). Sixteen µL of the membrane solution was drop-cast on the printed gold electrode surface. The resulting ISE was dried in a fume hood for 15 min.

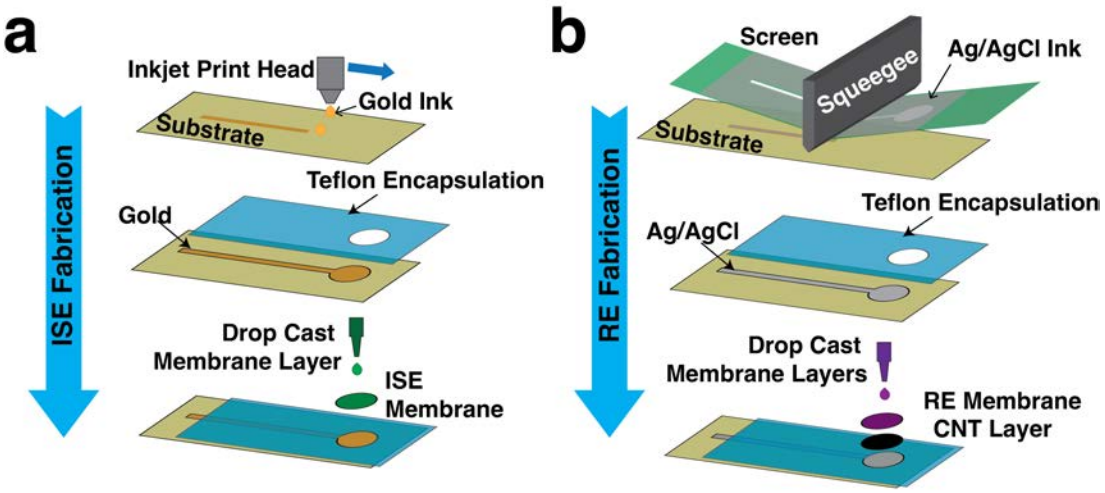

Figure 3.2: a) Ion-selective electrodes were made by inkjet printing gold onto a substrate, and encapsulating the trace with a teflon tape. The membrane solution was drop-cast onto the exposed area of the electrode. b) Reference electrodes were made by screen printing Ag/AgCl ink onto the substrate, and the trace was encapsulated with teflon. The carbon nanotube transducing layer was drop-cast first, followed by the PVB/salt membrane.

Reference Electrode Fabrication

Printed RE fabrication is outlined in Figure 3.2b. Ag/AgCl electrodes with the same geometry as the gold electrodes were screen-printed on 100-µm-thick PET using Engineered Materials Systems, Inc. CI-4001 ink (Delaware, OH, USA). Three layers of ink were printed; each layer was dried before the next was printed. Printed Ag/AgCl electrodes were then annealed at 120 °C in a vacuum oven for 2 hours and encapsulated with laser-cut Teflon tape 75 µm thick.

The REs employed a CNT transducer between the Ag/AgCl electrode and the membrane. This transducer was composed of 0.01 g of CNT (iP-Single-Walled Carbon Nanotubes from Carbon Solutions, Inc., Riverside, CA, USA) and 0.05 g of F127 (poly(ethylene glycol)-block-poly(propylene glycol)-block-poly(ethylene glycol) diacrylate) dissolved in 10 mL of THF, which were sonified for 1 hour in an ice bath using a Branson Digital Sonifier probe. The resulting mixture was deposited on the printed REs' surface as 4 µL total in two separate 2 µL increments. The RE membrane was made by dissolving 1.58 g of Butvar B-98 (poly(vinyl butyral) (PVB), 1.00

g of NaCl, and 1.00 g of $NaNO_3$ in 20 mL of methanol. This mixture was sonified for 30 min in an ice bath. The resulting solution was deposited on top of the CNT transducer as 6 µL total in three separate 2 µL increments. Unless otherwise noted, all chemicals used in both ISE and RE membranes were obtained from Millipore Sigma (St. Louis, MO, USA).

Fully printed nondegradable sensors used in soil studies were attached to an acrylic block for mechanical stability. Silver conductive epoxy 8331D (MG Chemicals, Burlington, ON, Canada) was used to connect wires, and the joint was encapsulated by Gorilla epoxy.

3.3 Nitrate-Selective Electrode Sensitivity

The sensitivity of printed gold ISEs was measured against commercial glass reference electrodes in aqueous solutions, as illustrated in Figure 3.3a. Commercial Ag/AgCl electrodes with liquid filling solution were obtained from Millipore Sigma (Z113107). To perform the measurements, $NaNO_3$ was dissolved in deionized water, and diluted to 0.05, 0.1, 0.2, 0.5, 1, 2, 5, 10, 20, 50, and 100 mM concentrations. Prior to measurement, the electrodes were conditioned for at least two hours in 100 mM $NaNO_3$. Chronopotentiometery was performed using the Keithley 2400 Series SourceMeter, Keysight B2987A Electrometer/High Resistance Meter, and Ivium-n-Stat from Ivium Technologies B.V. (Eindhoven, The Netherlands).

Figure 3.3b shows the potential over time for one ISE measured against a glass commercial reference electrode in nitrate solutions between 20 mM and 0.05 mM. This ISE reported a stable potential value less than 30 s after a change in concentration. The data from Figure 3.3b can alternatively be plotted versus nitrate concentration on a log scale, as shown by the blue circles in Figure 3.3c. The other lines in Figure 3.3c represent sensitivity for six additional ISEs in three batches. The average sensitivity for all seven sensors was -54.1 ± 2.1 mV/dec.

The linear region for these sensors was between 0.05 mM and 100 mM. This range is equivalent to 3.1 to 6200 ppm NO_3^- or 0.7 to 1400 ppm nitrogen (NO_3^--N). Concentrations of nitrate in agricultural fertilizer vary widely depending on crop and soil type as well as fertigation technique, but a few 100 ppm would be a high nitrate concentration in fertilizer [97] . In the United States, the Environmental Protection Agency's drinking water quality standards specify a maximum of 10 ppm NO_3^-, and some studies have shown an increased risk of certain health conditions for water with 5 ppm NO_3^- or greater. The sensors presented here covered nitrate concentrations from drinking water to concentrated fertilizer.

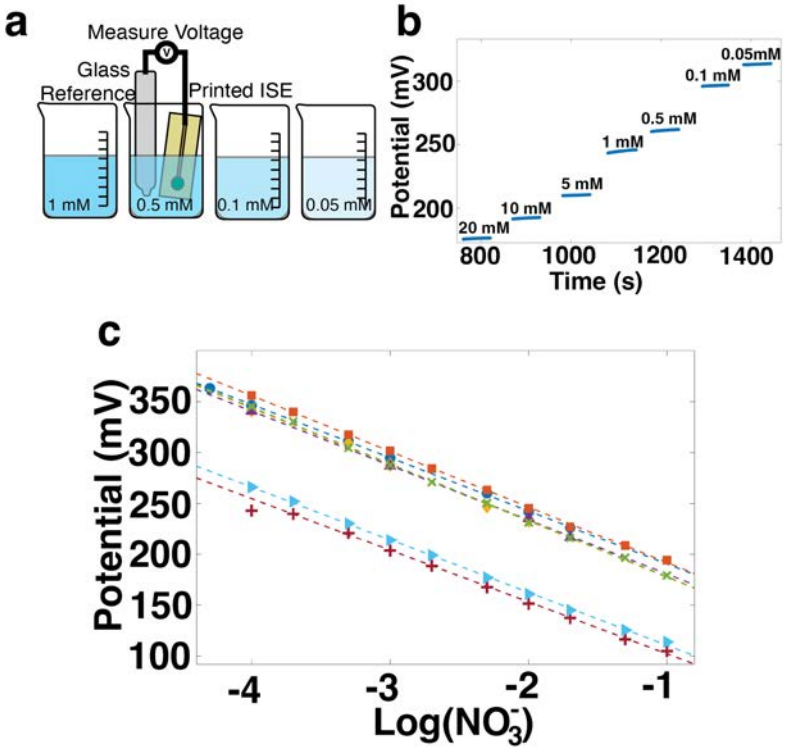

Figure 3.3: a) Characterization of a printed nitrate-selective electrode against a commercial reference electrode in $NaNO_3$ solutions of varying concentrations. b) Potential over time response of a printed nitrate-selective electrode in changing concentrations of nitrate. c) Sensitivity plot of 7 nitrate-selective electrodes overlaid, showing good repeatability and near-Nernstian response of -54.1 ± 2.1 mV/dec.

In Figure 3.3c, the sensitivity curves for different sensors are offset one from another. This variation in E_0 is common in ISEs and means that each sensor must be individually calibrated prior to use. E_0 variation has a variety of causes, many of which are summarized by Hu et al. [98]. Properly, E_0 is the potential at ion activity of 1, which is outside of the linear range of the sensors. E_0 values presented here were calculated using the potential at 1 mM NO_3^- concentration. Within one batch of ISEs, the E_0 variation was found to be 12.5 mV. The measurements for one batch were done with each ISE paired with one of several different commercial reference electrodes. While nominally identical, the commercial reference electrodes' potentials were up to 11 mV different from each other. This difference in commercial

references' performance was consistent with E_0 values obtained within a batch of ISEs. The batch to batch variation was 83 mV over six batches. This significant variation may be due to variation in the membrane drying and sections of crystallized PVC in the membranes, as suggested by Rousseau et al. [99].

3.4 Reference Electrode Development

Reference electrodes act as electrochemical ground; therefore, their potential must remain unchanged in varying ionic environments. The precise composition of the printed RE will impact E_0 in the Nernst equation. However, because E_0 is constant, the offset is easily accounted for in calibration.

The performance of printed REs was determined by measuring them versus a commercial Ag/AgCl double junction RE, as in Zamarayeva [100] and illustrated in Figure 3.4a. First, pristine printed Ag/AgCl electrodes were measured, and the resulting data are shown in Figure 3.4b. The output voltage was unstable since these printed REs lacked a source of chloride ions, which are needed for the Ag/AgCl reversible reaction:

$$\mathrm{AgCl} + \mathrm{e}^- \rightleftharpoons \mathrm{Ag} + \mathrm{Cl}^- \tag{3.2}$$

The surface area and composition of the printed RE were modified by adding a CNT layer and a PVB-NaCl membrane was added to provide a source of chloride. The characterization is shown in Figure 3.4c. These electrodes used the formulation developed in Zamarayeva [100] for use in chloride-rich environments. REs with an NaCl membrane showed a -18 mV/dec sensitivity to nitrate, which is unacceptably high.

The optimized RE composition was achieved with the addition of $NaNO_3$ to the PVB-NaCl membrane. Cattrall and Zamarayeva et al. [101, 100] have shown that including the ion of interest in the membrane of an RE reduces its sensitivity to that ion. To reduce sensitivity to nitrate, $NaNO_3$ was added to the membrane; sensitivity data for this electrode are shown in Figure 3.4d. This formulation had a sensitivity of -3 mV/dec, which was a marked improvement over the NaCl membrane alone.

The effect of adding the ion of interest to the reference electrode membrane is highlighted in Figure 3.4e, where the NaCl membrane and NaCl+$NaNO_3$ membranes are directly compared. In this figure, potentials are normalized by subtracting the average potential in 1 mM nitrate from the average potential at each concentration, and the potential offsets are plotted versus nitrate concentration. The RE whose membrane included NaCl + $NaNO_3$ had a flatter slope, which reflects its insensitivity to nitrate concentration.

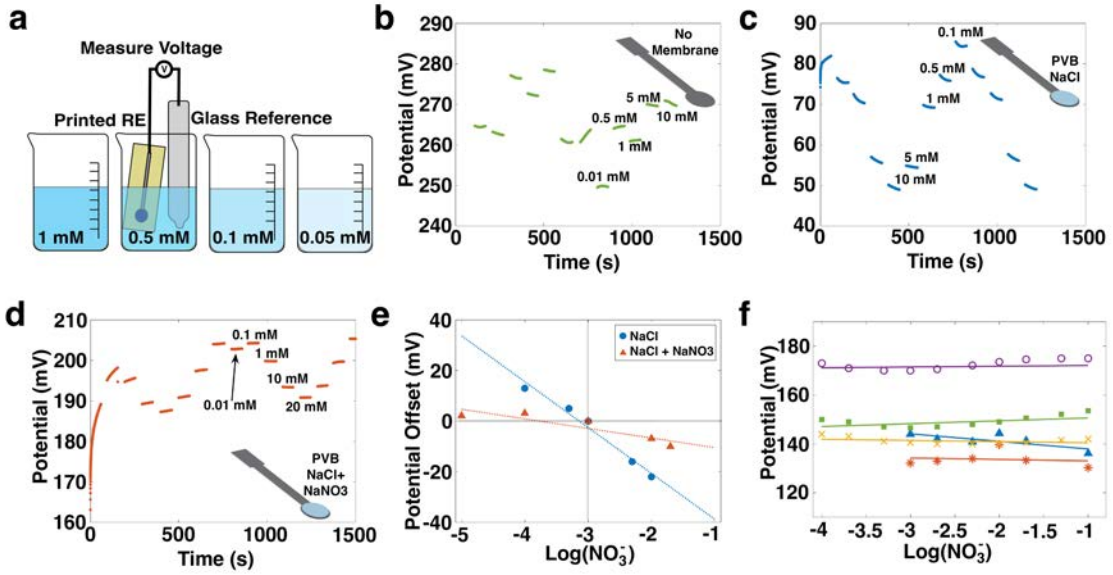

Figure 3.4: a) Measuring a printed reference electrode against a commercial reference electrode in $NaNO_3$ solutions of varying concentrations. Potential over time in changing concentrations of nitrate of a printed Ag/AgCl reference electrode with b) no added membrane, c) PVB membrane with NaCl added, and d) PVB membrane with NaCl and $NaNO_3$ added. Measurements in (b-d) were done against a commercial Ag/AgCl reference electrode. e) Sensitivity of printed reference electrodes with NaCl in PVB membrane (blue), and $NaNO_3$ and NaCl in PVB membrane (red). The absolute value of the voltage measured at 1 mM $NaNO_3$ has been set to 0 mV to facilitate comparison of slopes. f) Sensitivity of five printed reference electrodes to NO_3 is 2.96 $\pm$ 1.9 mV/dec.

Repeatability across different reference electrodes is shown in Figure 3.4f, where voltage versus concentration for five printed REs with the NaCl + $NaNO_3$ + PVB membranes is displayed. All the printed REs showed a stable potential response over three orders of magnitude change in the nitrate concentration.

3.5 Interference

Soil is a complex environment containing a host of ions other than NO_3^-. Ideally, NO_3^- ISEs should be insensitive to all ions other than NO_3^-, and REs should be stable

regardless of the concentration of any ion. Selectivity studies quantify the degree to which these behaviors are true and identify elements which could cause errors in the measurements.

The Nicolsky–Eisenman equation describes the potential, E, generated by a potentiometric sensor in the presence of interfering species [102].

$$E = E_0 + 2.3026\frac{RT}{zF}log_{10}(a_A + \sum_B K_{A,B}^{POT}(a_B)^{\frac{z_A}{z_B}}) \tag{3.3}$$

where a_B is the ion activity (or concentration for dilute solutions) of ion B, and z_B is the charge of ion B, and the other constants are the same as in the Nernst equation 3.1.

It assumes Nernstian behavior for all ions, and interfering species' responses are weighted by their respective Nicolsky–Eisenman coefficient, $K_{A,B}^{POT}$, where A is the primary ion (NO_3^-, in this case) and B is the interfering species. $K_{A,B}^{POT}$ should be less than 1, and the nearer to zero, the less sensitive the ISE is to that interfering species.

Based on a soil chemistry report from A & L Western Agricultural Laboratories, eight possibly interfering species were chosen: sulphate (SO_4^{2-}), chloride (Cl^-), phosphate (PO_4^{3-}), nitrite (NO_2^-), ammonium (NH_4^+), calcium (Ca^{2+}), potassium (K^+), and magnesium (Mg^{2+}). Higher concentrations of SO_4^{2-} and Cl^- were also tested because they rank above NO_3^- in the Hoffmeister series, so were of particular concern as interfering species. Solutions for selectivity experiments were made with powdered Na_2SO_4, $NaNO_2$, KCl, $MgCl_2$, $Ca(NO_3)_2$, NH_4Cl, Na_3PO_4, and NaCl obtained from Millipore Sigma. The concentrations of these chemicals are listed in Table 3.2.

The two-solution method, which is a mixed solution method, was used to determine the $K_{A,B}^{POT}$ values of the ISEs for the ions listed above [102]. Printed ISEs were paired with a commercial Ag/AgCl reference electrode. Then, measurements were recorded first in 1mM $NaNO_3$ and then interfering salt and 1 mM $NaNO_3$. Figure 3.5 shows the output potential for one nitrate ISE in blue. Between each exposure to an interfering species (shown in white), the sensor was measured in 1 mM $NaNO_3$ (shown in gray) to provide reference data for the next species. The insert of figure 3.5 shows how the potential difference, ΔE, for magnesium was found as the step change from 1 mM $NaNO_3$ to 1 mM $NaNO_3$ + 16.5 mM $MgCl_2$.

The ΔE was then used in Equation (3.4) to calculate $K_{A,B}^{POT}$.

$$K_{A,B}^{POT} = a_A(e^{\Delta E z_A F/(RT)} - 1)/(a_B)^{z_A/z_B} \tag{3.4}$$

We also measured the printed REs' response to interfering ions by measuring them against commercial glass electrodes, first in 1mM $NaNO_3$ and then interfering

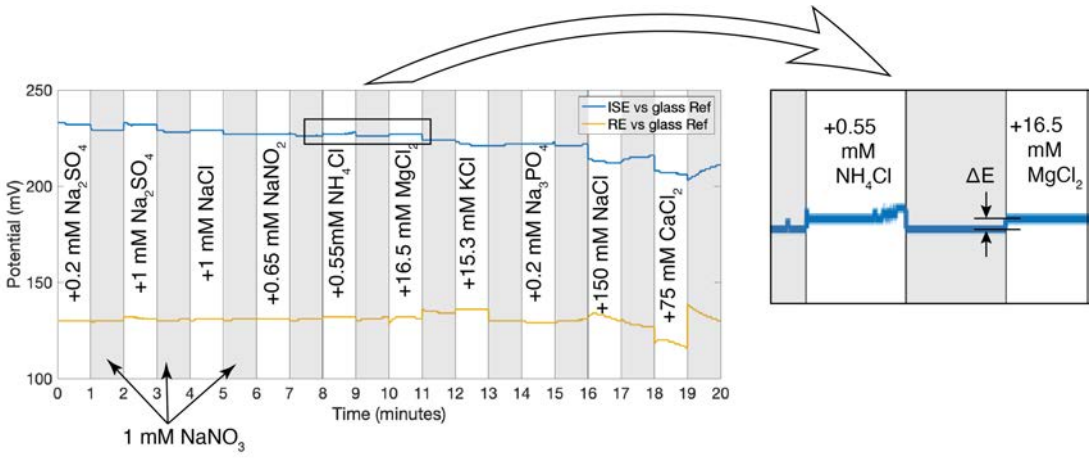

Figure 3.5: Potential over time of an ISE measured against a commercial reference electrode in solutions of various interfering ions (blue), and potential over time of a printed RE measured against a commercial reference (yellow). Both responses are stable with changing interference ions. (Inset) ΔE is the potential difference between measurement in 1 mM $NaNO_3$ and measurement in solution containing an interfering ion.

salt and 1 mM $NaNO_3$. The yellow line in figure 3.5 shows one RE's potential in the interfering solutions as an example. Because REs should not have Nernstian responses to ions, Equation (3.3) is not a good model for RE behavior. Instead, simple ΔE values are reported in Table 3.2. ISE $K_{A,B}^{POT}$ and RE ΔE values reported in the table are averages for N=4 electrodes.

As shown in Table 3.2, the $K_{A,B}^{POT}$ values for the ISEs and ΔE values for REs were quite small for most ions except Ca^{2+} at concentrations that are expected in soil. Ca^{2+}, however, had a significant impact on both the ISE and the RE, indicating that in soils with high concentrations of calcium, the sensor might be unreliable, or at least require site-specific calibration.

In addition to being insensitive to interfering ions, their presence should not lower the sensitivity of the ISEs to NO_3^-. The sensitivity of four sensors was measured between 0.1 and 100 mM concentrations of KNO_3 and NH_4NO_3 fertilizers, and 0.05 to 50 mM $Ca(NO_3)_2$. The sensitivities in KNO_3 and NH_4NO_3 fertilizers were -52.6 ± 5 mV/dec and -51.1 ± 4 mV/dec, respectively, but -29.3 ± 10.6 mV/dec in $Ca(NO_3)_2$. The impact of Ca^{2+} on sensor behavior is important and deserves further study because Ca^{2+} can be present at high concentrations in soil, and is used in

Table 3.2: Nickolsy–Eisenman coefficients for ions found in soil.

Chemical (ppm)	**Concentration**	**Concentration and Salt Used**	$\boldsymbol{K_{A,B}^{POT}}$ **for ISE**	$\boldsymbol{\Delta E}$ **for RE (mV)**
Sulphate	20 ppm	0.2 mM Na_2SO_4	−0.087	−0.67
Sulphate	96 ppm	1 mM Na_2SO_4	−0.019	−4.33
Chloride	35.5 ppm	1 mM NaCl	0.064	0.33
Nitrite	30 ppm	0.65 mM $NaNO_2$	0.086	−0.67
Ammonium	10 ppm	0.55 mM NH_4Cl	0.012	−0.67
Potassium	600 ppm	15.3 mM KCl	0.317	−2.33
Magnesium	400 ppm	16.5 mM $MgCl_2$	0.004	3.67
Phosphate	20 ppm	0.2 mM Na_3PO_4	0.074	2.00
Chloride	5300 ppm	150 mM NaCl	0.002	2.67
Calcium	3000 ppm	75 mM $CaCl_2$	1.377	12.67

fertilizers as well.

3.6 Biodegradable Nitrate ISEs

The nitrate ISEs made of gold ink printed on plastic and encapsulated with Teflon, as used in the experiments above and illustrated in figure 3.6a are not biodegradable. Replacing the conductor, substrate, and encapsulation layer with biodegradable materials is required to make a biodegradable sensor.

One option is to replace the printed gold with conductive zinc ink described in chapter 2. As an initial test of this, Zinc:PVP ink was printed on PHBV—a biodegradable polymer—and paper substrates. The encapsulant remained non-degradable Teflon, and the same nitrate ion-selective-membrane cocktail was drop cast directly on the zinc which was exposed through a laser-cut window in the Teflon. This ISE is illustrated in figure 3.6b.

The zinc ISEs printed on paper substrates showed no response to changing nitrate conditions, which might indicate complete loss of conductivity of the zinc on

paper, as discussed in chapter 2. The zinc electrodes on PHBV took longer than one minute to settle to a new potential after changing concentration. The output potential jumped more than 500 mV or as little as 2 mV for a factor of 10 change in nitrate concentration. The output potential did not return to the same value each time the ISE was in a single concentration. This unpredictable and unstable response, illustrated in figure 3.7, indicated that zinc was not a suitable biodegradable conductor for a potentiometric nitrate sensor. Nitrates are oxidizing agents, while zinc is a reducing agent, thus any contact between the nitrate solution and the zinc electrode, which could happen from diffusion through the membrane, or via pinholes or leaks at the edges of the membrane, invites a reaction between the zinc and the nitrate. It is important to keep zinc well encapsulated and away from open windows in the encapsulation material to prevent this.

Another group of biodegradable conductive materials are forms of carbon. Carbon is not conductive enough to use for efficient radio-frequency antennas, but the higher resistive losses of carbon traces are not detrimental to potentiometric sensor performance because of the very small—ideally infinitesimal—currents involved. Forms of carbon have often been used as solid contact layers in potentiometric sensors [98]. The high surface area and hydrophobicity of carbon can improve sensor stability relative to bare metal conductors.

For initial characterization of carbon as a conductor for nitrate sensors, we began with the simple ISEs shown in figure 3.6c. These are made of carbon on paper with wax encapsulation and do not include a rigid stake or integration with other components. Ultimately, carbon electrodes can be connected to zinc traces leading to the communications chip to form an integrated node. ISEs built like this would use wooden substrates with planarization layers and beeswax encapsulants, as illustrated in figure 3.6d.

Carbon ISEs were fabricated according to the following process. Carbon electrodes, which were 1-inch wide by 2.5 inch-long rectangles, were printed on Bristol paper (Strathmore 500 series 2-ply plate finish) using 114-34A/B187 (Creative Materials, Ayer, MA, USA) carbon ink with a Zehtner Universal Film Applicator and a doctor blade (Zehtner ZUA 2000). A laser-cut stencil defined the electrode geometry. Printed carbon electrodes were cured at room temperature for 24 hours and then encapsulated with 700-μm-thick beeswax sheets. The wax sheets were made by melting white beeswax pellets (Sky Organics, Maimi, FL, USA) in a crock pot. A sheet of plywood was soaked in water, then dipped in the melted wax, which was then peeled off the wet wood. Wax sheets were stored at room temperature, then cut to size using a laser cutter. The window in the beeswax layer was 0.75 inches in diameter, and defined the active area of the sensor, since the carbon strip was broad. A windowless wax sheet was used for back encapsulation while one with a window

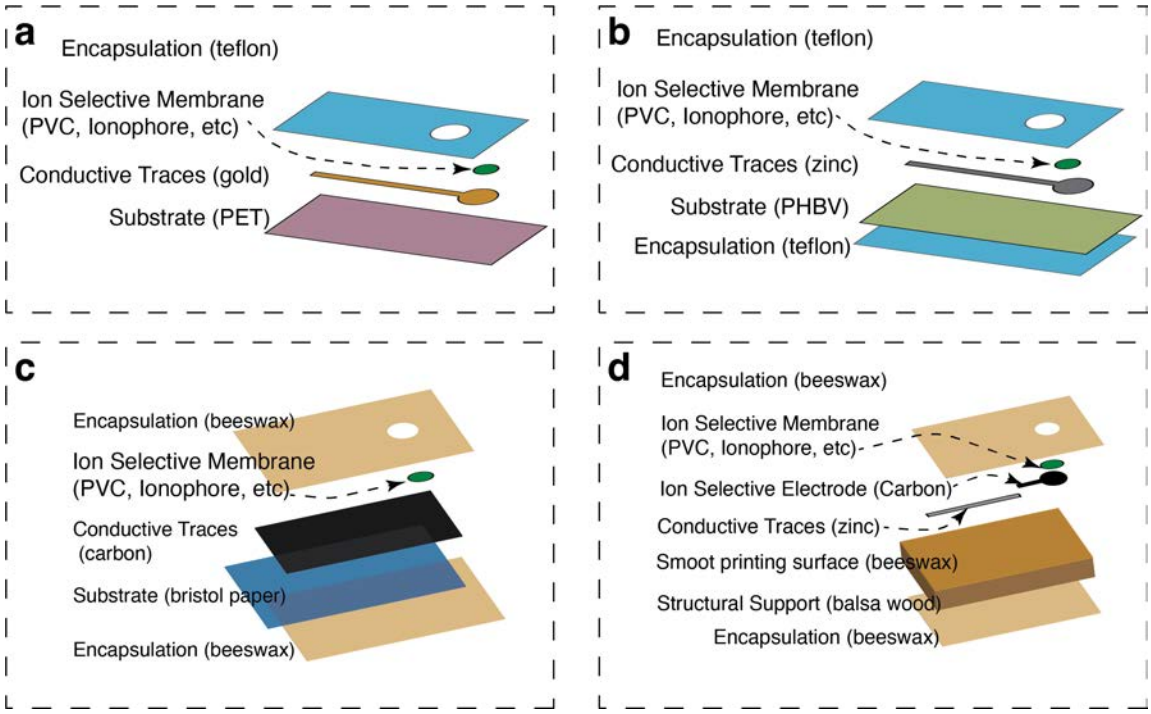

Figure 3.6: a) Conventional, non-degradable ISEs use a PET substrate, printed gold conductor, and teflon encapsulation. b) Initial degradable nitrate ISEs used a PHBV substrate, printed zinc conductor, and teflon encapsulation. c) Functional degradable nitrate ISEs used a paper substrate, carbon conductor, and beeswax encapsulation. d) When integrated into a full sensor node, the ISE is a carbon electrode connected to a zinc trace, with the carbon-zinc joint well away from the active electrode area. The substrate is wood with wax or PCL planarization layer, encapsulated in beeswax.

was used on the front. The wax-paper-wax stack was placed in a 120 °C oven for 2 minutes to briefly re-melt the wax, allowing it to seal to the paper substrate. The ISMs were made by drop casting 180 µL of the same ISE membrane cocktail as was used for the gold electrodes.

Carbon ISE sensitivity was measured first against a commercial reference electrode. The sensitivity of 9 ISEs was -45.5 ±5.7 mV/dec. The average E_0 of the carbon electrodes, -112 mV, was significantly lower than that of gold ISEs, because the wire-carbon and carbon-membrane boundary potentials are different from those of gold. The E_0 variation was 14.5 mV, comparable to the in-batch variation for gold electrodes.

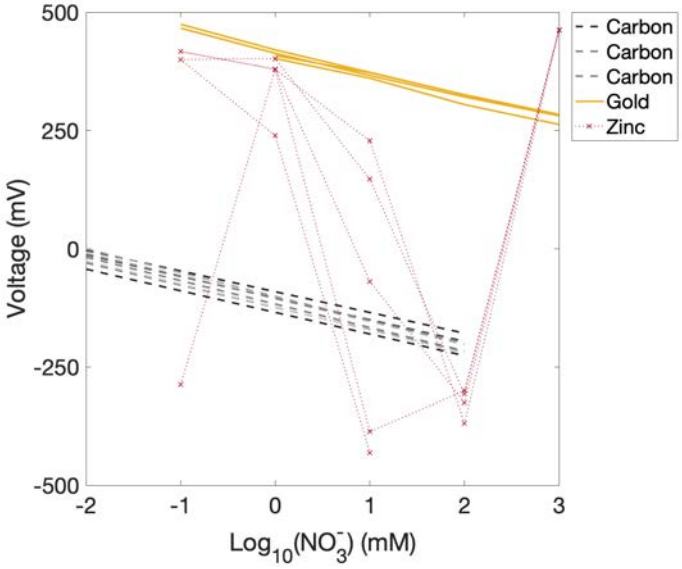

Figure 3.7: Carbon makes a good ISE. Zinc doesn't.

Figure 3.7 shows the sensitivity of several carbon ISEs, together with the response of a zinc ISE, and four gold ISEs as a control. The zinc behavior was clearly different from functional ISEs'. The nearly parallel slopes of the gold and carbon ISEs illustrate their similar sensitivities, while the offset between the groups of lines represents the difference in E_0.

3.7 Fully Printed Sensors

Pairing the printed ISE with a printed RE results in a fully printed sensor which realizes the benefits of printing: low cost, high-throughput manufacturing, no glass or liquid components, and production in form factors that are suitable for use in field deployments. Figure 3.8a shows the potential over time for a printed gold ISE measured against a commercial reference in light blue, and the same gold ISE paired with a printed reference in dark purple. The E_0 value changed, which was expected because the interfaces present in a printed RE are different from those of a commercial RE. For this sample, the fully printed sensor's potential was approximately 87 mV below the printed ISE–commercial RE pair. Both versions had high sensitivity over the 0.1 mM to 100 mM range, response times less than 10 s, and hysteresis less than

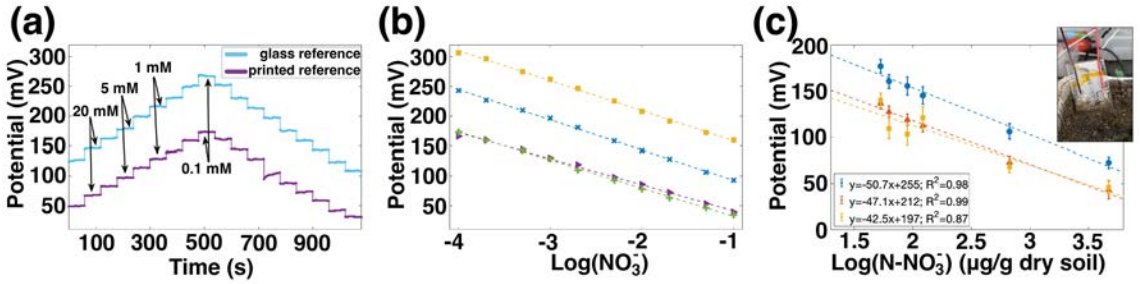

Figure 3.8: a) Potential over time for a gold ISE measured against a commercial glass reference electrode (light blue) and against a printed reference electrode (dark purple). The change in reference electrode changed the E_0 of the pair by 87 mV. b) Sensitivity curves for printed sensors using gold ISEs from two different batches. The average sensitivity for these four sensors is 48.0 ± 3.3 mV/dec. c) Potential versus nitrate concentration for three sensors in a high-organic-matter soil.

5%.

The sensitivity of four such printed sensors, from two batches, is shown in Figure 3.8b. The sensitivity of these gold ISEs when measured against glass REs was -54.3 ± 2.6 mV/dec, which is near Nernstian and comparable to other nitrate ISEs in Table 3.1. When the glass references were replaced with printed references, the sensitivity decreased slightly to 48.0 ± 3.3 mV/dec. This decrease in sensitivity can be attributed to the slight sensitivity of the printed reference electrodes to nitrate. Again, E_0 variation was considerable, particularly from batch to batch. This was expected given the batch-to-batch variability of the ISEs and the sample-to-sample variation of printed REs.

A similar trend was seen for carbon-based nitrate ISEs. The sensitivity of five nitrate sensors made of carbon-on-paper ISEs and silver/silver-chloride-on-paper printed references is shown in figure 3.9a. These ISEs, when measured against glass references, had sensitivity of -40.2 ± 6.2 mV/dec. When measured against printed references, their sensitivity was -39.1 ± 4.3 mV/dec. Again, replacing the commercial reference with a printed reference did not decrease sensitivity.

Next, fully printed sensors were measured in soil. For these measurements, a set of six small pots each containing 50 g of peat soil were prepared. The soil was an agricultural peat soil from Bouldin Island in the Sacramento–San Joaquin Delta, California [103, 104]. Each container was watered to 50% soil moisture by mass using pure water, or 1, 10, 100, or 1000 mM nitrate solution. KNO_3 was used as the source

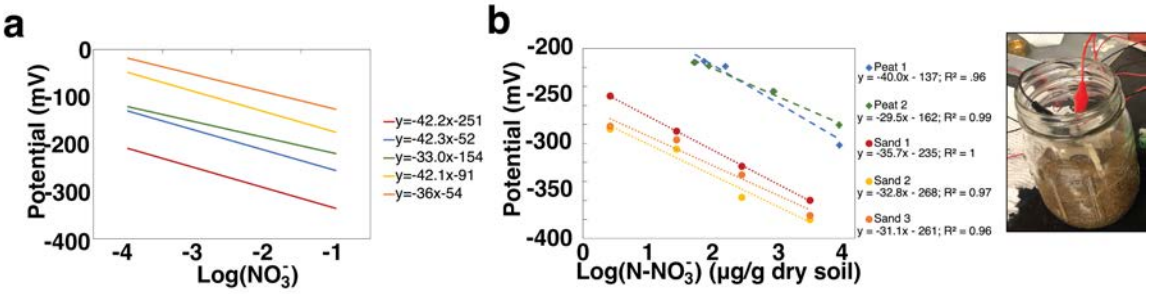

Figure 3.9: a) Sensitivity curves for five printed sensors using carbon ISEs. b) Potential versus nitrate concentration for two sensors in a high-organic-matter soil and three sensors in sand.

of nitrate. The sensors were connected to a Campbell Scientific CR1000 data logger. The sensors were inserted into each container and their potential recorded every 5 s until the output stabilized for at least 3 min per concentration. After measurement in one container, the sensor was removed, rinsed with deionized water, and inserted into the next container. The carbon-based sensors were also measured in sand–a commercially available desert sand from Mosser Lee, (Milston, WI, USA)–following the same procedure.

A post-sensor test KCl extraction was conducted on each soil sample to determine the total extractable nitrate concentration—including background NO_3^- already present in the soil prior to watering—in each soil treatment. Approximately 15 g of each soil sample was added to 75 mL of 2M KCl solution and shaken for 1 hour at 180 rpm. Samples were subsequently filtered through pre-washed Whatman 1 filter paper (Cytiva, Marlborough, MA, USA) and extracts were frozen until colorimetric NO_3^- analysis (EPA-127-A Rev 8) could be performed using a Seal AQ300 Analyzer (Seal Analytical, Mequon, WI, USA).

Figure 3.8c shows the relationship between the non-degradable printed sensors' potential and the log of the concentration of nitrate, which was linear with R^2 values of 0.98, 0.99, and 0.87. The average sensitivity was -47 mV/dec, which was similar to their sensitivity in aqueous solution. This is an important result because it shows that the sensitivity of the NO_3 ISEs in direct soil application—rather than slurries or percolates—can be as good as their sensitivity in solution. The E_0 variation means that each sensor would need individual calibration to provide absolute accurate measurements, rather than relative changes; this is a challenge common to ISEs, including commercial nitrate probes. These results are promising for the future

application of printed ISEs in soil media.

Figure 3.9b shows the response of carbon-based nitrate sensors to nitrate in sand and peat soil. These sensors also had good linearity with R^2 values above 0.96. The average sensitivity in peat was -35 mV/dec, and in sand it was -33 mV/dec. Moreover, the sensitivity of individual sensors (tracked by color in the figure) did not change significantly from solution to soil measurements. The E_0 values cluster by soil type, which raises the question of how soil type impacts sensor performance and what calibration will be needed. This is investigated further in section 6.2.

3.8 Stability

For practical use in agricultural and environmental contexts, sensors need to be stable, meaning they do not drift over time. For less than 5% error in concentration readings over a 90-day lifespan, sensor drift should be less than 1 μV/hour. There are two common causes of drift in solid-state potentiometric ion-sensors: charge build-up from stray currents and water layer formation. In order to understand the origins and solutions of these phenomena, it is helpful to return to fundamental operating principles of a solid-state potentiometric sensor.

The job of an ISE is to transduce a chemical concentration in the surrounding sample to an electrical voltage on a wire. In the ISM, charges are carried by ions, while in the conductor, charges are carried by electrons. To go from ions to electrons, two mechanisms have been used. One is to use a redox-active transducing layer between the ISM and the conductor, which can chemically mediate between ions and electrons. The other approach is to rely on capacitive coupling where the charge on the ISM side of the membrane-conductor boundary is in ions, and the charge on the conductor side of the boundary is in electrons. Simple coated-wire electrodes illustrated in figure 3.10a, like the original demonstrations of solid-state ISEs and the gold electrodes presented here, work on this capacitive principle, but have a small surface are and correspondingly low capacitance. Although current through the device should ideally be zero, in reality it is on the order of pA, and depends on the input impedance of the voltmeter used for measurement. Over long periods of time, this small current accumulates as charge on the capacitor.

Printed carbon has a greater surface area than printed gold, as illustrated in figure 3.10b. The increased surface area increases electrode capacitance, which in turn decreases potential drift over time.

Another source of drift is the formation of a thin layer of water under the ISM, as shown in figure 3.10c. Such a water layer can form from water diffusion through the membrane, percolation through pinholes, or from leaks around the edges. If present,

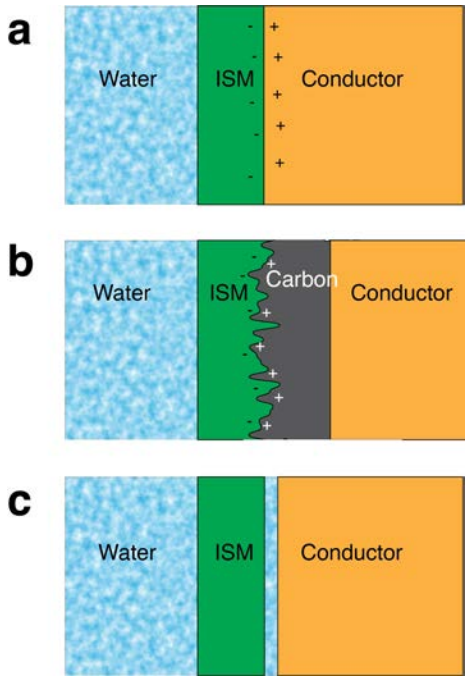

Figure 3.10: a) Simple coated-wire type ISE without a transducer layer between the ISM and the conductor. b) Adding a carbon transducer layer between the ISM and the conductor increases surface area, increases capacitance, and reduces water layer formation. c) A coated-wire type electrode can form a layer of water under the ISM, which causes drift.

diffusion of ions to and from the water layer alters the boundary potentials at the membrane-water and water-conductor layers. The diagnostic test for a water layer was described by Fibbioli et al. [105].

An ideal nitrate sensor will not form a water layer between the ISM and the solid contact or conducting layer. Such an ideal device would have no drift during exposure to high nitrate concentration, when exposed to an interfering solution the potential will change as a step function to a new stable value corresponding to very low nitrate concentration, upon return to the original high nitrate solution, the potential should come back to its original value quickly and stably.

The top panel of Figure 3.11a shows the measured stability of two gold ISEs. In this water layer test, 100 mM $NaNO_3$ was used as the primary solution, and 100 mM NaCl was the interfering solution. First, the ISEs were conditioned in $NaNO_3$ until they were stable. The final hour of stable output in $NaNO_3$ is shown, followed

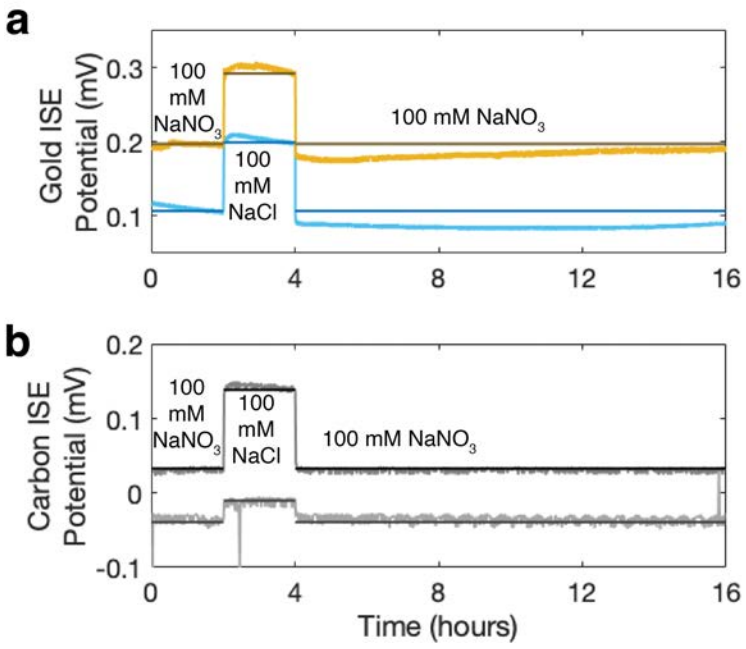

Figure 3.11: a) Water layer test with gold electrodes indicates formation of water layer. b) Water layer test with carbon electrodes shows more stable behavior.

by two hours in the interfering solution, and returning to $NaNO_3$ for 24 hours. The potential showed some drift during both the NaCl step and the $NaNO_3$ return, which could indicate the presence of a water layer on the electrode's surface, which was not unexpected for this type of coated-wire electrode. However, the electrode's stability was surprisingly good—on par with values reported in the literature, which involved specific modifications for stability. The difference between the potential immediately before and the potential immediately after the NaCl step was 15 mV, for the ISE shown in yellow, the same as found by Chen for electrodes using gold nanoparticles and Polypyrrole (PPy) to improve stability [93]. The drift over time for our electrodes was 0.7 mV/h, which is comparable to the 0.8 mV/h and 0.9 mV/h for screen-printed electrodes reported by Jiang and Fan, respectively [106, 86].

In addition to the increased surface area, a printed carbon layer is more hydrophobic than printed gold. The hydrophobicity helps prevent the formation of a water layer. Figure 3.11b shows water layer tests for two carbon ISEs. Both were very stable in $NaNO_3$ and NaCl. Their potentials returned to their pre-NaCl values almost immediately after the move from NaCl back to $NaNO_3$.

3.9 Conclusions

We designed and fabricated fully printed potentiometric nitrate sensors comprising a printed nitrate ISE and printed RE. The printed nitrate ISEs showed a near-Nernstian sensitivity of -54.1 ± 2.1 mV/dec when paired with a glass RE. A printed RE with low sensitivity to nitrate was developed using a membrane composed of PVB, NaCl, and $NaNO_3$. Fully printed nitrate sensors demonstrated sensitivity of -48.0 ± 3.3 mV/dec in solution and -47 mV/dec in soil. Printed sensors were not significantly impacted by sulphate, chloride, phosphate, nitrite, ammonium, potassium, and magnesium at concentrations expected in soil, but calcium did interfere with sensor behavior.

The fabrication methods used here are scalable and relatively low-cost when compared to conventional electronics. Because the sensors are passive, they would require little power to be read, which is advantageous when integrating into wireless sensor nodes. As a result, they could be widely distributed throughout a landscape to map the movement of nitrate through the watershed, inform efficient application of fertilizer, or alert residents to elevated nitrate levels in drinking water.

Chapter 4

RF Antennas

Sensors are only useful if their data can be read, which means data transmission is required. For a network of many sensors, that transmission should be wireless, because wired connections would involve many miles of wires, and create a real rat's nest of cables. All wireless communications rely on antennas of some type. An antenna is "the transitional structure between free-space (propagation of radio frequency, or RF, waves) and a guiding device" such as coaxial wires that deliver current and voltage to a circuit [107]. As such, any time an electronic signal goes from currents and voltages in a circuit to electromagnetic waves or vice versa, an antenna is involved.

For the agricultural sensor nodes, passive Ultra High Frequency Radio Frequency Identification (UHF-RFID) was chosen as an initial wireless communication protocol because it enables battery-free sensor nodes and medium-range communication distances. This protocol dictates operation in the 902-927 MHz frequency band in the US, so antennas must be designed to operate in that band.

This chapter has two parts. First, non-degradable antennas for use in free space are designed, printed, and characterized. These antennas demonstrate the advantages and disadvantages of different printing techniques and prove good functionality of very compact antenna designs. Sections of this work were originally published as "Printed, flexible, compact UHF-RFID sensor tags enabled by hybrid electronics" [108]. Next, antenna designs are modified for use with biodegradable substrates, encapsulants, and conductors. This chapter focuses solely on the physical performance of the antennas. Integration of printed antennas with RF integrated circuits (RFICs) to form complete tags and the connection of printed sensors to these tags is discussed in Chapter 5.

4.1 Antenna Design

Antenna design begins with an understanding of electromagnetic (EM) wave propagation and basic antenna types. Here, we focus on modified half-wavelength dipoles. Dipoles have a simple structure, and are planar, making them easy to print. All the metal surfaces are on one side of the substrate, so through-vias are not needed. Dipoles use less metal than slot or patch type antennas, and for biodegradable applications, minimizing total metal in the system is desire able, even though the metal is biodegradable. Further, as we will see, dipole designs can be modified to fit in a small area footprint, allowing for compact and unobtrusive sensor stakes.

Dipole Antennas

A half-wavelength dipole is essentially a wire. It is connected to an external circuit by a feed line which joins the dipole at a small gap at its center and provides current when the antenna is transmitting. When an antenna is receiving, the process is the same as transmission but in reverse. The current is time-harmonic (sinusoidally varying) and spatially distributed along the dipole's length as a cosine function, with nulls at the ends and a peak at the feed line, as illustrated in figure 4.1a. The time harmonic current in the wire generates time-varying magnetic fields **B**, as illustrated in figure 4.1b, which in turn create time-varying electric fields **E**, leading to propagating EM waves, according to Gauss's laws. The wavelength of the EM wave is set by the length of the dipole, as shown in figure 4.1c. The EM waves propagate away from the dipole symmetrically about the axis of the dipole, with nulls at the ends of the wire, as illustrated in figure 4.1d. This donut-shaped radiation pattern is characteristic of dipole antennas, and can also be represented by two 2D plots, as shown in figure 4.1e. More complete physical descriptions of antenna radiation mechanisms can be found in numerous textbooks, for example Ulaby [109] for introductory material and Balanis [107] for extensive mathematical derivations.

Another fundamental property of an antenna is its input impedance, Z_{in}, which is defined as $Z_{in} = \frac{\tilde{V}}{\tilde{I}}$ where $\tilde{V}$ is time-harmonic voltage, $\tilde{I}$ is time-harmonic current, and Z_{in} is generally complex. The real part of Z_{in} represents power radiated away from the antenna, and the imaginary part represents power stored in fields near the antenna. A standard half-wavelength dipole has $Z_{in} = 73 + j42.5\Omega$. In systems, the antenna impedance must be matched to that of the load or line to which it is connected. Matching means that the impedance of the antenna is the complex conjugate of the load. Impedance matching will be discussed in more detail in section 4.3 and 5.2. For now, we will use a load of 50+0jΩ, which is the impedance of standard coaxial cables used in the lab.

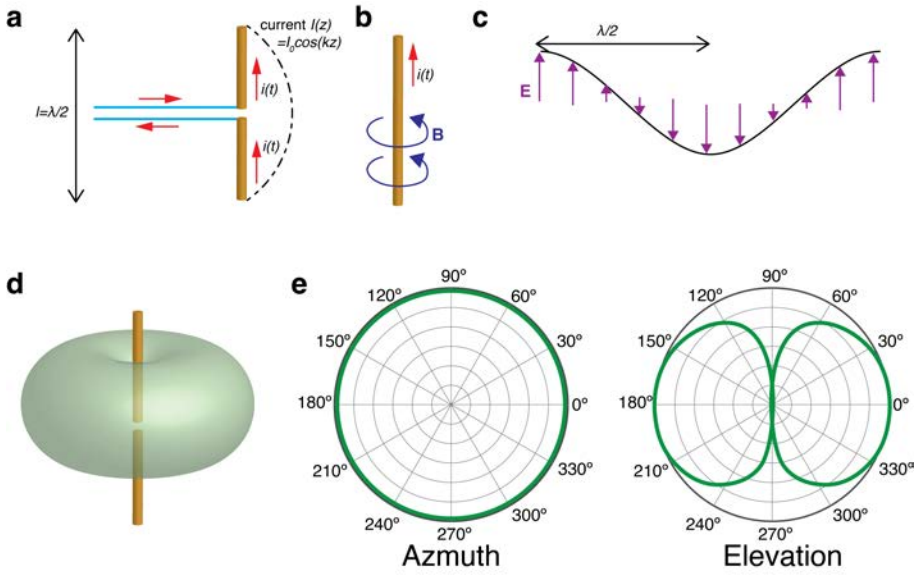

Figure 4.1: a) A half-wavelength dipole is two wires connected to a feed line at a narrow gap in the middle. b) Time-varying current in a wire creates time-varying magnetic fields, which generates time-varying electric fields, becoming electromagnetic wave propagation. c) The wavelength of the electromagnetic wave generated is set by the length of the dipole. d) A dipole radiates symmetrically in all directions away from the wire, with nulls at the poles of the wire. e) The classic dipole's donut-shaped radiation pattern can be represented by two 2D plots instead of a 3D rendering.

Folded Dipoles

The impedance of a standard half-wavelength dipole, like the one shown in figure 4.2a, is a fundamental property of that geometry. Changes to the antenna geometry can change the input impedance while keeping the wavelength constant. One way to do this is to use a folded dipole, which is a narrow loop of wire, as shown in figure 4.2b. This structure works as a transformer and antenna at once, and generally serves to increase Z_{in}. For planar, printed folded dipoles, the impedance can be tuned by the width and spacing of the lines.

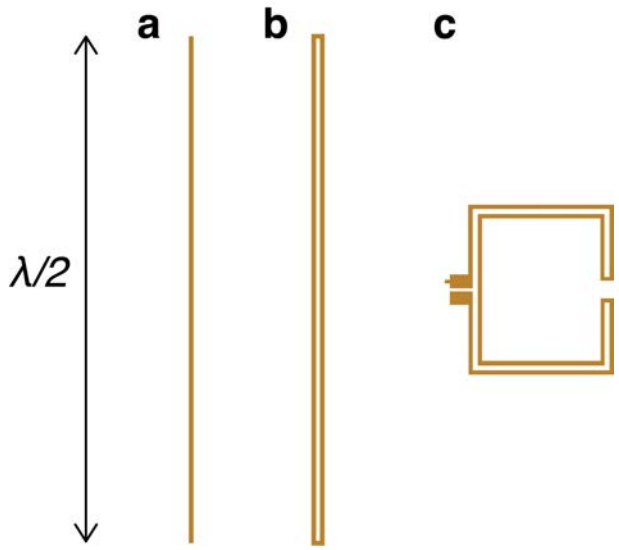

Figure 4.2: a) A standard half-wavelength dipole. b) A folded dipole is a very narrow loop of wire that is still a half-wavelength from end to end. Width and gap dimensions can be used to vary input impedance. c) The arms of the folded dipole can be bent in to form a more compact antenna.

Miniaturization

The wavelength and frequency of all waves are related by their velocity u according to equation 4.1.

$$u = \lambda f \tag{4.1}$$

For EM waves, velocity is the speed of light c, divided by the relative permittivity, ϵ_r of the material the wave is traveling in, which is 1 for air. Thus, for waves at 915 MHz in air, the wavelength is

$$\lambda = \frac{c}{f} = \frac{3 \times 10^8 \text{ m/s}}{915 \times 10^6 \text{ Hz}} = 32.79 \text{ cm}$$

This means that a half-wavelength dipole for 915 MHz would need to be about 16 cm long, which becomes cumbersome for fabrication and intrusive in in-field installation.

Antenna miniaturization is an area of antenna design which aims to reduce the size of an antenna while maintaining acceptable performance [110]. This reduction in size can be of the longest linear dimension, D, the area, or the volume of the

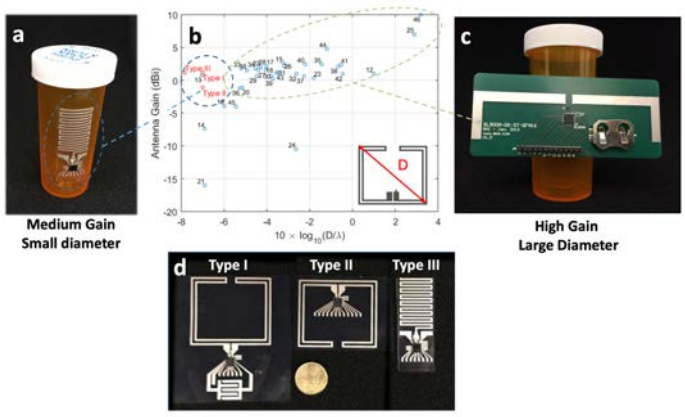

Figure 4.3: An overview of the printed tags presented in this manuscript in comparison to the state of the art. a) A printed, flexible, meander monopole antenna can be used in a passive UHF RFID tag that is easily integrated onto a small, non-conformal package like a pill bottle. b) Printed antennas on a flexible substrate reported in literature (black circles) can have high to moderate antenna gain. However, such antennas also have large diameter relative to their operating wavelength (D/λ), where "diameter" refers to the longest distance between two points on the antenna, as illustrated in the inset. This makes them less suitable for applications where small form-factors are desirable. Other examples in literature that pursued a smaller D/λ resulted in antennas with low gains (bottom of the figure). Notably, the antennas described in this work (red circles) have small D/λ and moderate gain. c) A typical dipole antenna with large D is not suited for integration on small packages. d) This work presents three types of printed, passive tags on flexible substrate for operation in the UHF RFID band (902-928 MHz). The antennas used in Type I are externally-fed folded dipoles, type II are internally-fed folded dipoles, and type III are on meander monopoles with ground pads on the front side of the substrate. All tags operate using an RFIC mounted on printed traces.

antenna. Typically, small antennas have much poorer performance–often quantified by the antenna's gain–than their larger counterparts.

Figure 4.3b shows that in literature, antennas with small longest linear dimension typically also have reduced maximum antenna gain [111, 112, 113, 114, 115, 116, 117, 118, 119, 120, 121, 122, 123, 124, 125, 126, 127, 128, 129, 130, 131, 132, 130, 131, 133, 134]. The antennas designed and studied here have small linear dimensions wile preserving reasonable gain, as shown in Figure 4.3b.

Design and Simulation Methods

Antenna design began with numerical simulations. An antenna type and dimensions were chosen based on the envisioned application, specifications on antenna geometry, and boundary conditions of the fabrication. For example, folded dipole type antennas were chosen for the reasons described above, and minimum line width was set to about 500 μm based on printing limitations. Initial designs were proposed and simulated in an electromagnetic solver, which returns antenna parameters like impedance and gain. The dimensions and feeding strategy of an antenna were adapted digitally in order to optimize antenna parameters and ensure compliance with the predetermined specifications. However, simulation results typically differ from reality because of assumptions and idealizations made in the calculations, so physical antennas were fabricated and characterized as part of the antenna design. With this information numerical models were updated to more closely match measurements.

The antennas were designed using numerical simulations in the finite-difference time-domain (FDTD) simulation software Sim4Life (ZMT, Zürich, Switzerland). The dipoles were developed based on the designs presented in [112]. The dimensions of the dipole traces were adapted to achieve a target power reflection coefficient < -10 dB in the UHF RFID frequency band (902-928 MHz in the USA) in reference to 50 Ohms. The meandered monopole was designed to be compatible with stencil printing methodology, which limits trace thickness and inter-trace spacing were to 1 mm. The meander width and number of meanders were varied in order to achieve a power reflection coefficient < -10 dB in the UHF RFID frequency band. The conductive traces were modeled as conductive sheet with σ equal to the conductivity of the conductive ink used for screen printing ($\sigma = 5 \times 10^6$ S/m) and the PEN substrate as a brick with $\epsilon_r = 3.5$, $\sigma = 0$ S/m, and thickness = 125 micrometer. Conductive traces were modeled with a maximal grid step of 1 mm in the FDTD algorithm. The substrate was modeled with a single step of 125 micrometer in the transverse dimension and maximal steps of 1 mm in the other two dimensions. The antennas were fed a Gaussian pulse with center frequency 1 GHz and bandwidth 1 GHz using a voltage source. The voltage and current on the antennas are monitored using the simulation software and the simulation is terminated once those quantities reach a steady-state solution.

4.2 Antenna Fabrication

Here, we describe antenna fabrication with several different printing techniques. The performance of a physical antenna depends on its fabrication method. Many meth-

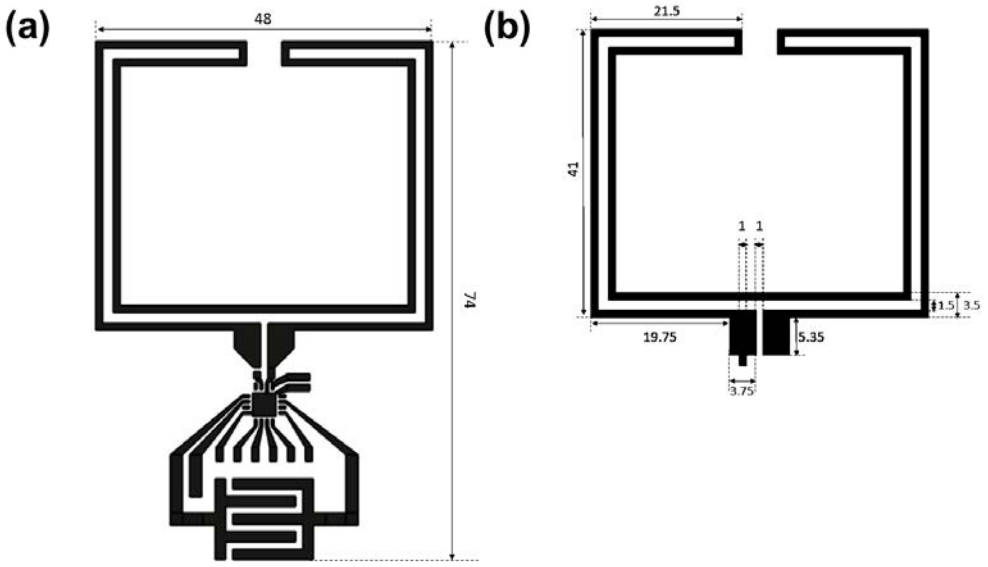

Figure 4.4: Dimensions of a printed folded dipole antenna. a) Complete RFID tag including the antenna, traces for mounting the IC and matching inductor, and printed capacitive touch sensor. b) The antenna alone used for S11 and radiation pattern measurements.

ods of printing have been used to make RF systems and antennas [135, 136], including screen-printing [111, 115], gravure-printing [137], spray-coating [112] and inkjet-printing [113, 138, 139]. Using our first antenna design, Type I (see Figure 4.4), we characterized the impact of printing technique on antenna performance by printing the same antenna with four different techniques: inkjet printing, stencil printing, spray coating, and screen printing. The printing technique impacted trace thickness, overall profile shape, edge and surface roughness, and sample-to-sample variability. These physical parameters in turn impacted the RF performance of the antenna.

Antenna Printing

Tags and antennas were fabricated using different printing techniques on plastic substrates. All samples were printed on a 125 μm-thick polyethylene naphtalate (PEN) substrate (Q65HA from Teijin Dupont Films, Wilmington, DE, USA).

Inkjet Printing Antennas were printed with DGP 40LT-15C silver ink (Advanced

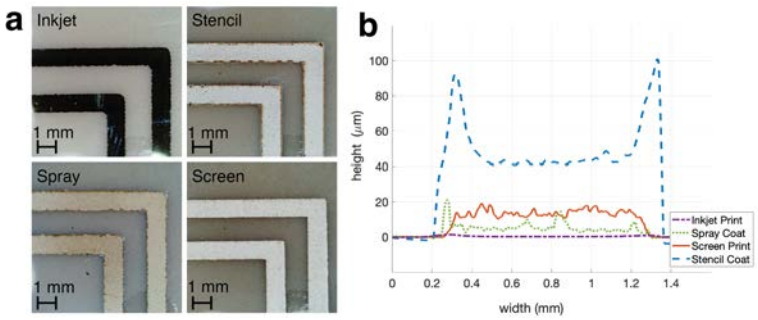

Figure 4.5: a) Microscope images of the top-left corner of the antenna show surface and edge roughness of patterns made with inkjet, stencil, screen, and spray printing (in a clockwise direction). b) Profiles of traces printed with the same four techniques. The vertical axis shows the trace height, while the horizontal axis shows the traces' transverse direction. The colors indicate different printing techniques.

Nano Products, Sejong, Korea) using a Dimatix DMP-2850 inkjet printer (Fujifilm Dimatix, Santa Clara, CA, USA) with a 10-pL cartridge. Samples were printed with a drop spacing of 25 μm and a platen temperature of 52 °C during printing, and annealed in a vacuum oven for one hour at 140°C .

Spray Coating Patterns were defined using laser cut stencils. The stencils were cut from adhesive Kapton film (Dupont) using a laser cutter (Universal Laser Systems Inc, Scottsdale, AZ, USA). Silver ink designed for spray coating, PSPI-1000 ink (NovaCentrix, Austin, TX, USA), was applied by hand with an aerosol brush. After printing, the samples were annealed at 130°C for 15 mins.

Stencil Printing The stencils for stencil printing were prepared in the same way as the stencils for spray coating. Silver ink, 126-33 extremely conductive silver ink (Creative Materials, Ayer, MA, USA), was applied using a razor blade held in contact with the stencil. Samples were annealed on a hot plate at 130°C for 10 min, then the adhesive stencil was removed.

Screen Printing The screens were ordered from NBC Meshtech (Bavaria, IL, USA). Screen printed samples used the same ink and annealing conditions as stencil printed samples.

Antenna Profiles Thickness and roughness of the traces produced by each technique were measured with a Veeco Dektak MG stylus profilometer.

Figure 4.5a shows the edge roughness of one corner of Type I antennas made with the different printing techniques. Inkjet printed traces had a smooth surface and periodic extensions along the edge. The regularly spaced bulges resulted from

the spreading of regularly spaced ink droplets. The stencil and spray coated traces were defined by laser-cut adhesive stencils as described in the methods section. The laser cutting of the stencils made rough edges which can be seen in both these sets of traces. The screen printed traces had comparatively straight edges.

The thickness profiles of traces made with these four techniques are shown in figure 4.5b. The inkjet printed traces were by far the thinnest, at about 200 nm thick. This is typical for inkjet-printed traces, which are made with relatively small volumes of low viscosity ink. The stencil printed samples had the thickest traces of 43 μm, while the spray-coated traces were about 3-8 μm thick, and the screen printed samples were about 20 μm thick. The large ridges on the edges of many stencil printed samples and some spray coated samples formed when ink dried on the edge of the tape stencil and remained after the stencil was removed. The surface roughness, quantified here as the root mean square error of the central portion of each trace, also depended on fabrication method. The surface roughness was 14 nm, 2.3 μm, 1.6 μm, and 2.0 μm for inkjet, spray, stencil, and screen printed traces respectively. Surface roughness has some impact on the impedance of printed RF components with lower roughness leading to lower Ohmic resistance [140].

The thickness (t) of the traces significantly impacts their resistance and RF efficiency. Thin conductors are characterised by their sheet resistance (R_s), with $R_s = \rho/t$ [in $\Omega/\square$]. The resistivity ρ [in $\Omega - m$] is a material property; in inks it is determined by the type of conductor (silver, for all of our inks), as well as the type and concentration of additives and binders in the ink, and the annealing conditions. The ink used for inkjet printing had the lowest $\rho = 1.15 \times 10^{-7}\Omega - m$, while the conductivity of the ink used for screen and stencil printing was $\rho = 2 \times 10^{-7}\Omega - m$ and that of the spray coating ink was $\rho = 8.5 \times 10^{-7}\Omega - m$. However, because the inkjet-printed traces were much thinner than those obtained using any other techniques, the sheet resistance was highest for inkjet printing with $R_s = 0.5\Omega/\square$ in comparison to $R_s = 1.8 \times 10^{-2}\Omega/\square$ and $R_s = 2.9 \times 10^{-2}\Omega/\square$ for stencil and screen-printing, respectively.

For AC applications, comparing the skin depth (δ_s) to trace thickness provides insights about the current distribution and losses in a thin trace. AC current travels along the edge of a conductor, and the skin depth gives an indication of the thickness of a conductive material that carries current. Skin depth is given by:

$$\delta_s = \frac{1}{\sqrt{(\pi f \mu \sigma)}} \tag{4.2}$$

where $\sigma = \frac{1}{\rho}$ is the conductivity, $f = 915MHz$ is the frequency of interests, and $\mu = \mu_0 = 4\pi \times 10^{-7}[H/m]$ is the magnetic permeability [109]. A conductor whose

thickness is less than δ_s will have significant losses compared to a thick conductor or an infinitely thin perfect conductor. At 915 MHz, using the inks' resistivities, we found $\delta_s = 6\ \mu m$ for inkjet-printed traces, $\delta_s = 15\ \mu m$ for spray coated traces, and $\delta_s = 7\ \mu m$ for stencil and screen printed traces, which were made with the same ink. The screen-printed and stencil printed traces had a thickness that exceeded their δ_s, while the spray coated traces were somewhat thinner than their δ_s, and the inkjet-printed traces were more than an order of magnitude thinner than δ_s in that material. This means that the inkjet printed trace suffered significant losses compared to the other printing techniques.

4.3 Antenna RF Characterization

Methods

During all measurements the antennas were directly connected to an SMA cable using the 292-64A-06 connector. Voltage reflection coefficient (S_{11}) measurements of antennas printed using different techniques were executed using a VNA (Agilent N5242A, PNA-X, Santa Clara, CA, USA). All S_{11} measurements were executed in reference to 50 Ω. Antenna Gain measurements of antennas printed using different techniques were executed using two-port measurements with the same VNA. The VNA registered two-port S-parameters of two antennas mounted at a fixed distance of 61 cm. S-parameter were averaged over 50 sweeps from 500 MHz to 1500 MHz with 1001 frequency steps of 1 MHz and were then used in the three-antenna method [141] to determine antenna gain. During these measurements, all antennas were placed parallel with their printed sides facing each other in a mirrored configuration. Antenna gain as function of (θ, ϕ) and polarization were measured with the same VNA in the same setup as the antenna gain measurements. During these measurements, one antenna was kept static, while the second antenna in the transmission measurement setup was rotated in either the azimuth angle (ϕ) or the elevation angle (θ) in order to obtain the dependency of G_ϕ and G_θ on both components, resulting in a radiation pattern. Antenna bending measurements were executed using the screen-printed antennas and the same VNA with the same configuration as the measurements described above. During these measurements, one antenna was kept static, while the second was bent around it's middle horizontal and vertical axes of the antenna as shown in the insets of figure 4.7b.

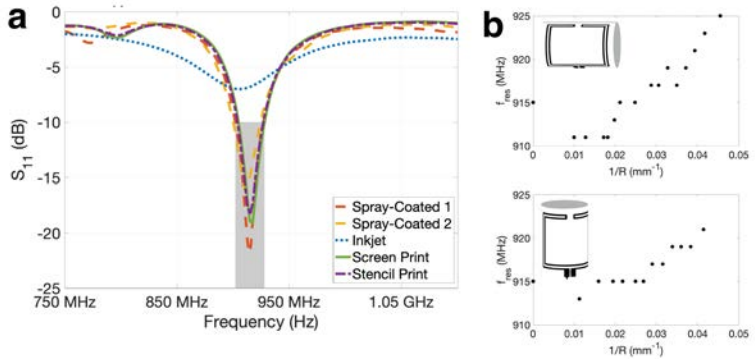

Figure 4.6: a) Power reflection coefficient (S11) parameters show that spray coated, stencil printed, and screen printed samples achieve good resonance (S11 ¡ -10 dB) in the targeted 902-928 MHz band, while inkjet printed samples have a much smaller resonance peak. b) Bending the antenna around a smaller radius shifts the resonance peak (frequency where S11 is the lowest) to higher frequencies. Up to radii of 20 mm, the peak stays within the 902-928 MHz band.

Results

The physical properties of the printed samples influenced the RF performance of the printed antennas. We quantified the RF performance using three parameters: antenna power reflection coefficient ($|S_{11}|^2$), antenna impedance, and antenna directvitity/gain. The $|S_{11}|^2$ of the Type I printed antenna fabricated using different printing techniques were measured to characterize the RF performance of the antennas. $|S_{11}|^2$ is a standard performance metric for antennas [142]. At the resonant frequency small $|S_{11}|^2$ (large negative values in dB) indicate that most of the power provided to the antenna is not reflected but is transmitted. Our design targeted 90 % accepted power in the UHF RFID frequency band, illustrated by a grey rectangle in Figure 4.6a. We defined the bandwidth of an antenna as the range of frequencies over which the antenna complies with this design goal, i.e. it has an $|S_{11}|^2 \leq -10\ dB$. The resonant frequency of the antenna is that frequency where S11 is minimal. The inkjet-printed samples did not meet the target of having a $|S_{11}|^2 \leq -10\ dB$ in the UHF-RFID band, due to their limited trace thickness. The stencil-printed samples had a resonance peak at 915 ± 3.5 MHz and bandwidth of 23 ± 1 MHz, while spray coated antennas had a peak at 913 ± 1 MHz and 24 MHz bandwidth. Screen printed samples' resonance was at 917 ± 2 MHz with a bandwidth of 24 ± 1 MHz.

The effect of bending the flexible antennas was studied by bending the antenna

in two directions, see Figure 4.6b. We have verified that when the antenna was bent, its resonance frequencies increased, which is illustrated in Figure 4.6b for bending around two orthogonal axes. Bending the antenna reduced its size, which increased the resonant frequency. Bending radii down to 24 mm for both axes did not shift the antenna out of the desired frequency band. Bending the antenna down to a radius of 24 mm shifted the resonance frequency by -1% and 0.7%, respectively. Therefore, this antenna design is functional when the tag is flexed. The minimum bending radius was limited by the rigid SMA connector.

The reflected power measured by S_{11} comes from impedance mismatch between the generator, cables, and the antenna. RF equipment is designed to have standard impedance of $50 + 0j\Omega$. A load perfectly matched to its feed line has impedance equal to the complex conjugate of the line, which is also $50 + 0j\Omega$. The reflection coefficient S_{11} is a complex number which is related to the complex impedance of the antenna (Z_A) by:

$$S_{11} = \frac{Z_A - Z_L}{Z_A + Z_L} \tag{4.3}$$

where Z_L is the impedance of the feed line, 50 Ω. From this, the impedance of the antennas was calculated [107]. Screen-printed samples ($N = 8$) had a real impedance of 48 ± 3 Ω at 915 MHz, while stencil-printed samples ($N = 7$) had a real impedance of 51 ± 6.9 Ω at the same frequency. These were also in good agreement with the simulated value of 50 Ω. The inkjet-printed antennas had relatively large imaginary impedance ($Im(Z) = -50 \pm 1.8$ Ω, $N = 4$), caused by the limited thickness of the traces.

Directivity describes how an antenna directs the power it radiates; it is defined as "the ratio of radiation intensity in a given direction to the radiation intensity averaged over all directions"[110], which is commonly plotted on a polar plot or three dimensional rendering. If given as a single number, directivity refers to the maximum value. It is usually more practical to measure gain (G), which is the directivity times the radiation efficiency. Radiation efficiency is the ratio of power radiated by the antenna to power accepted by the antenna and accounts for losses in the antenna. Gain is given in units of dBi, where the "i" indicates the measurement is with respect to isotropic. An antenna with a gain of 0 dBi would radiate the same power in a given direction as an isotropically radiating source. A linear, half wavelength dipole orientated along the z-axis has maximum gain of 1.64 (2.15 dBi) in the x-y plain, and nulls along the z-axis [107].

We designed and characterized three types of antennas. Type I was a folded dipole which is fed from the outside of the antenna. Type II was a very similar folded dipole fed from inside the square. Type III was a meandered monopole, with

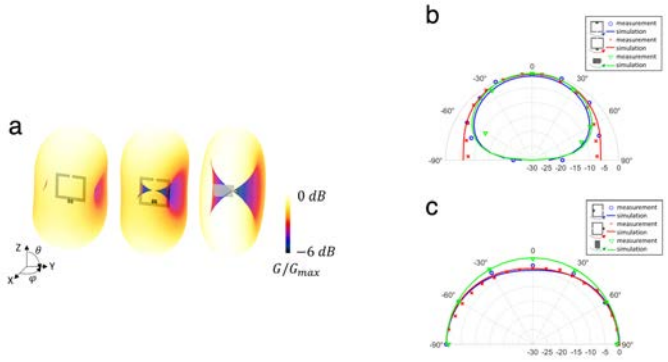

Figure 4.7: Wireless performance of the studied printed antennas and tags. a) Simulated (solid line) and measured (discrete points) radiation patterns (in terms of antenna gain normalized to the maximum antenna gain) for each of the three types of antennas. b) 3D representations of the simulated radiation patterns shown in (a). The colors indicate relative strength of the antenna gain. All antennas show desirable, dipole-like radiation patterns with uniform gain at $\phi = 0$ and varying elevation angle, as well as two nulls at $\theta = 90^o$ and varying azimuth

small ground pads on each side of the monopole. We measured the gain patterns of each of the three antenna types by rotating one antenna along the azimuth and zenith angles and measuring power transmission from one antenna to the other, as described in the methods section.

Figure. 4.7a provides three dimensional renderings of the normalized gain of each antenna type. Figure 4.7b,c shows the measurements of the antenna gain as a function of the azimuth angle and zenith angle. The simulated and measured radiation patterns were very similar to those that are theoretically expected for a dipole antenna, although the folding slightly increased the gain in the plane of the print. The measured gain patterns showed relatively good correspondence with the simulated values, indicated by the solid lines.

For each antenna type, we measured absolute antenna gain in the direction of maximum gain where possible, using screen printed samples. Type I had a simulated gain of 1.3 dBi, and we measured 1.2±0.2 dBi. Type II antennas had a simulated maximum gain of 1.6 dBi, but we were unable to measure in the direction of maximal linear gain due to the feeding strategy and connector attachment. We instead measured in the direction orthogonal to the plane of the antenna and found a gain

of -1.1 ± 0.1 dBi, compared to a simulated gain of -1 dBi in that direction. Type III antennas were simulated with a maximum gain of 1.1 dBi, and we measured a gain of 1.15 dBi for these antennas.

4.4 Biodegradable Antennas

The materials that an antenna is made of influence how it resonates. In moving from nondegradable to biodegradable antennas, the conductor changed from silver to zinc, the substrate from PET to wax-coated wood, and a top wax encapsulation layer was added. Each of these new materials impacts antenna performance, and design modifications are needed to account for such.

Substrates and Encapsulation

Recall from section 4.1 that the frequency at which a dipole antenna resonates is set by

$$f = \frac{c\epsilon_r}{2l} \tag{4.4}$$

where c is the speed of light, ϵ_r is the relative permittivity of the medium around the dipole, and l the dipole's length. The substrate and encapsulation layers around an antenna change the effective ϵ_r and thus the resonant frequency of the antenna. The impact of the substrate and encapsulation layer can be accounted for by changing l, the physical size of the dipole. This phenomenon was first explored in simulation and appropriate scaling factors were determined for expected substrate and encapsulation thicknesses. Next, antennas were printed in a variety of sizes to verify this technique and the scaling factor needed for actual wood and wax properties.

Simulations

The folded dipole antennas designed above were modified using numerical simulations in Ansys HFSS 3D Electromagnetic Field Simulator (Ansys, Canonsbur, PA, USA). The conductive traces were modeled as conductive sheet with σ equal to the conductivity silver ($\sigma = 1.75 \times 10^6$ S/m) and thickness 20 μm, and the PEN substrate as a brick with $\epsilon_r = 3.2$, loss tangent = 0 S/m, and thickness = 100 μm. Beeswax layers were modeled with $\epsilon_r = 2.6$ and loss tangent = 0 S/m, and wood layers were modeled as balsa wood with $\epsilon_r = 1.3$, and loss tangent = 0 S/m. Simulations used the driven modal mode with a lumped port with Z=50Ω. Frequency was swept with 401 points from 456 GHz to 1.37 GHz, centered at 915 MHz. The antenna geometry

began with the design from section 4.1, and all dimensions, including trace width and gap width, but not the lumped port width, were scaled to fractions of their original size.

In simulation, the full scale folded dipoles on PET substrates resonate in the 902-927 MHz band, as shown by the black dotted line in figure 4.8a. Full-scale folded dipoles simulated on 5 mm balsa wood with 1 mm beeswax encapsulation layer on top and bottom resonate at about 800 MHz, shown by the solid gray line in figure 4.8a. Scaling down the antenna's physical dimensions while holding the substrate and encapsulation conditions constant leads to an increase in resonance frequency, as shown in figure 4.8b. The relationship between size and frequency is linear in simulation. This linear relationship provides a design approach where a beginning antenna size can be tested on a desired set of substrate and encapsulation materials, and the offset between the measured or simulated resonant frequency and the design frequency can be used to calculate an appropriate scaling factor for that material set.

Measurements

Antennas were stencil printed on PET substrates using silver ink and the methods described in section 4.2. Stencils used the folded dipole design at 100, 95, 90, 85, 80, 75, and 70% of the original size, with all dimensions except the feed points scaled evenly. One set of antennas was attached to pre-cut wooden backing boards using a thin layer of molten wax. Another set was attached to wood backing boards and encapsulated by a layer of wax. An acrylic jig was laser cut to fit around the antenna and prevent accidentally wax coating of the feed points. The jig was taped to the mounted antenna and molten wax was poured into the opening. After the wax set, a doctor blade heated on a 300 °C was used to reflow and remove excess wax. The thickness of the acrylic jig and the resulting wax layer thickness was 1 mm. A third set of antennas were left unmounted and uncoated as a control. Antenna $|S_{11}|$ parameters were measured with the same VNA and SMA connections as above.

Figure 4.8c shows how decreasing size increases resonant frequency for three antennas printed on PEN (shown in blue) with 100%, 85%, and 75% of the original design size. The 85% size resonates at 1080 MHz on PEN, but 945 MHz on a wooden substrate. Likewise, the 75% antenna resonates at 1226 MHz on PEN, but 900 MHz on wood when encapsulated with 1 mm of beeswax. Figure 4.8d shows the linear relationship between size and resonant frequency. The wax encapsulation condition has a different slope between frequency and size, but is still a linear relationship. From these relationships, an antenna designed for wood with 1 mm wax encapsulation should be 73% as large as an antenna designed for 100 μm PEN. We now have

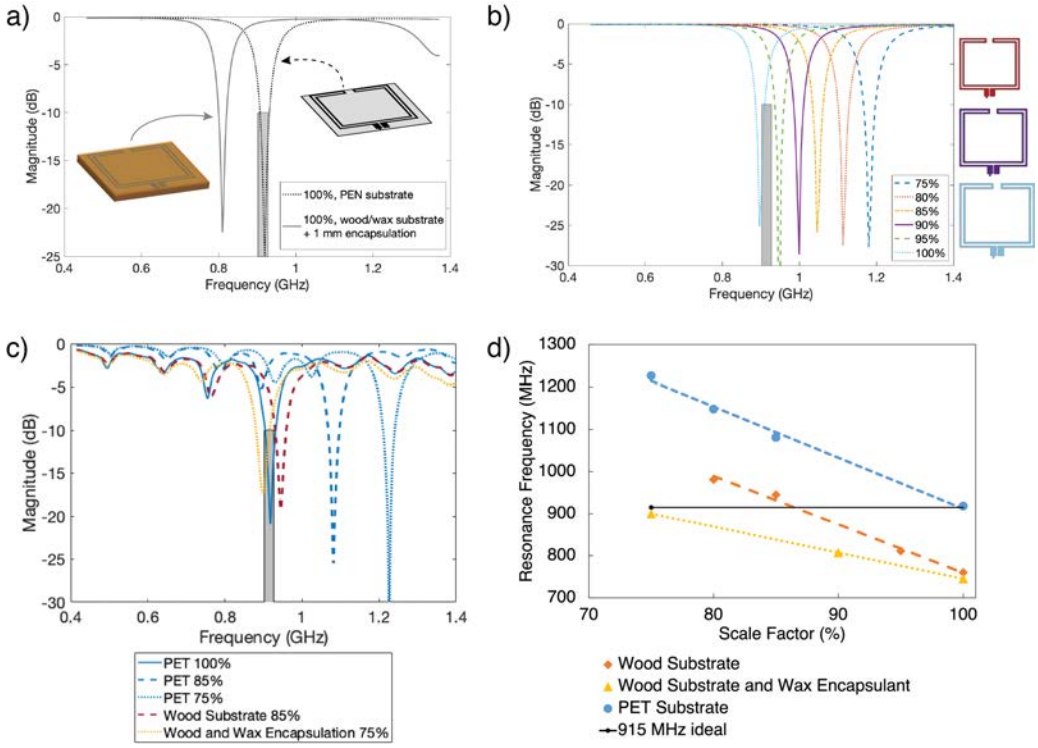

Figure 4.8: a) A folded dipole antenna on an 100 µm PEN substrate in simulation has a radiation peak within the 902-927 MHz design band, indicated by the gray rectangle. The same antenna simulated with a 5 mm balsa wood substrate and 1 mm beeswax encapsulation layer has a resonance peak of around 800 MHz, well outside the desired band. b) Scaling down the antenna's physical dimensions while holding the substrate and encapsulation conditions constant leads to an increase in resonance frequency. The relationship between size and frequency is linear in simulation. c) The measured resonance of different size antennas follows the pattern expected from simulations. d) There is a linear relationship between antenna size and resonance for printed antennas measured on PET substrates, wood substrates, and wood substrates with wax encapsulation layers.

a system with two knobs to control frequency: antenna size and encapsulation thickness. For a given wax thickness, an optimal size antenna can be chosen, and vice versa. However, thick encapsulant layers also contribute to damping, so antennas that are very small with very thick encapsulation layers do not behave exactly the same as antennas that are large with thin layers.

Conductor

The sheet resistance of the conductor that forms the antenna influences the depth of the resonance peak. This trend was clear from the printing techniques study described in section 4.3. Biodegradable conductors have lower conductivity than commercially available silver inks. Here, we use simulations to determine the maximum acceptable sheet resistance for antennas to have a resonance peak below -10 dB. The zinc ink developed in chapter 2 is then used to print antennas that meet the specifications.

Simulations

Simulations were done in Ansys HFSS using the original scale folded dipole. Zinc ink was simulated with conductivity of 1×10^5 S/m and thicknesses of 20, 40, 60, 100, and 1000 µm. Figure 2.12a shows the simulated S11 parameters of these zinc antennas with various thicknesses. The thicker the ink, the deeper the resonance peak. Changing thickness does not shift resonance frequency. A tungsten ink with conductivity of 5000 S/m and 60 µm thickness for a sheet resistance of 3.3 Ω/□ was also simulated to represent more common biodegradable conductors. This antenna had no resonance peak at all, highlighting the importance of high conductivity ink for biodegradable antennas.

Measurements

Antennas were screen printed zinc on PET substrates. Both Zn:PVP:NMP and Zn:PCL:Anisole ink formulations were used. Antennas were encapsulated in beeswax by dip coating one or two layers of wax. The Zn:PVP antennas were measured the day after they were made using the same VNA as for the other measurements. The Zn:PCL antenna was measured 11 days after it was printed. Antennas were also printed with Zn:PVP:NMP on wood and wax substrates, but did not remain conductive long enough to measure S11 parameters. The DC resistance of all antennas was measured, which was used to calculate the sheet resistance of the zinc.

Figure 4.9b show the measured S11 values for five printed zinc antennas. All the antennas have distinct resonance peaks, and two of them, with the highest conductivity, have peaks that meet the threshold of below -10 dB. The precise location of the resonance peaks depends on the wax coating thickness for the four antennas with peaks grouped around 800 MHz. These four antennas used the original size antenna designed for no encapsulation layer. The antenna with the deepest peak was made with a scaled-down design for thicker wax encapsulants and resonates near 1 GHz.

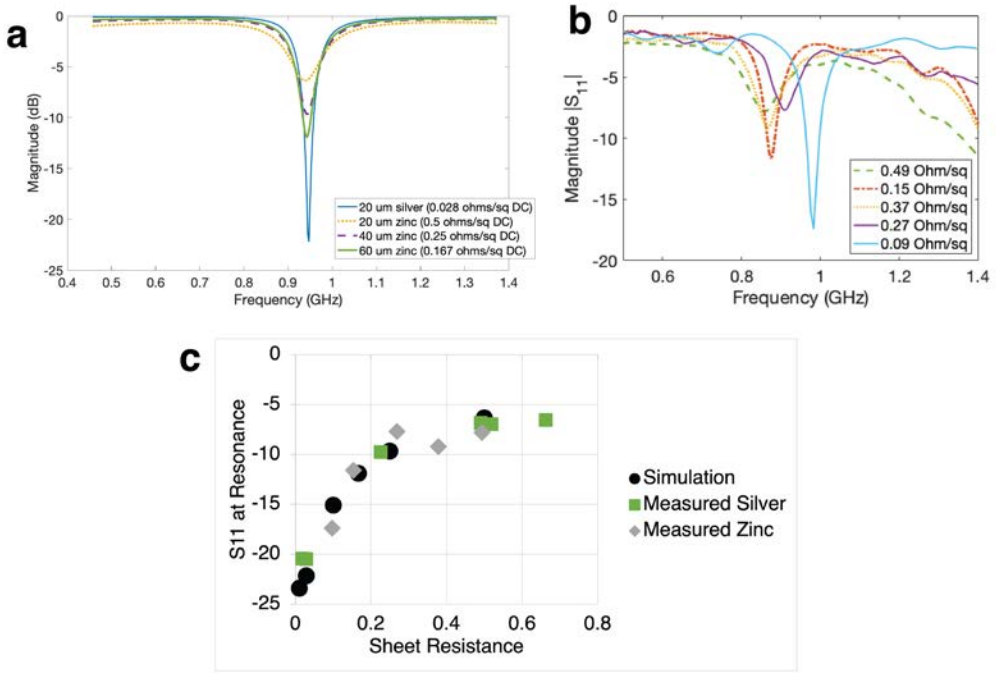

Figure 4.9: a) simulated S11 parameters for zinc antennas of various thicknesses to achieve different sheet resistances. b) measured S11 parameters for zinc antennas printed on PET substrates and encapsulated by dip coating in wax. c) the relationship between DC sheet resistance and S11 at resonance is the same regardless of type of material (silver or zinc) and well modeled by simulation.

This antenna, with a resonance peak of -17.4 dB, was made with PCL-based ink, showing an application of the ink developed in chapter 2.

Figure 4.9c shows the relationship between S11 and antenna sheet resistance for simulations, silver antennas made with different printing techniques, and zinc antennas. The trends for silver and zinc antennas align well, indicating that it is indeed the sheet resistance, not the material itself, that dictates depth of resonance peak. Both sets of measured data align well with simulations. In order to achieve resonance of at least -10 dB, sheet resistance of 0.2 $\Omega/\square$ or less is required.

4.5 Conclusions

These miniaturized antennas featured moderate gain and small linear dimensions. Different printing techniques were investigated to fabricate this antenna. Screen-printing the antenna was found to lead to the most efficient antenna, with stencil printing using a disposable stencil as a good precursor for screen-printing. Inkjet printing did not lead to antennas with sufficient efficiency because of high sheet resistance.

The compact antenna designs were scaled to resonate at 915 MHz when printed on wood substrates and protected by wax encapsulants. The biodegradable zinc ink developed in chapter 2 was used to make antennas with acceptable performance. These antennas are ready to be integrated with silicon ICs to form RFID tags.

Chapter 5

Integration

In chapter 3, nitrate sensors were presented. In chapter 4, the antennas were optimized. In order to form a functional sensor node, the printed antenna must be physically and electrically connected to an RF integrated circuit (RFIC) and the sensor needs to be connected to these readout electronics. Figure 5.1 illustrates conceptually integration as the combination of existing functional parts.

In part 1 of this chapter (sections 5.1 to 5.6), we discuss the connection between printed antennas and RFICs, and demonstrate a battery-free RFID sensor tag capable of sensing on-board temperature and interactive touch. Sections of this work were originally published as "Printed, flexible, compact UHF-RFID sensor tags enabled by hybrid electronics" [108]. In part 2 (section 5.7), we discuss readout electronic requirements for potentiometric sensors and lay the foundations for their integration with the printed RFID tag.

5.1 Chip Attachment

Connecting printed conductive traces to conventional, rigid silicon ICs packaged in plastic is not a trivial task, particularly when the printed traces are on a flexible substrate. Conventional solder, widely used in the electronics industry for attachment of electrical components, is incompatible with the low temperature limits of printed materials, and, depending on the solder type and printed trace material, undesirable chemical reactions may occur. In this section, a method for attaching rigid, packaged electrical components is developed, with attention to both mechanical stability and electrical connection.

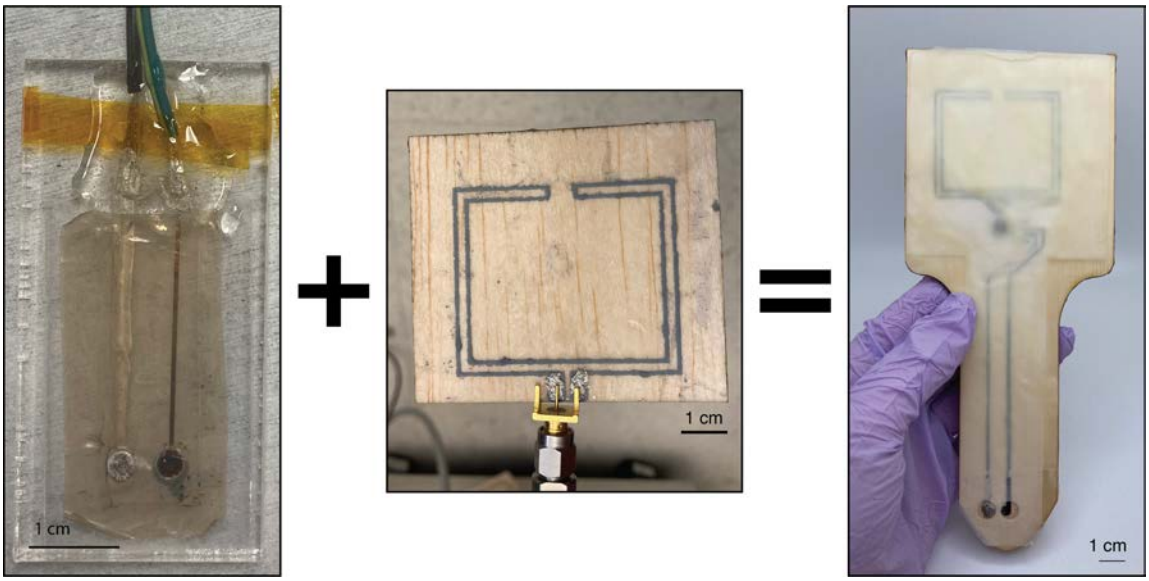

Figure 5.1: The optimized nitrate sensor and the optimized antenna need to be combined together with an RFIC in order to form a complete sensor node.

Mounting Mechanisms

To mount a chip or other discrete component with the contacts are facing down, the solder or conductive adhesive goes between the chip and the pre-patterned substrate, as shown in Fig 5.2. Precise alignment of chip pads to printed traces is important, so a flip-chip pick-and-place tool is used to align chips with the conductive traces printed on the substrate. Processing parameters and materials must be chosen such that the conductive material does not spread and short the contact pads together. One of the key choices is the conductive adhesive material used, labeled "wet ink" in figure 5.2.

Conductive Adhesive Materials

There are many materials that can be used for chip attachment, including solders, conductive adhesives, and inks.

In order to determine which conductive adhesive or ink would work best with screen or stencil printed silver ink on PEN, several types of conductive adhesives, epoxies, and inks were tested. RF test traces were printed with a gap of a few millimeters in one side. 0603 form factor [1.55 × .85 mm footprint] zero-ohm resistors

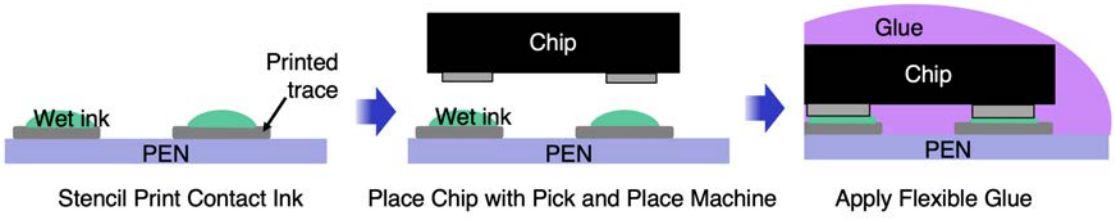

Figure 5.2: Pick-and-place tools are used to align pads to traces for chips mounted contacts-down.

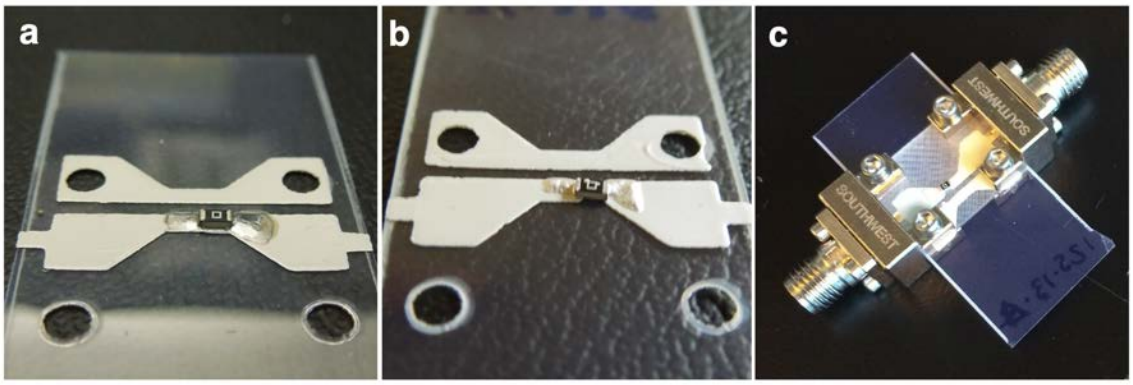

Figure 5.3: a) Zero-ohm resistor mounted with low temperature solder. b) Zero-ohm resistor mounted with screen printable silver ink. c) Test traces connected to adapters for RF cables.

were attached using several different materials and the RF power loss, $|S12|$ or power transmitted from one terminal to the other, was measured using the VNA. Another set of test traces were shorted with the various conductive materials. A printed trace with no gap was used as a control. The results are shown in table 5.1.

From these results, Creative Materials 125-13H screen printable silver ink was chosen for attaching components because of its low RF losses. Other advantages of 125-13H are its long drying time of over 30 minutes, which allows a time buffer during attachment, and ability to cleanly stencil print small features.

Material	Connection Type	RF Loss at 915 MHz [dB]
none	through	-0.5
	Open	-42
Ted Pella Conductive Silver paint (PELCO # 16062)	Zero Ohm Resistor	-32
	Short	-5.7
MG Chemicals Silver Conductive Epoxy Adhesive	Zero Ohm Resistor	-1.2
	Short	-1.0
Creative Materials 125-13H Silver Screen Printable Ink	Zero Ohm Resistor	-0.7
	Short	-0.7
Creative Materials 120-07: Fine Features Screen Printable Ink	Zero Ohm Resistor	-1.2
	Short	-0.7
Koki M742 Low Melting Point Sn-Ag-Bi Solder Paste	Zero Ohm Resistor	-0.9

Table 5.1: Resistive losses at RF frequencies for conductive adhesive materials

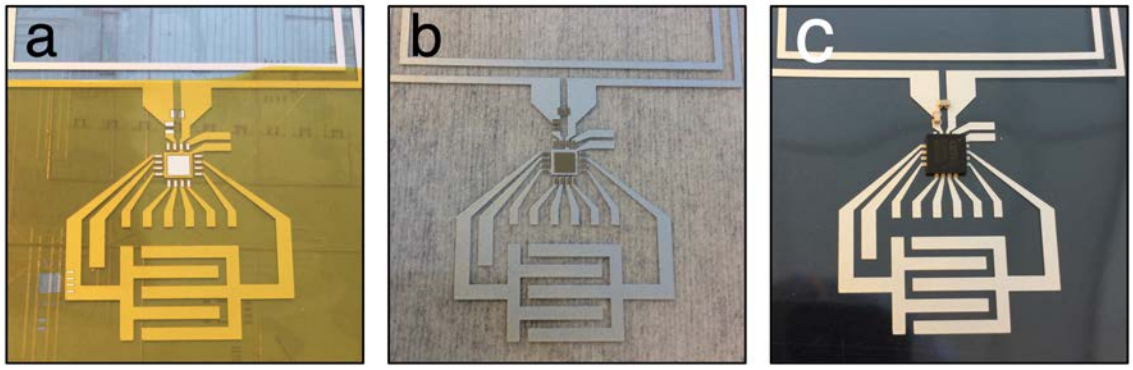

Figure 5.4: Rigid components are attached to to a screen-printed tag in three steps: (a) a laser cut stencil is used to define areas where (b) conductive ink is applied with a razor blade. (c) The components are placed with a pick-and-place tool.

Stencil Printing Attachment Process

To mount the RFIC, an SL900A by AMS (ams AG, Premstaetten, Austria), using the chosen Creative Materials 125-13H silver ink, first, we laser-cut a kapton stencil with holes for each of the chip's landing pads, as shown in figure 5.4a. The stencil is 50 µm thick non-adhesive kapton film (DuPont). The thinness of the stencil was

important as it limited total ink volume applied and thus controlled spreading of the ink and shorting of the traces. The stencil and substrate were held in place with a gel-pack backing layer, and a razor blade was used to deposit the ink through the stencil. The wet ink lined up with the already-printed traces is shown in figure 5.4b. A pick-and-place die bonder was used to align and mount the rigid components on the wet ink. The ink was cured at 180 °C for three minutes. Figure 5.4c shows the mounted chip. Finally, both the RFIC and the passives were coated with a few drops of Loctite 4902 flexible super glue, which dried at room temperature for several hours.

5.2 Impedance Matching

The chip attachment process described in section 5.1 allows for physical connection between the chip and the substrate, as well as DC electrical connection between the I/O pins and the printed traces. At RF frequencies, an additional impedance matching step is required to facilitate power flow between the antenna and the RFIC.

Recall that impedance is $Z = \frac{\tilde{V}}{\tilde{I}}$, where $\tilde{V}$ and $\tilde{I}$ are time-harmonic voltage and currents. The impedance of an antenna is set by its geometry, which was designed to be $50+0j\ \Omega$ for the folded dipole antennas. The impedance of an RFIC is determined by the RF-front end circuitry, which is set by the IC designers, and cannot by changed by chip's end users. Many RFICs have a significant negative imaginary, or capacitive, component to their impedance.

Impedance mismatch between the $50 + 0j\ \Omega$ antenna and capacitive IC causes power losses which can be characterized by the power transfer coefficient, (τ), defined as:

$$\tau = \frac{4Re(Z_{ant})Re(Z_{IC})}{|Z_{ant} + Z_{IC}|^2} \tag{5.1}$$

where Z_{ant} is the antenna's impedance and Z_{IC} the IC's impedance. Maximum τ is achieved when the antenna and the IC's impedances are conjugate matched, i.e. $Z_{ant} = Z_{IC}*$. In order to match the antenna and the chip, we first needed to know the impedance of the chip. The IC's data sheet listed RF input impedance as $123 - 303j\ \Omega$ for packaged die, but impedance can change when a chip is mounted on a substrate. We measured the impedance of eight RFICs mounted on flexible substrates for input powers from -20 to +13 dBm and found that impedance ranged from $1.3 - 55j\ \Omega$ at low input power to $21 - 46j\ \Omega$ at high input power.

Impedance matching can be achieved either by changing the antenna's geometry to match the IC [142] or by using a matching network. We chose not to alter the antennas because they were designed with $50+0j\ \Omega$ impedance to be compatible with

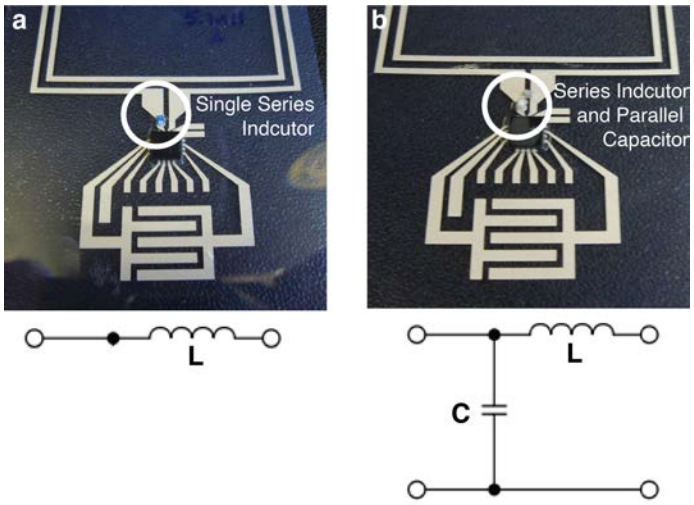

Figure 5.5: a) A single inductor in series between the chip and the antenna provides some matching. b) A series inductor and a parallel capacitor provide another degree of freedom and possible perfect impedance matching.

standard RF equipment. Designing the antennas this way makes them compatible with a variety of ICs with various impedances, which is discussed in more detail in section 5.5.

Matching networks can be made of discrete (lumped) passive components in series and parallel. We designed two styles of matching networks: a single series inductor, shown in figure 5.5a, and an L-match with series inductor and shunt capacitance, shown in figure 5.5b. While the best L-match networks had higher matching efficiency in theory, we encountered two limitations in practice. One was that the L-match was highly sensitive to the exact values of the inductor and capacitor, beyond the tolerance of surface-mount components. For example, a tag with an L-match network consisting of nominally a 10 nH and an 18 pF capacitor, which are standard component values, would have $\tau = -13$ dB, which is no better than an 10 nH inductor alone. This is illustrated in figure 5.6. The second challenge was that L-matches designed for the impedance of the chip at low input power were ineffective at high input power and vice versa. The single inductor did not provide as high a degree of matching, but it did tolerate a wider range of inductance values and provides improvement to the impedance match for input power between -20 and +13 dBm.

Using a single inductor reduced the imaginary part of the denominator in equa-

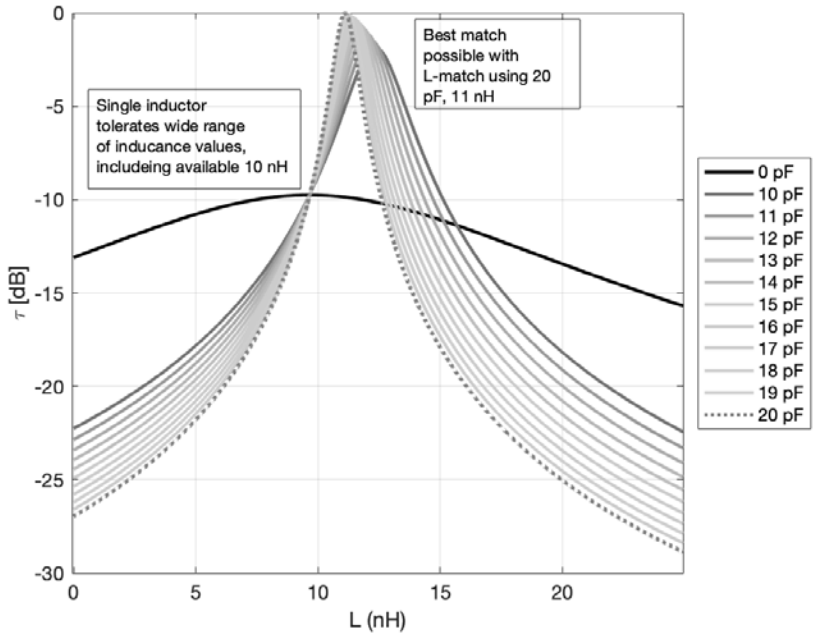

Figure 5.6: Matching networks that include a series inductor and a parallel capacitor can provide a very high degree of matching in theory. However, slight variations in actual inductance lead to poor matching. A single series inductor provides acceptable matching across a wide range of values.

tion 5.1, which increased τ and consequently the received power. According to measured values of the IC's mounted impedance, inductor values between 5-15 nH offer effective matching. To confirm this experimentally, a variety of inductors in this range were attached to tags using the chip-attachment process described in section 5.1. The effectiveness of inductors at matching was characterized with over-the-air testing of the tags.

5.3 Over-the-Air RF Tag Performance Testing

We characterized the performance of the RFID tags by measuring their Return Signal Strength Indicator (RSSI) and read range. Both were measured with an RFID interrogator set up. The interrogator antenna transmitted an RF signal which traveled to the tag. The tag used the energy harvested from the RF signal to power on and

modulate its impedance to encode its unique ID in the reflected, or backscattered, RF wave. The backscattered wave traved back to the read where it was received. RSSI is a measurement of the power received by the reader. The read range is the maximum distance between interrogator and tag over which the tag can still respond. Both RSSI and read range are functions of the RFIC and the physical arrangement of the antennas and other objects in their vicinity.

Power transmission in free space is governed by the Friis equation, 5.2.

$$P(d) = P_T \times G_1 G_2 \frac{\lambda^2}{(4\pi d)^2} \tag{5.2}$$

Where $P(d)$ is the power at a given distance, P_T is the transmit power, G_1 and G_2 are the gains of each antenna, λ is the wavelength, and d is distance between the antennas. The actual power received by the tag at distance d, P_R, is $P_R = P(d) \times \tau \times m_{pol}$ where m_{pol} is the polarization mismatch and τ the power transfer coefficient from above. These equations can be rearranged to find the maximum distance that a certain power will be received.

The maximum read range, r_{max}, of an RFID system is given by equation 5.3

$$r_{max} = \frac{\lambda}{4\pi} \sqrt{\frac{G_T G_R P_T m_{pol} \tau}{P_{th}}} \tag{5.3}$$

Power can be increased by using antennas with higher gain, ensuring they are properly aligned to reduce polarization mismatch, and increasing the power transfer coefficient (τ) between antenna and RFIC. Increasing transmission distance will always decrease received power, which imposes a maximum read range for a wireless link.

The RFID interrogator set up was made of a commercially available RFID reader system (Thingmagic Sargas, Trimble, Sunnyvale, CA, USA) connected to a circularly polarized RFID reader antenna (MT- 262024/TRH/A/K from MTI Wireless Edge) with 30 dBm output power. The tags were placed with their printed surface parallel to the surface of the RFID-reader antenna at a distance of 5 cm and were moved away from the reader antenna in the direction orthogonal to the reader antenna in steps of 5 cm. At every step in separation distance, the reader registered the received signal strength indicator (RSSI) value that was returned by the tag. RSSI measurements were collected using Sargas's web GUI. Twenty RSSI values were registered at every location and determined the average (in decibels) RSSI over distance. Figure 5.7a shows the set up for measuring free-space transmission between powered the RFID antenna and a printed tag.

The effectiveness of using a single series inductor for impedance matching was experimentally verified by measuring RSSI at a fixed distance (48 cm) for tags with

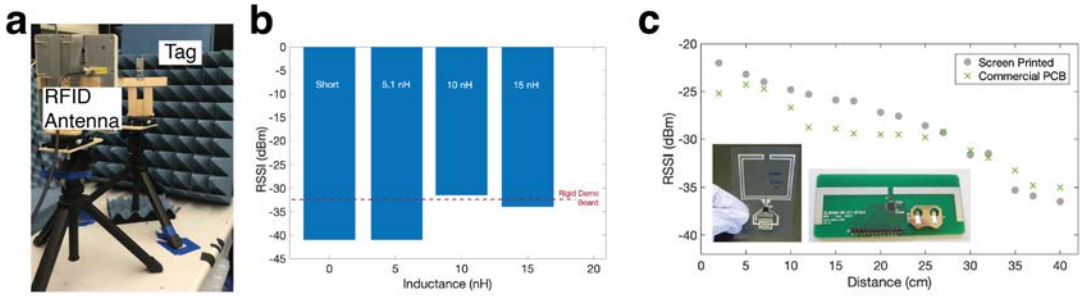

Figure 5.7: a) Set-up for over-the-air measurements of RSSI (return signal strength index). b) Using a 10 nH inductor for impedance matching between a screen printed folded dipole provides the highest RSSI at 48 cm reading distance. c)The RSSI of printed RFID tags matches or exceeds that of commercially produced, rigid RFID tags using the same IC.

0,5.1, 10, and 15 nH. The results are shown in figure 5.7b. As expected from section 5.2, the series inductor improved RSSI relative to an unmatched tag, and 10 nH was the optimal value.

Figure 5.7c shows the RSSI of a screen printed folded dipole tag and a rigid reference board for transmission distances between 5 and 40 cm. For both tags, RSSI decreased over distance as expected in free-space propagation. The screen-printed folded dipole tags returned higher RSSI-values than the rigid PCBs closer to the reader (distances < 30 cm) and comparable values at further separation distances (distances 30 - 40 cm). These measurements were repeated with the internally fed folded dipoles and meandered monopoles from chapter 4, referred to as Type II and Type III respectively. For mid-distance transmission (between 15 and 35cm) the average RSSI of Type I tags was -30 dBm, for Type II tags it was -25 dBm, and for type III tags it was -24 dBm. The rigid reference board had an average RSSI of -30 dBm over the same range of distances. Type I and II tags' read range was measured at 40$\pm$2.5cm, while that of Type III tags was much longer, 90$\pm$2.5cm, and the read range of the reference board was 60 cm.

5.4 Over-the-Air Data Transmission

With chips attached and matched to antennas, the next step is to use the RFID tags to stream data from sensors. Here, we show streaming of data from temperature sensors built into the IC, and from external printed capacitive sensors.

Over-the-Air Calibration of Tag Temperature Sensor

We used tags with all three antenna designs to wirelessly transmit sensor data. We first demonstrated transmission of sensor data using the RFIC's on-board temperature sensor. The interrogator antenna and two tags were placed inside the chamber (Associated Environmental Systems, Ayer, MA, USA), separated by about 20 cm. The chamber went through three temperature cycles (10°C to 30°C and lowered again to 10°C) at different relative humidities (RH): low humidity (10 to 30% RH), medium humidity (45 to 50% RH), and high humidity (80 to 90% RH). A reference measurement inside the chamber was executed using a wired probe (RH520A, Extech Instruments, Boston, MA, USA).

Figure 5.8 (b) shows the setup in an environmental chamber used to calibrate the temperature sensor of the screen-printed RFID tags. In humid environments, many polymers absorb water, which changes their material properties and can impact the performance of devices fabricated on these substrates. The sensitivity to humidity depends on the specific material. Figure 5.8 (c) shows the temperature measured by the RFID tags in green compared to the wired reference temperature measurements in black. Each of the three antenna types, as well as a rigid reference board, were tested. The printed tags showed increases and decreases in temperature that aligned very well with the measurements of the references probe, once the measure data were filtered for outliers. There was an average relative error of 0.15 % on the temperature measurements. We found that the tags were able to accurately measure temperature regardless of the humidity. At high humidity, the data from printed tags did have spikes due to irregularities in the wireless communication. In general, these errors were fairly uncommon: 6 % of the measurements for tag Type I and lower percentages for the other tags. Our calibration measurements showed that our strategy to use the RFIC's temperature sensor with our fabrication technique led to reliable temperature measurements in different humidities.

Over-the-Air Tag Capacitive-Touch Read-out

Sensor tags can be made more versatile by integrating different types of external sensors. We chose to integrate a printed capacitive touch sensor to illustrate this possibility. Capacitive touch senors are composed of interdigidated electrodes which have some capacitance between them. The fringing fields extend out of the plane of the electrode, making them sensitive to the environment nearby [143, 144, 145]. When a finger, whose dielectric constant is much greater than that of air, is placed on the sensor, the capacitance of the sensor increases. The capacitive touch sensor was made with five fingers, with overlap length of 9 mm, width of 1.5 mm, and gap spacing

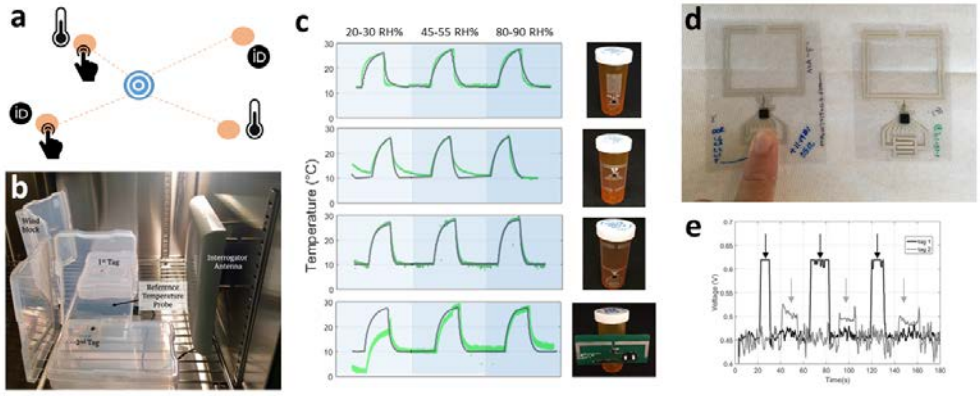

Figure 5.8: Applications using the printed, flexible, passive tags developed in this study. a) The tags developed in this work, which have a variety of self contained and user-interactive sensors, can form a passive star network with a central active reader. This kind of network only requires the central node to have an energy source, while still allowing for distributed sensing and user-interaction. b) Calibration set-up for measuring temperature in a humidity-controlled environment. Two tags are simultaneously interrogated by the reader antenna. A reference temperature probe is placed between the two tags under test to validate the wireless temperature readouts. c) Results from the temperature measurements show good agreement between wired reference temperature monitor (black) and passive, wireless printed tags (green, top three panels) regardless of humidity. The rigid tag (lower panel) has significant error in low humidity. d) User interacting with a capacitive touch sensor integrated with a type I tag. e) Backscattered sensor data from two type I tags being wirelessly interrogated simultaneously. The user alternated between touching tag 1 and tag 2, and touch events show as elevated voltage readings. This demonstrates that passive networking of user input is feasible using the proposed tags.

of 1 mm. The layout is included in Figure 4.4a. These capacitors had an average capacitance of $1.33 \pm .04$ pF when not touched. Capacitance increased up to 24 pF when touched, depending on the force of the touch. The capacitor is measured by the RFIC in a voltage-divider set up. We used the small stray capacitance between two printed traces as the reference capacitor in the voltage divider. The RFIC measured the voltage on its analog input ports. Figure 5.8d shows two of the fully printed sensor tags with capacitive touch sensors at the bottom. The patterns for the sensing capacitor and reference capacitor were incorporated into the antenna screen

layout, resulting in a complete sensor tag that was printed in a single pass.

During these measurements, the tags were laid on a brick of styrofoam at 20 cm from the same UHF-RFID reader used in the previous section. The tag's voltage sensor 1 was interrogated continuously using the wireless channel and a time series of the measured voltage was stored on the reader's side. Sensor measurements were recorded using Mercury API java scripts from ThingMagic. The tags were then touched periodically on the capacitive touch sensor. These measurements were executed for two tags simultaneously, in order to show the networking abilities of the UHF-RFID setup using our screen-printed tags.

Fig 5.8e shows the transmitted voltage detected by the external voltage sensor of two different screen-printed RFID tags that simultaneously transmitted that voltage using UHF-RFID backscattering. The touch events were clearly visible in the transmitted data. When the tags were not touched, the voltages were $0.46 \pm 0.004\ V$ and $0.45 \pm 0.02\ V$ for tags 1 and 2, respectively. During touch events those voltages increased to $0.62 \pm 0.006\ V$ and $0.50 \pm 0.01\ V$ for tags 1 and 2, respectively. These increases and changes of standard deviation were significantly larger than the RFIC's sensitivity of 0.01 V. However, we did observe tag-to-tag variation in the voltage divider. A tag-by-tag calibration of the cap-touch sensor would be required if the read-out system had no learning abilities in order to distinguish between touch and non-touch events.

5.5 Changing ICs

Sections 5.2 through 5.4 used one specific RFIC, the SL900A for demonstration purposes, but this specific chip is not the most appropriate choice for all applications.

Recall that the maximum read range is set in part by the power required by the chip, P_{th}. Different chips can have different read ranges even if the wireless link is identical if one chip has more efficient or sensitive energy harvesting and power management. AMS SL900As were designed for ease of use with a variety of applications and strong wireless connection at low to moderate read range (up to 1 m) but were not designed for long read range. For agricultural application, long read range is critically important, as powered readers will need to come within a read range of a tag in order to collect that data. AS3212 and AS3213 RFID chips, collectively known as AS321X, are specifically designed for long-range passive communications (Asygn, Grenoble, France). For the agricultural sensors project, we switched to using AS321X chips for the longer read range.

The integration process developed for the SL900As provides a blueprint for integrating the new chips. The steps are outlined below and illustrated in figure 5.9.

1. Design screen for I/O pins on the chip
2. Create laser-cut stencil for controlled conductive ink application
3. Mount IC on printed traces and measure mounted impedance
4. Calculate matching network parameters needed to match with 50+j0 Ω antenna
5. Mount IC with antenna and match with passive components around the calculated value. Measure RSSI to confirm optimal matching network component values.
6. Bonus for biodegradable stakes: change antenna geometry for wooden substrate. Print modified antenna on wood, and mount IC and inductor as above.

Because the antenna was designed with $50 + 0j$ Ω impedance, these simple steps are all that is needed to incorporate a new chip. If the antenna had been designed for a specific chip, a full antenna redesign might be required for a new chip. Below, the details of the process are described for the AS321X chip.

First, in figure 5.9a, landing pads with connecting traces were designed according to the pin-out diagram and dimensions of the particular chip. This chip had pads that are 200 μm wide with 200 μm spaces between them. The landing pads, traces to connect to sensor inputs, and the antenna were screen printed. Next, in figure 5.9b, a piece of kapton was laser-cut with the same dimensions as the landing pads. The stencil can alternatively have narrower line widths to reduce total ink volume and therefore ink spreading during chip attachment. The stencil was aligned with the screen printed traces. A pick and place tool was used to place the chip on the wet ink on the landing pads. Figure 5.9c shows the vacuum chuck holding the chip as it came into contact with the substrate. The mounted chip is shown in figure 5.9d.

Next, we measured the impedance of the mounted chip. According to the AS321X data sheet, the RF impedance at the antenna ports is 30-j195 Ω. The mounted measured impedance on a PEN substrate with silver screen printed traces was $22 - j167$ Ω. Figure 5.9e shows a chip mounted on landing pads which were specifically designed for impedance measurement with a VNA. Instead of leading to the antenna, the RF input pins led to an SMA-compatible connection point at the top. For chip impedance measurement, a zero-ohm resistor was used in place of a matching inductor.

The AS321X chip impedance had a large negative imaginary (capacitive) component, which can be offset by a series inductor. The impedance of an inductor is $Z = j\omega L$. For a chip with $-195j$ Ω, an inductor with impedance of $+195j$ Ω at 915

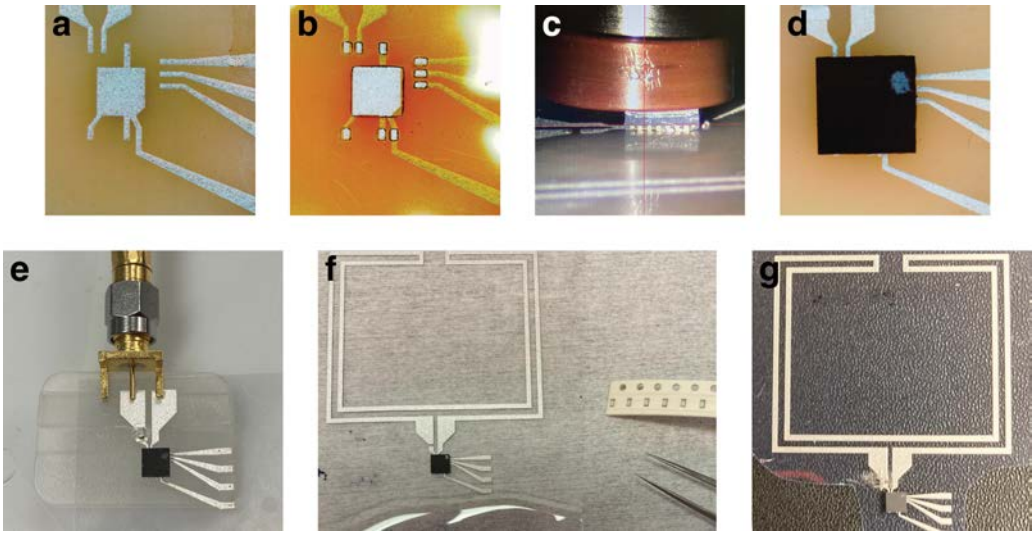

Figure 5.9: a) Landing pads were screen printed with the dimensions of the I/O pins on the chip. b) A new mask for conductive adhesive applications was laser-cut to reflect the physical dimensions of landing-pads. c)A pick-and-place tool is used to align the chip with the wet conductive adhesive on the printed landing pads. d) An overhead view of a mounted chip. e) Measuring the impedance of the chip mounted on printed traces to calculate the appropriate matching circuit. f) Mounting an inductor for impedance matching. g) A complete printed tag with the new chip.

MHz is needed.

$$L = \frac{1}{\mathrm{j}\omega Z} = \frac{1}{2\pi \times 915 \text{ MHz} \times 195\Omega} = 34 \text{ nH}$$

where ω is the angular frequency, $2\pi f$, with f the frequency of 915 MHz.

Figure 5.9f shows a screen printed antenna with a mounted chip ready for a matching inductor to be added. 0603 surface mount components were attached using tweezers and small amounts of conductive ink, allowing different inductor values to be tried with the same chip. Inductor values of 33, 39, 47, and 56 nH were tried on several printed tags, and we used an RFID interrogator system to see which worked the best.

For the AS321X chips, the RFID interrogator set up was made of a different RFID reader system (Speedway R420, Impinj, Seattle, WA, USA) connected to the same circularly polarized RFID reader antenna (MT- 262024/TRH/A/K from MTI Wireless Edge) with 30 dBm output power. RSSI values and number of reads were

collected using the GUI from Impinj, while later sensor readings were collected using Asygn's demonstration GUI for the AS321X chips. The commercial reader was changed from Sargas to Impinj to be compatible with Asygn's GUI.

There was not a clear trend between RSSI at a fixed distance and the inductance used for matching; there are large variations in RSSI for all inductor values. However, tags with 39 and 47 nH inductors tended to have 100's of successful reads per minute, while tags with 56 and 33 nH sometimes struggled to connect. From these observations, 47 nH was chosen for most tags. This suggests that the imaginary part of the chip's impedance was more negative than what was measured or listed in the data sheet. Figure 5.9g shows a screen printed silver folded dipole with a mounted chip and 47 nH inductor which was read reliably.

5.6 Mounting on Biodegradable Materials

The process described in section 5.5 was used to create printed non-biodegradable passive RFID tags with long read range, but a biodegradable version is needed for the agricultural sensor nodes. The raw materials for printed biodegradable RFID tags were developed in chapter 2. Biodegradable antennas which meet RFID performance specifications were demonstrated in chapter 4. We approached integrating these constituent parts to form a full biodegradable RFID tag as a step-by-step process, where each material was replaced one at a time.

First, the PET substrate was swapped for a wax-soaked wood substrate, while keeping the conductor as screen-printed silver ink. This stake is shown in figure 5.10a. The design used an antenna at 82% of original size to be compatible with the wooden substrate. Once the chip and impedance matching inductor were mounted, the stake needed to be encapsulated, but this could not be done by dip coating. Dipping a wax sample into molten wax tends to melt the hard wax and can cause printed traces to warp or the attached components to fall off. Instead, a sheet of Wattman filter paper was pre-cut to shape and soaked in wax, then laid on top of the traces and IC. The waxed paper was adhered to the substrate by locally remelting the wax with a heat gun. This process ensured gravitational and fluid-flow forces did not distort the printed traces while the wax was hot. The encapsulated stake with printed nitrate senors is shown in figure 5.10b. We interrogated this semi-degradable node with the RFID setup for AS321X tags and were able to stream temperature data from 69 cm away, as shown in figure 5.10c. At this distance, RSSI ranged from -62.5 to -56.5 dBm, well above this chip's threshold of -76 dBm.

The next step will be to replace the silver conductor with printed zinc conductor. In this process, we will need to investigate biodegradable conductive adhesive

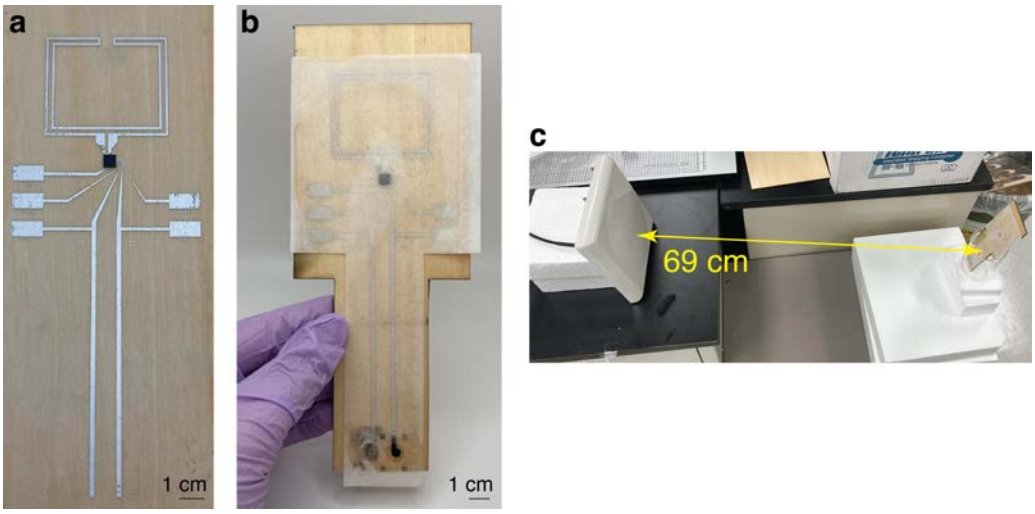

Figure 5.10: a) An AS3212 chip mounted on screen printed silver traces on a wood-and-wax substrate. b) The same printed RFID tag with waxed paper encapsulation. c) Wirelessly reading data from the chip mounted on wood with waxed paper encapsulation.

materials that are compatible with the existing zinc ink, stencil-printable using the laser-cut stencils, and relatively low-loss.

5.7 Nitrate Sensor Integration

The nitrate sensors are potentiometric sensors whose output is a voltage. Although voltage-measurement tools are very common and can be inexpensive, two characteristics of the measurement electronics are particularly important for reading potentiometric ion sensors: the input impedance and the input range.

Input Impedance

When a potentiometic sensor is immersed in a solution containing its primary ion, it generates a voltage. When that sensor is connected to a measurement device, the measurement device acts as a load driven by the voltage generated by the sensor, as illustrated in figure 5.11. In this circuit, the potentiometric sensor is represented by a Thevnin equivalent circuit including intrinsic impedance of the sensor itself, Z_{sensor}. The current that flows depends on the potential of the sensor as well as the

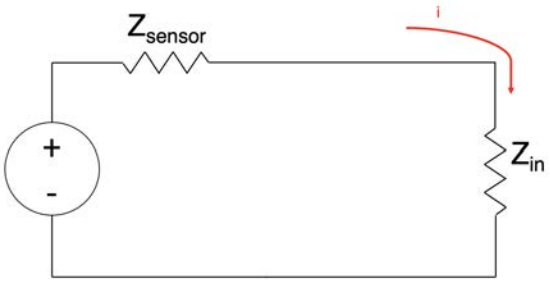

Figure 5.11: The nitrate sensor acts as a voltage source, driving a current through the measurement device.

input impedance, Z_{in} of the measurement device. Accurate and stable measurements require measurement devices with high input impedance to limit voltage dropped across the internal impedance of the sensor and to minimize current flow.

Ion-selective microelectrodes typically have input impedance in the range of $10^{11}\Omega$ and the input impedance of the measurement device should be at least an order of magnitude higher than that of the sensor [146]. We measured the impedance of the gold ISEs with Electrochemical Impedance Spectroscopy on the Ivium Potetiostat and found impedance on the order of 1 MΩ, which is quite low because of the lack of transducer layer.

During sensor optimization and characterisation in the lab, nitrate sensors were measured with four types of analyzers: Keithley 2400 Series SourceMeter, Keysight B2987A Electrometer/High Resistance Meter, an Ivium-n-Stat from Ivium Technologies B.V., and a Campbell Scientific CR1000 data logger. The nominal input impedance of each of these devices is listed in table 5.2. The sensitivity of sensors measured with each of these tools was similar as all had input impedance well above the impedance of the sensors. The different tools did measure different values of E_0. The higher the input impedance, the higher the E_0 value. This trend generally held, though sensor-to-sensor variation was large enough to overwhelm the variation by tool in some cases.

If a tool with insufficient input impedance is used, non-negligible current will flow. For example, a sensor with an electrochemical potential of 300 mV with intrinsic impedance of 1 MΩ being measured by a Data Acquisition System (Keysight DAQ970A) with 10 MΩ input impedance will have $I = \frac{0.3}{10^7} = 30$ nA of current passing through.

Considering the ISE's conductor-membrane interface as a capacitor with capaci-

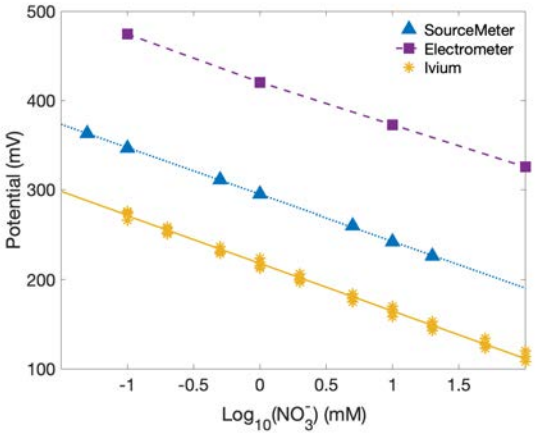

Figure 5.12: Measurement tools with sufficient Z_{in} allow readings of sensors with high sensitivity, but different E_0 depending on the tool.

Instrument	**Input Impedance (Ω)**
SourceMeter	1×10^{10}
Electrometer	1×10^{15}
Ivium Potentiostat	1×10^{12}
CS Datalogger	2×10^{10}
Data Acquisition System	1×10^{7}
Arduino	1×10^{8}
TL082CP OpAmp	1×10^{12}

Table 5.2: Impedance of voltage measurement tools

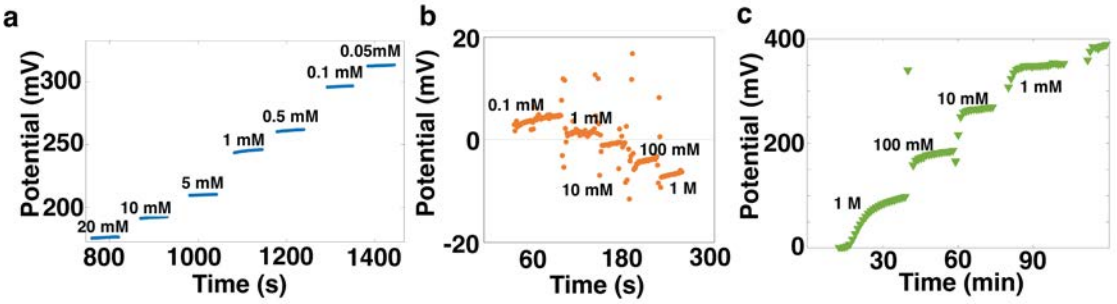

Figure 5.13: a) Nitrate sensor potential over time measured with the Keithly SourceMeter had quick response time and high sensitivity. b) Nitrate sensor potential over time measured with a relatively low-impedance Data Acquisition System had nearly zero sensitivity to nitrate. c) Nitrate sensor potential measured over time with an Arduino board with pre-amplifier circuitry showed high sensitivity and slow response time.

tance of about 3 μF, the voltage drift over time will be

$$\frac{dV}{dt} = \frac{dQ}{dt}\frac{1}{C} = \frac{I}{C} = \frac{30 \text{ nA}}{3\mu\text{F}} = 10mV/sec \tag{5.4}$$

which would lead to drift corresponding to an entire order of magnitude in 5 seconds. In practice, measuring a gold fully printed nitrate sensor with the Data Acquisition System (DAQ) gave the data shown in figure 5.13b. (Figure 5.13a shows the potential over time for a sensor measured with a Keithly SourceMeter for comparison.) With the DAQ, the potential at all concentrations was nearly zero because steady-state conditions were not allowed to develop. An 11 mV change in potential was observed for 5 orders of magnitude change in concentration, for a sensitivity of about -2 mV/dec.

Greenhouse studies of nitrate sensors require at least n=16 for a 4 × 4 Latin square experiment design. To measure this many sensors simultaneously, an affordable readout system was needed well before RFID-enabled stakes were ready for deployment. As an intermediate step, we used wifi-enabled Arduino boards (MKR-1010). These boards have voltage input pins, but their input impedance is only $10^8\Omega$, still too low to measure the sensors. To interface with the Arduino boards, we used a voltage-follower op-amp circuit for each electrode, followed by a differential amplifier to measure the potential difference between the electrodes, as shown in figure 5.14. The op-amps used for these circuits were TL082CP from Texas Instruments, which

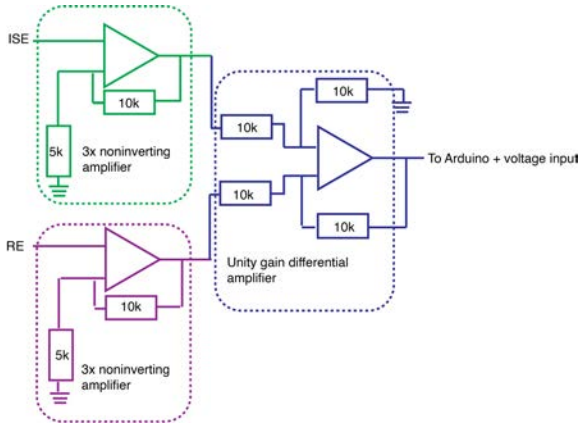

Figure 5.14: A three-part amplifier circuit for interfacing with potentiometric sensors. The ISE and RE are connected directly to op-amp terminals and see the input impedance of the op amp. Choosing op-amps with high impedance allows high-impedance measurement of sensors.

have high input impedance of $10^{12}\Omega$. This circuit used a voltage follower with optional gain for each of the electrodes, followed by a unity-gain differential amplifier. Because the ISE and RE were connected directly to the positive terminals of the op-amps, the impedance they see is that of the op amp. Choosing op-amps with high impedance allows high-impedance measurement of sensors. This circuit was based on considerations described in Fry and Langley [146].

Figure 5.13c shows the potential over time for a fully printed sensor measured with the op-amp circuit/Arduino board combination. The sensitivity for this sensor when measured by the potentiostat was -59 mV/dec. When measured with the Arduino board is was -81 mV/dec, which suggests some impact from the readout circuitry.

The use of external op-amp circuits build around high impedance amplifiers makes relatively low cost reading of potentiometric sensors possible. However, variations in boards, op-amps, discrete resistors used in biasing circuits, solder joints, and wiring from the sensors creates significant node-to-node variation.

Voltage Range

Another important factor to consider when creating field-deployable nodes is the range of potentials expected from the nitrate sensor. Most micro-controller boards

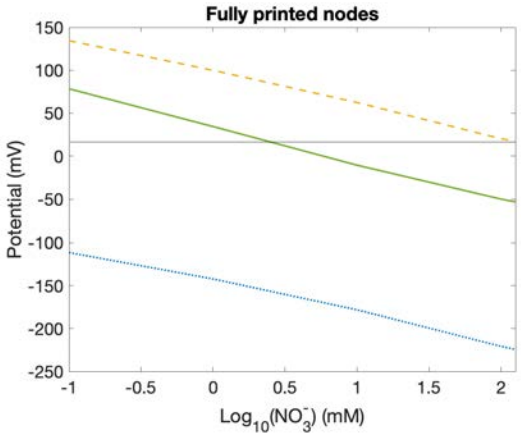

Figure 5.15: Calibration curves for three real potentiometric nitrate sensors. The dashed line is always positive and can be read directly by a circuit with only positive power supply. The dotted line is always negative and can be connected with reverse polarity to be read by a circuit with only positive power supply. The solid line crosses zero and cannot be read by a circuit with only positive power supply.

have on board power ranging from zero to $+V_{DD}$, which might be +3.3V or +5V depending on the board. If the ISE potential is consistently more positive than the RD potential, as for the dashed line in figure 5.15, the sensor can be directly read by the micro-controller. However, on-board amplifiers and digital to analog converters cannot take negative input voltages. If the ISE potential is consistently more negative than the RE, as for the dotted line in figure 5.15 the two electrodes can be plugged into the opposite terminals, effectively multiplying the response by (-1). These sensor nodes will have a positive slope with respect to nitrate concentration, which can be confusing for partners involved in field testing if the situation is not clearly explained.

If the nitrate sensor's potential is above zero for low nitrate concentrations and below zero for high nitrate concentrations, as for the solid line in figure 5.15, the sensor cannot be read by a circuit without a negative voltage on the power supply. Its signal will rail out for either high or low nitrate concentrations.

Whether a sensor's output potential at moderate nitrate concentrations is positive, negative, or near zero depends on the E_0 of the sensor and connecting wires. The large variation in E_0 leads to sensors with all three scenarios. Reducing E_0 variation would be helpful for designing reliable and user-friendly interface electronics.

Outlook for Nitrate Sensor Nodes

Commercial off-the-shelf RFID tags generally do not have voltage input pins with sufficiently high Z_{in} or a wide range of accepted input voltages. The input voltage range issue can be managed by creating sensors with reproducible E_0, which is a task for sensor research and optimization. Sufficient Z_{in} requires custom IC design. Both of these issues must be addressed to integrate potentiometric sensors with RFID tags.

5.8 Conclusion

Once discrete components have been independently optimized, building complete, functional systems with them is not a trivial task. Connections between different types of materials, such as flexible-to-rigid, printed-to-silicon, or biodegradable-to-nondegradable, require consideration of material properties. Connections between different parts of RF systems require impedance matching. Connections between sensors and ICs or micro-controllers require attention to input pin specifications and sensor requirements.

Here we have demonstrated integration of printed electronics with commercial off-the-shelf RFICs with a process that is adaptable for different models of RFICs. This process was used to connect RFICs to printed capacitive sensors, and data from printed sensors was communicated wirelessly. Integrating the RF-side with potentiometric ion sensors requires specific I/O interfacing with the electronics. Intermediate sensor nodes were used to demonstrate initial integration of printed nitrate sensors with readout electronics, and highlighted impedance and voltage range requirements for electronic interfacing on fully integrated nodes to come.

Chapter 6

Field Deployment

Scientific and engineering laboratories are designed to be carefully controlled spaces, where the scientific method is possible. All variables are held constant save for the ones which are the subject of the study. In these conditions, biodegradable conductors and substrates, nitrate sensors, antennas, and RFID tags meet performance specifications.

Agricultural conditions are not like engineering laboratories. They are subject to variable and sometimes extreme weather, pests from microbial scale to rodents, changing soil biochemistry, and impacts of growing plants. Before sending our sensor nodes to a field used in commercial scale agriculture, we need to study, in a semi-controlled way, the impact of real soil and growing crops on the individual parts of a sensor node. In this chapter, we examine the degradation of wooden stakes in a greenhouse and the effectiveness of beeswax as an encapsulation material. We study the performance of nitrate sensors in three types of soil at various water contents. Finally, we look at the impact of wet soil and crop canopies on passive RFID wireless links.

6.1 Stake Materials

The stake and encapsulation are responsible for the physical structure and protection of the functional electronics. It is important to understand the lifetime and degradation of these materials in field conditions. If the encapsulation fails before the desired functional lifetime, there is little chance that the electronics will survive.

To test the lifetime of the stake materials and the effectiveness of beeswax as an encapsulant, we planted wax-coated and bare wooden stakes in pots with growing corn and lettuce in a greenhouse and left them for 90 days.

Figure 6.1: a) Stake design including three interlocking wood pieces with a flat top supported by a back bracing piece. b) Wax dripping marks and holes from air bubbles are visible on hand-dipped stakes. c) Four dipped stake ready for planting. d) Stakes planted to 6 inch depth in soil media.

Materials and Methods

Twenty-four stakes were tested, twelve of bass wood (3 ply, 3 mm thick) and twelve of balsa wood (single ply, 3 mm thick). The pieces of the stakes were laser cut, then the stakes assembled using Elmer's craft glue (applied with a fingertip) and left to dry for at least an hour. Figure 6.1a shows the stake design of three interlocking pieces.

Beeswax (unfiltered cosmetic grade beeswax, GloryBee, Eugene Or, G0142306) was melted in a crock pot on high to a depth of 11.5 cm. Eight of each type of stake were dip coated in the melted wax. The stakes were taller than the depth of the wax, so both ends had to be sequentially dipped. Each end received two coats of wax, and a section about an inch wide in the middle of the stakes got a total of four coats. Stakes cooled fully between coats. Figure 6.1c shows four of the finished,

Table 6.1: Mass loss of wood stakes after 90 days

Wood	Encapsulation	Mass loss as percent of starting mass
Balsa	no wax	39%
Balsa	beeswax	1%
Bass	no wax	14%
Bass	beeswax	3%

coated stakes.

Handcrafting encapsulation like this leads to nonuniformities. In particular, wax dripping while setting leads to uneven thickness. Additionally, because wood is porous, it has air bubbles in it. These can create pinholes in the wax when dipped. The second coat of wax helps mitigate the pinholes in the bulk of the wood. The seams of the plywood in particular trap air which causes higher concentrations of pinholes on the edges of the 3-ply bass stakes, as shown in figure 6.1b.

The soil used in this study was a 1:1 mixture of sand and a Turner Loam silty top soil described in more detail in section 6.3.

Uncoated and coated stakes were partially buried along with corn seedlings in 16 pots of soil which were exposed to greenhouse temperatures ranging from 18 to 22°C . Figure 6.1d shows the planted stakes at the start of the study. An additional set of coated stakes were tested in a growth chamber simulating early spring or late fall conditions (20°C days and 10°C nights) with lettuce to study the impact of day/night cycling of temperature on the wax. All pots were irrigated along with the addition of nitrogen fertilizer.

Within three weeks, no above ground deterioration was observed for uncoated balsa stakes and all wax coated stakes, shown in figure 6.2a,b. Wax-coated stakes were hydrophbic, so water beaded on their surfaces, as shown in figure 6.2c, while uncoated bass plywood absorbed water, and repeated watering and drying led to significant delamination, shown in figures 6.2d-e.

After 39 days, a single uncoated bass wood stake was removed from the ground for visual inspection and white mold growth was noted. After 90 days, all stakes were carefully removed, visually inspected, and remains were washed, dried, and weighed. Figure 6.3 shows remains of a representative sample of each type. The average mass loss of each sample type is shown in table 6.1.

Below ground portions of all uncoated balsa stakes were nearly completely degraded therefore contributing to the drastic reduction in mass. Although bass wood is considered to have low resistance to microbial attack [147], our samples showed

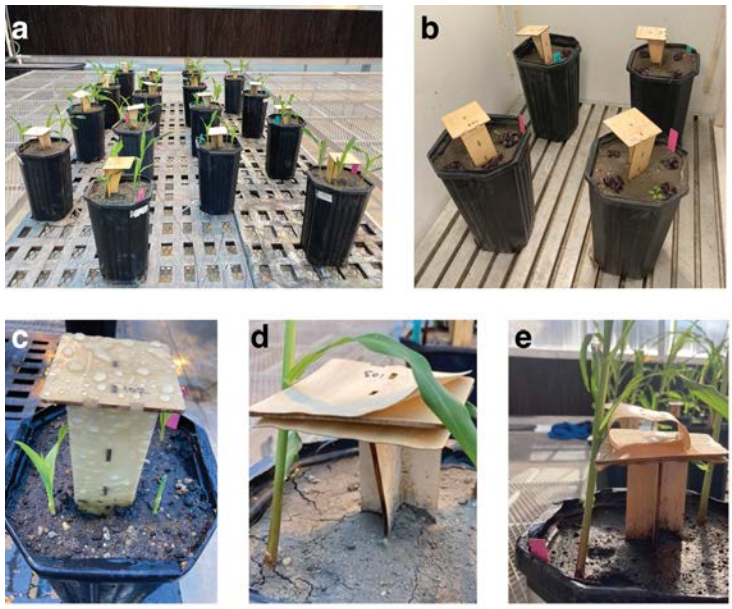

Figure 6.2: a) 16 pots with coated and uncoated bass and balsa wood stakes with corn growing in the greenhouse. b) 4 of the 8 wax-coated stakes with lettuce plants growing in the growth chamber. c) A wax-coated bass plywood sample is hydrophobic, so irrigation water beads up on the surface. d) An uncoated bass plywood sample absorbs water and the plies swell at different rates, leading to delamination. d) Complete delamination of the top ply of uncoated bass plywood.

very little degradation in terms of mass loss. This could be attributed to several factors including adhesives or simply insufficient time to degradation. All wax-coated samples had very little mass loss, showing the usefulness of beeswax as an encapsulation layer to prevent degradation in soil. The wax coated 3-ply bass wood samples split along the joints between plies when they were dried after removal and before weighing. This happened because water seeped in through the pinholes at the seams, and further highlights the need for a complete wax seal without pinholes. While this experiment showed the utility of beeswax as a protective encapsulant for structural members of sensor nodes, it reinforces the advantages of balsa wood for biodegradable sensors, as it remains structurally sound when encapsulated but rapidly degrades when exposed to soil.

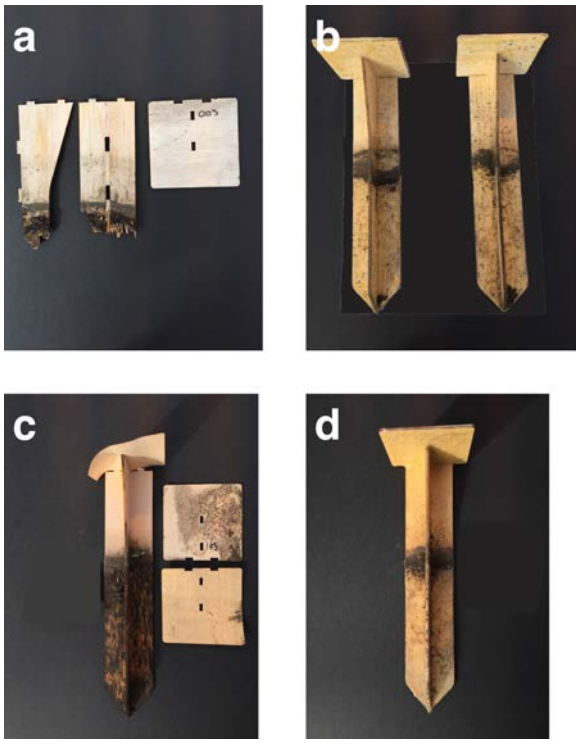

Figure 6.3: a)Balsa wood without wax encapsulation decomposed under the soil surface in 90 days. b) Balsa wood with beeswax encapsulation layer did not degrade. c) 3-ply bass wood delaminated above the soil level and began to decompose under the soil level. d) 3-ply bass wood with beeswax encapsulation did not degrade.

6.2 Nitrate Sensors in Soil

Soil Texture and Moisture

Soils are complex environments with many characteristics that could complicate potentiometric nitrate sensor readings. Although the sensors were shown to have high sensitivity to nitrate and be largely insensitive to most other ions commonly found in soil in chapter 3, soil is more complicated than aqueous solutions. Soils have different textures, water content, pH, electrical conductivity, cation exchange capacity, and organic matter content, to name a few. Ideally, nitrate sensors should not be sensitive to any of these soil properties, but calibration or direct measurement of the interfering property could help return accurate nitrate measurement values.

In order to tell which soil properties influence our printed potentiometric nitrate sensors, controlled studies are needed for each property. We begin with soil texture and moisture content.

Methods

A set of 20 nitrate sensors were prepared. Ion selective electrodes and reference electrodes were printed separately as described in chapter 3. Individual electrodes were attached to an acrylic stake with tape and wires were connected using 8331D silver conductive epoxy (MG Chemicals, Burlington, ON, Canada), and encapsulated by Gorilla epoxy. The wires were routed to a board consisting of the pre-amplifier circuitry for high input impedance described in section 5.7 and a wifi-enabled Arduino MKR1010 board. A finished stake is shown in figure 6.4a. Each sensor remained paired with its specific readout electronics for all the tests.

Two types of tests were done. In the nitrate sensitivity tests, aqueous solutions with concentrations of nitrate between 0.1-1000 mM were used to saturate an array of containers with either sand, clay, or peat soils. Figure 6.4b shows sensors being measured in sand. Sensors were left in one container for at least 5 minutes while the Arduino recorded the sensor's output potential, then moved to the next container.

Sand tests were performed with a commercially available desert sand (Mosser Lee, Milston, WI), consisting of only sand-sized soil particles and no initial nitrate. Clay tests were performed with an agricultural clay soil utilized for perennial alfalfa (Medicago sativa) and the peat soil is agricultural peat soil; both clay and peat are from Bouldin Island in the Sacramento–San Joaquin Delta, California, and are described in more detail by Anthony et al [103].

In the moisture tests, another array of containers with the three soil types were prepared. This time, all containers were watered with 10 mM nitrate solution, but to different moisture levels. Moisture levels included 0, 10, 20, 30, 40 and 50% and again sensors were left in one container for at least 5 minutes while potential was measured, then moved to the next container.

Nitrate in Sand

Sand has low cation exchange capacity, so few other ionic species are present, and the solids in the soil itself are unlikely to interfere with the potentiometric measurement. Nitrate sensors in sand showed strong linear relationships between nitrate concentration and output voltage, with about half of the 17 sensors included in this trial showing R^2 values above 0.99. These 8 sensors with $R^2 > 0.99$ were used for the remaining analysis. The high R^2 values indicate that these sensors were indeed

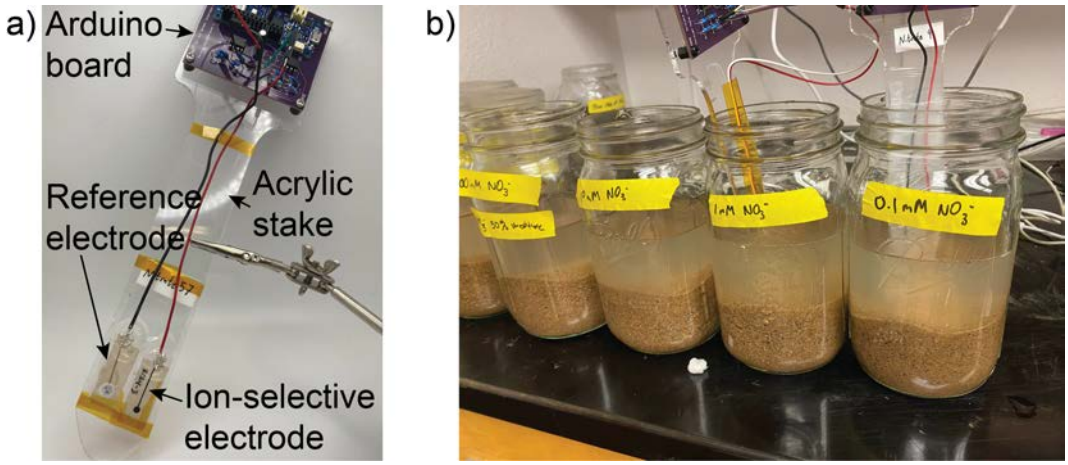

Figure 6.4: a) A printed nitrate sensor attached to a wifi-enabled Arduino board and associated voltage-measuring electronics. b) A set of containers with sand and varying nitrate concentrations are used to measure sensitivity of the sensor nodes in sand.

sensing nitrate and, once calibrated, they could be used to find an unknown nitrate concentration from a measured potential. The average sensitivity for these sensors was -42 ± 8 mV/dec. Figure 6.5a shows the linear relationship between nitrate concentration and output potential for five of the sensors in sand, with sensitivities ranging from -40 to -42 mV/dec. Sensitivities between -40 and -50 mV/dec are considered acceptable at this development stage.

There is a significant variation in E_0, which is shown in figure 6.5a by the vertical space between each sensor's calibration fit line. The standard deviation of the intercepts of the best fit lines is 270 mV, and the range was 648 mV (n=8). For comparison, gold nitrate ISEs measured with a potentiostat in aqueous solution had E_0 variation of about 80 mV. The significantly higher E_0 variation here could be partly due to inconsistencies in contact between the liquid in soil and the electrode surface, but the Arduino electronics used to measure the sensors also introduce substantial variation. A small study of n=4 nitrate sensors measured with a Campbell scientific data logger in sand with varying nitrate had E_0 variation of 90 mV.

Nitrate in Peat

Figure 6.5b show the output potential of three nitrate sensors measured with Arduino boards in peat soil at varying nitrate levels. They had sensitivity of -31 ± 8 mV/dec,

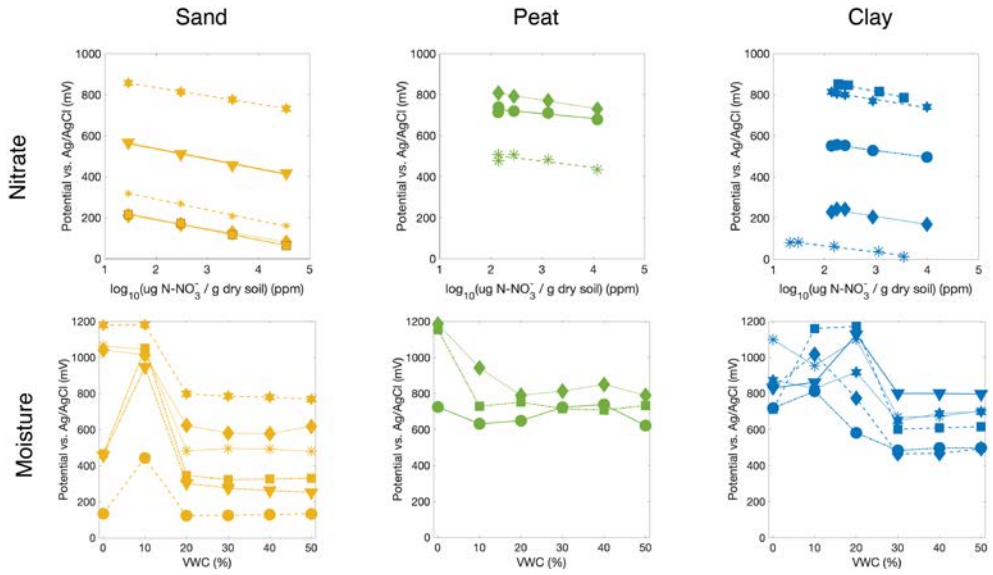

Figure 6.5: a) Nitrate sensitivity in sand. b) Nitrate sensitivity in peat. c) Nitrate sensitivity in clay. d) Impact of moisture content in sand. e) Impact of moisture content in peat. f) Impact of moisture content in clay.

with R^2 values for each sensor's best fit line of 0.8, 0.71, and 0.99. The standard deviation of the intercepts of the best fit lines was 165 mV. The low sensitivities and relatively low R^2 values are due to inconsistencies with Arduino boards and the age of the sensors. These sensors were measured in sand and clay first, before the measurements in peat, so by the time of these measurements, the sensors had been inserted, removed, and rinsed from soil media many times. Figure 3.8c and section 3.7 described fresh nitrate sensors in peat soil measured with a Campbell Scientific data logger. Under these conditions, the sensitivity was -47 mV/dec, R^2=0.95, and E_0 variation 30 mV (n=3).

The different results depending on the age of the sensor and the electronics used to measure it highlight the importance of improved stability for real-world use cases.

Nitrate in Clay

In clay, five of 14 sensors had R^2 values >0.9 and slopes between -30 and -60 mV/dec; these sensors' relationships between measured potential and nitrate concentration are shown in figure 6.5c. The sensitivity of the sensors was -39± 8 mV/dec, and the variation in intercepts of the sensors' best fit lines was 360 mV. Clay has much

finer grain size and higher cation exchange capacity than sand, so it is notable that sensitivity values and the standard deviation of intercepts are similar for sensors measured in sand and clay. This suggests that soil texture alone is not a primary interfering factor in soil nitrate measurements, though other soil characteristics may be.

Moisture Content

Ideally, nitrate sensors' output should not depend on soil moisture content. However, potentiometric sensors require electrochemical contact between the two electrodes to function: ions must be able to move from the ionophore membrane in and out of the same solution that is in contact with the reference membrane. At some point, the soil becomes too dry to support this flow of ions, and the electrodes become effectively an open circuit, providing no useful signal. To identify the minimum moisture level for effective sensor operation, the output potential was measured for soil samples of varying moisture content, all watered with 10 mM nitrate solution.

The results are shown in figure 6.5d-f. Sand and clay soils followed the expected pattern. Above a certain threshold, output potential was constant with respect to moisture content, represented by the flat lines on the right-hand side of figures d and f. The potential jumped significantly and abruptly at low moisture content. These read-out electronics defaulted to high signal output at open-circuit inputs. For sand, the threshold was between 10 and 20% volumetric water content (VWC). For clay, it was between 20-30%. This makes sense because clay's matrix potential is higher than that of sand, meaning water is bound more tightly to the surfaces of solid particles in clay. When this happens, water is not free to move about and cannot provide a path for ions to equilibrate between the sensor's ISE and RE. The relationship between water content and sensor signal output in peat soil was not as clear. The minimum water threshold seemed to be between 10-20%, but the output potential was not as stable between 30-50% VWC as it was in other types of soil. Different sensors have different minimum thresholds. It was unclear if these results were due to variations in water retention properties of the high-organic matter soil, or resulted from drift and damage to heavily-used sensors, as discussed for the peat-nitrate results.

Individual Sensor Characteristics

Throughout the results from sand, clay, and peat in both nitrate and moisture tests, there was significant sensor-to-sensor variability. Here, I show that most of that has to do with the sensors, not the soil.

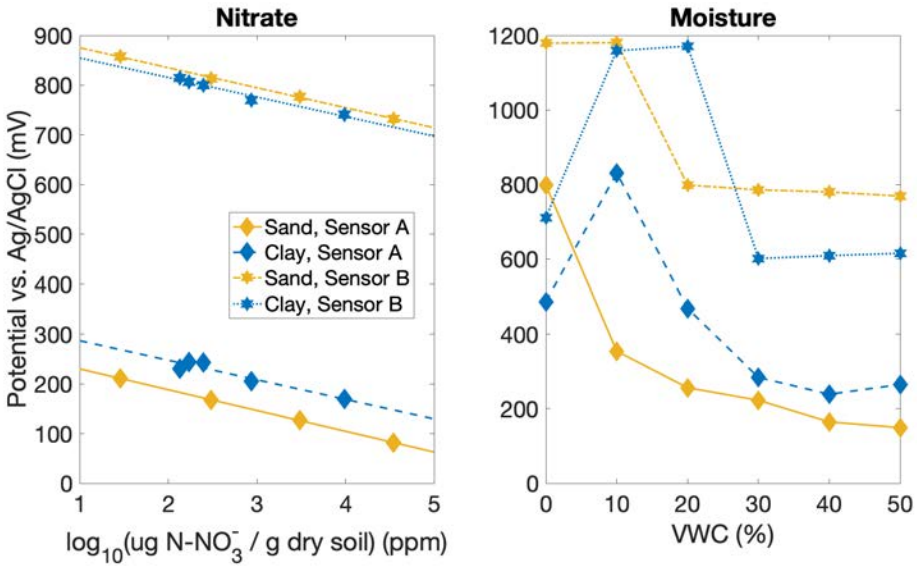

Figure 6.6: Output Potentials for two sensors in sand and clay for nitrate tests and moisture tests. Sample A, in diamonds, consistently outputs between 100-300 mV when it is functioning correctly, regardless of soil type or test type. Sensor B, in stars, outputs 600-900 mV. The variation seen in figure 6.5 can be traced to indiviual sensor tendancies like this.

Subsets of the same 20 sensors were used in all six measurements. Sensors which had low R^2 in sand also had low R^2 in clay, while most sensors with high R^2 in sand also had high R^2 in clay (70%). Sensors which performed better in sand than clay may have suffered use and aging impacts. Similarly, sensors with relatively high potential outputs had this characteristic across soil types and nitrate/moisture measurements. For example, figure 6.6 shows nitrate content and moisture sweeps for two sensors in sand and clay. In all cases, sensor A, represented by diamonds, has much lower potential than sensor B, represented by stars. The potential measured by sensors during the 50% moisture and 10 mM concentration point of the moisture sweep was within 50 mV of the potential measured during the 10 mM point of the nitrate sweep for half of the sensors measured in sand.

Sensor-to-sensor variation is a problem that needs to be solved in order to avoid mandatory calibration of every individual sensor. This variation stems mainly from the sensors and readout electronics themselves, not from the type of soil. Sensors are relatively stable from measurement to measurement, which took place over a period

of a few days to a week for most sensors.

6.3 RFID Read Range

As discussed in section 1.3 and 5.3, RFID technology enables communication with fully passive nodes like our biodegradable nitrate sensors. The price for making a battery-free sensor node is limited read range, because the power for the sensor measurement and data communication comes from the interrogator antenna and is subject to propagation losses as it travels the distance to the tag. Because power diminishes as $\frac{1}{R^2}$, doubling the distance reduces power received by the tag by 75%. Battery-less RFID typically supports reading distances between 1-10 m, which is significantly less than the kilometer read ranges possible with powered cell technology. However, UHF-RFID read ranges are considerably greater than HF RFID, or near field coupling (NFC), which operate on the order of a few centimeters. In agricultural settings, the presence of soil and plants can further limit the read range.

Several studies have looked into passive RFID communications in soil. Bauer-Reich studied tags buried 5-20 cm deep in silty loam soil at different water contents [148]. Frolik characterized communication with tags buried up to 50 cm deep by frequency, soil depth, moisture, density, and texture [149]. Bogena et al. compared mathematical models for path losses in soil to measurements [150]. In all cases, wetter soil reduces the power received. This is because the dielectric properties of soil depend on soil moisture. The complex permittivity $\epsilon = \epsilon' + j\epsilon''$ of soil varies widely: the real part of the permittivity, sometimes known as the dielectric constant, ϵ', ranges from about 5 in dry soil to 30 in wet or dense soil at 1.4 GHz [151]. The change in ϵ' shifts the resonance frequency of the buried antenna, making it less efficient. For example, a dipole antenna designed to operate at 915 MHz buried in dry soil with $\epsilon' = 5$ will resonate at 409 MHz, and at 183 MHz in a wet soil whose ϵ' is 25. Additionally, attenuation from propagation in lossy media (represented ϵ'') by hampers communication to RFID tags which are buried underground at sensor level. For example, a 915 MHz electromagnetic wave propagating in a materials with $\epsilon = 25 + j6$, which represents a wet silt loam, will lose half of its power after traveling only 3 cm.

Because changing soil moisture changes the dielectric properties of soil, which in turn impacts the received signal strength in a wireless system, the signal strength itself can be used to monitor soil moisture conditions. For example, reduction of signal strength of a sensor at a known depth has been used as an indicator for increased soil moisture in pots [152] while Azar et al. kept the antenna above ground but used a probe inserted into the soil to detune the antenna and reduce signal

strength [120]. While changing RF conditions related to moisture can be useful when measuring moisture, they remain problematic for sensors that measure any other properties. For example, a nitrate sensor tag completely buried in wet soil might be unable to transmit its data, rendering the sensor useless until the soil dries, at which point the electrochemical sensor will not be operational.

One way to improve signal strength is to bring the antenna to the soil surface. This reduces attenuation from propagation in lossy media, but does not eliminate the loading of the antenna by highly variable permittivity soil near the antenna. Raising the antenna slightly above the soil surface helps mitigate this second problem. Figure 1a illustrates what a passive node with below-ground sensors and above-ground communication might look like.

The goal of this work is to characterize the feasibility of passive RFID communication in agriculture. The primary metric of interest is maximum read range because in order to take a measurement, a powered reader needs to be within the read range of a sensor node—the shorter the read range, the closer the reader has to be to the tag to get data.

In practice, the powered reader would be mounted on mobile infrastructure of some sort and would travel around the field to collect data from dispersed tags. The reader could be mounted in a variety of ways. Three examples are shown in figure 6.7. Readers could be mounted on existing infrastructure like center pivot irrigation systems; on drones (which might also capture optical remote sensing data) programmed to fly a specific pattern; or on tractors with wide booms like sprayers.

To make a system like this reasonable to implement, a reader height well above the height of the plants, and similar to the height of existing equipment is needed. This might be in the range of 1-4 m, depending on crop type.

In addition to soil impacts, wireless communication in agricultural settings must overcome the challenge of crops in the signal path. Leaves and stems can block the line-of-sight between the reader and the tag, causing reflections and scattering losses. The extent of the scattering depends on the leaf size and density, crop type, and the position of the tags relative to the rows of plants. The impact of crop canopy on wireless links between two powered nodes at the same height above the ground with some horizontal distance between them has been studied in wheat, corn, and vineyards [153, 154, 155]. However, the impact of crop canopy on communication between a ground level node and an elevated node has not been well documented in the literature.

Here, the vertical read range for passive RFID tags at 915 MHz as a function of soil texture, soil moisture, and presence and type of crop canopy is characterized. High water content soils significantly limit read ranges, but adding space between the tag and the soil surface mitigates the losses. While crop canopies reduce read

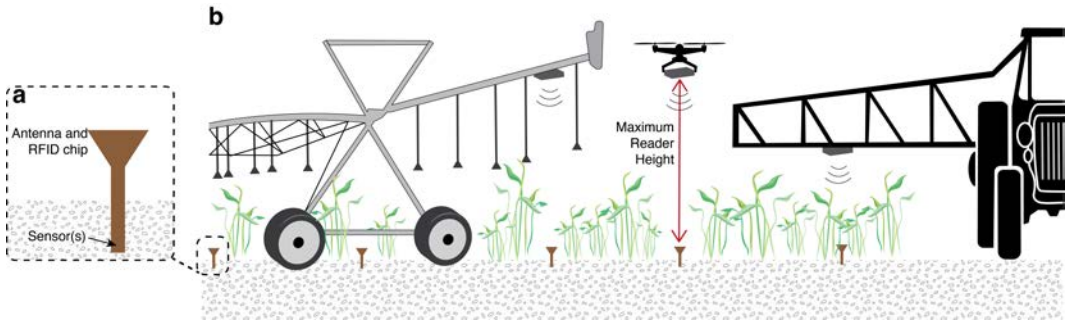

Figure 6.7: a) A passive soil sensor node consists of a subsurface sensor or sensors connected by a conductive trace to an above ground RFID chip and antenna. b) Passive soil sensor nodes which are widely distributed through a field could be read by powered readers mounted on existing farm infrastructure such as center pivot irrigation systems, aerial drones, or tractors with wide booms as for spraying. However the reader is mounted, the wireless link is primarily vertical—with the reader above the passive node. The crop canopy might or might not impede direct line of sight depending on the specific placement of sensors within or between rows.

range, ranges of more than 1.5 m are still possible even with dense canopy. These results lay the foundation for the deployment of a system of 100's of battery-free sensors in agricultural settings.

Materials and Methods

Reader, antenna, and tags

The RFID tags were read using a commercially available RFID reader system (Thingmagic Sargas, Trimble, Sunnyvale, CA, USA) connected to a circularly polarized RFID reader antenna (MT- 262024/TRH/A/K from MTI Wireless Edge) with 30 dBm output power. The passive tags were Asygn AS3123 demo tags (Asygn, Grenoble, France).

Soil Preparation and Details

Five types of soil were used in these tests: a sand, a Turner series silty loam top soil, a 1:1 mix by volume of Turner loam and sand, a 1:1:1 mix by volume of peat moss, Turner loam, and sand, and a Farnuf series soil with high-clay content. The dry bulk density, ρ, of each soil type was calculated by weighing soil samples after drying in

Table 6.2: Soil density and water holding characteristics

Soil type	Dry bulk density $g/(cm^3)$	Saturation GWC g/g	Saturation VWC $(cm^3)/(cm^3)$
Farnuf Clay Soil	0.85	38.4	32.6
Turner Loam soil	0.75	48	36
1:1:1 Sand: Turner: Peat	0.77	47	36.2
1:1 Sand: Turner	0.98	28.1	27.5
Sand	1.2	20	24

an oven at 118°F and 8% relative humidity for a few days. Saturation was found by watering the pots until a layer of standing water collected above the soil surface and water dripped out the bottoms of the pots, then waiting until the dripping stopped; this is the holding capacity of the soil. Water content was calculated by both mass and volume. Gravimetric water content, or GWC, is defined as $\frac{\text{mass water}}{\text{mass dry soil}}$. Volumetric water content is defined as $\frac{\text{volume water}}{\text{total soil volume}}$, which can also be found as GWC $\times \frac{\text{dry bulk density}}{\text{density of water}}$.

Table 6.2 shows the dry bulk density, and saturation water content by mass and volume for each soil type. Each day that RFID measurements were taken, each pot was weighed. The mass was used to find VWC and GWC for each soil type each day.

Read Range Measurements

An adjustable wooden stand was constructed to measure the read range. The interrogator antenna was attached to an arm which extended 70 cm away from the vertical support piece. The vertical attachment position of the arm could be fixed by sliding pegs on the arm into a series of evenly spaced holes in the vertical support. The height of the vertical support could also be increased to achieve interrogator antenna heights higher than arm's reach. The stand is illustrated in figure 6.8.

The height of the interrogator antenna was raised until no signal was received from the tag, then lowered in 5 cm intervals until the tag was found again. The height of the interrogator antenna above the surface of the soil in the pot was recorded as the read range. The tags were placed parallel to the surface of the ground. Their height above the ground was controlled by placing zero, one, or two 1.7 cm thick Styrofoam blocks between the soil and the tag.

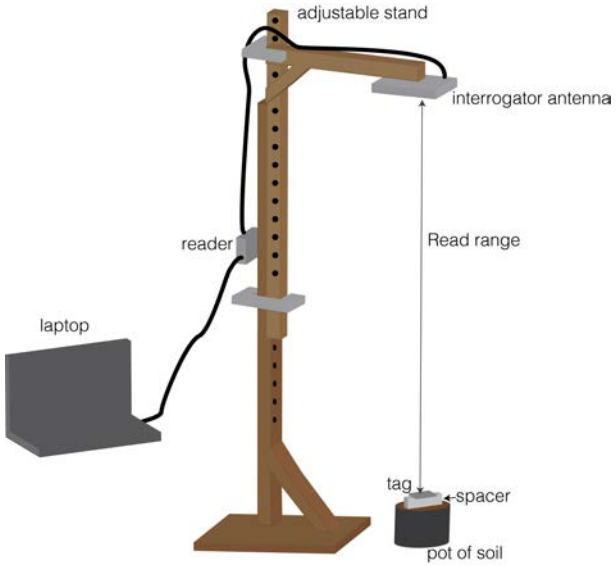

Figure 6.8: Read range measurement set up.

Crop Canopy Read Range

To measure read range in crops, a ladder was set up near the edge of each plot. The interrogator antenna, attached to its wooden extended arm, was taken up the ladder until the signal from the tag on the ground was lost, then lowered again until the signal was found again. The height of the antenna was measured with a measuring tape.

Results and Discussion

The maximum read range, r_{max}, of an RFID system is given by equation 6.1

$$r_{max} = \frac{\lambda}{4\pi}\sqrt{\frac{G_T G_R P_T m_{pol} \tau}{P_{th}}} \tag{6.1}$$

Where λ is the wavelength in free space, G_T and G_R are the gains of the transmit and receive antenna respectively, P_T is the power transmitted by the reader, m_{pol} is the polarization mismatch factor, τ power transfer coefficient, and P_{th} is minimum power required by tag. During a reading, EM waves propagate first from reader to tag, then from tag to reader. In both directions, the channel includes losses from free space propagation governed by the Friis equation, scattering off crops, and soil

impacts. Because most powered readers are highly sensitive and can receive even weak responses, the limiting direction for backscattered systems is typically reader-to-tag. The tag must receive at least a threshold power, which is a parameter set by the circuits in the IC.

The polarization mismatch m_{pol} refers to power lost because of polarization differences between the reader antenna and tag antenna. The tag antenna is a modified dipole, which has a primarily linear polarization. The reader is circularly polarized, so the polarization mismatch should always be 0.5 (or half the power is lost) regardless of the orientation of the tag. To verify this, the power received from the tags was measured for tags at four different polarization angles for reading distances of 60 cm. Four conditions were tested: tags on soil without crop canopy and no space between tag and soil; tags on soil without crop canopy and 1.7 cm space between tag and soil; tags under corn canopy with no space; and tags under corn canopy with 1.7 cm space. In all conditions, the power received from the tag did not depend on the polarization angle of the tag.

Field Test: Soil Moisture

In order to quantify the impact of soil texture and moisture on read range, pots of five different soil types were prepared: a high clay content soil, a silty loam top soil, sand, a 1:1 mix of sand and silty loam top soil, and a 1:1:1 mix of sand, silty loam topsoil, and peat. The details of these soils are described in the methods section. The maximum read high was measured for tags placed on the surface, 1.7 cm, and 3.4 cm above the soil on three different days. The maximum height of the stand was 2.78 m, so the maximum read range in some cases, especially the 3.4 cm spacing with drier soil, is likely higher than that. Each day the soil water content was measured. Figure 6.9 shows the maximum read range for each soil type and moisture level.

One key finding was that for any soil type, lower soil moisture corresponded to greater read range, which was expected because dryer soil has a dielectric constant more like free space than wet soil does. The increase in read range without a block was most pronounced in the sand, where the driest condition had a read range 56% higher than the wettest, and least pronounced in the soil/sand/peat mixture, where read range only increased 23%. This was likely related to the way the soils dry. The sand was porous and dried out quickly. The pure soils were not designed for use in pots, and the top dried out more quickly than the bottom. The soil/sand/peat mixture was specifically mixed to be a good growing media for pots in a greenhouse: the sand helped with drainage while the peat held onto water, so the soil dried the most uniformly.

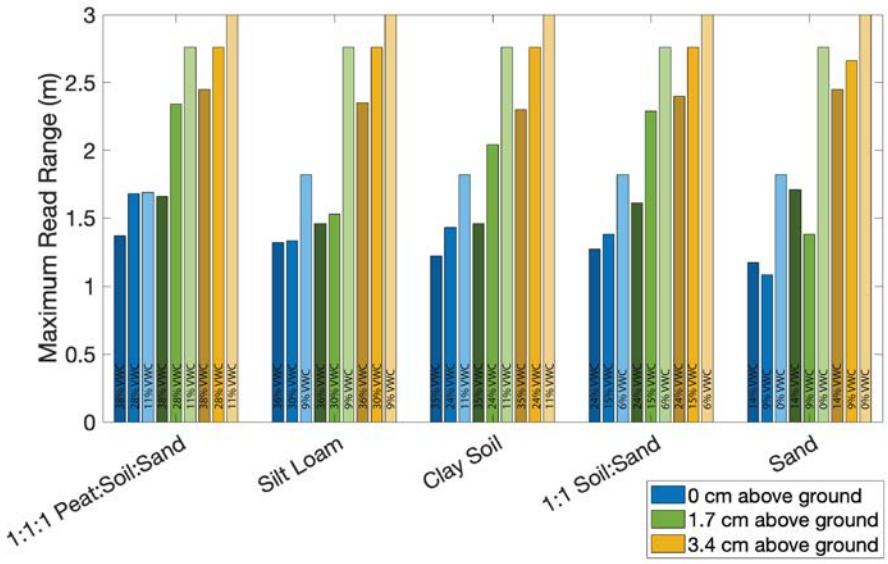

Figure 6.9: Maximum measured read range for five types of soil, three wetness levels, and three tag-soil distances.

Another key result was that for all soils, and all moisture levels, adding space between the tag and the soil surface increased read range. This was because the soil loaded the antenna, shifting its resonance out of the band of interest, but adding space reduced the loading. For the saturated conditions, adding 1.7 cm of distance helped the most in sand, where read range increased by 46% as a result. The 1.7 cm of distance had the smallest impact on the silt loam soil, where read range only increased by 11%. Adding 3.4 cm of space more than doubled the read range in sand compared to zero space; in silt loam soil, the read range increased by 78%. Part of the reason for this is that the read range for saturated sand was the lowest of any of the conditions. Sand had the highest density, and, for a given volumetric moisture content, sandier soils have a higher dielectric constant than finer textured soils [151]. Therefore, wet sand significantly limited read range, and anything to mitigate that impact—drying the sand or adding space—offered a proportionally larger benefit.

One way to understand the phenomena of adding spacers is to look at fundamental electromagnetic wave propagation while modeling the soil as a reflecting ground plane. This is not strictly accurate as the soil is not a conducting material, but from EM theory, the interface between two insulators with different dielectric constants

causes reflection of EM waves [109]. Here, the junction of air and wet soil with a dielectric constant of 25 will lead to

$$\frac{\epsilon' - 1}{\epsilon' + 1}^2 = \frac{25 - 1}{25 = 1}^2 = 0.92 \tag{6.2}$$

or 92% of the power reflected. The high degree of reflection at the air-soil boundary justifies modeling it as a ground plane. From antenna theory, the spacing between the antenna and the ground plane should ideally be $\frac{\lambda}{4} = 8.2cm$, so that waves reflecting off the ground plane constructively interfere with initial radiation, after accounting for the $\frac{\pi}{2}$ phase shift from the reflection at the boundary.

Simulations of linear dipoles in HFSS can be used to more fully understand the impact of a nearby ground plane on the antenna. The $|S11|$ for a half wavelength dipole modeled by a cylindrical wire 0.5 mm wide and 153 mm long with a 1 mm feed gap was -15.3 dB at 915 MHz in free space, -0.0 with a conducting plane 1 mm away, -2.0 with a conducting plane 1.7 cm away, -7.1 with it 3.4 cm away, and -9.7 with it 8.2 cm—a quarter wavelength—away. This theory indicates that increasing the distance between the soil and the tag to 8.2 cm could improve read range or signal strength even more. An antenna 8.2 cm above the ground might or might not be practical for field deployment, as it could be more intrusive, and would require longer traces to connect to sub-surface sensors. Optimal antenna height/stake lengths become an application-specific optimization problem.

Field Test: Crop Canopy

In the final set of experiments, tags were placed under growing crops and the maximum read range was measured. The read range for the different crop types is shown in figure 6.10. In each case, tags were measured directly on the soil surface and with 1.7 cm of distance between the tag and the soil. The canopy height of the corn was 85 cm, sunflowers 92 cm, and cabbage 35 cm. The soil moisture under the corn was measured with a hand held probe to be about 23% VWC, sunflowers 32% VWC, and cabbage about 35% VWC: saturation for this soil.

When the tag was on the surface of the soil, the read range varied primarily with soil moisture: cabbage had the wettest soil and the shortest read range. When the tag was raised on a block, the impact of soil moisture was reduced, and canopy density became a more significant factor: sunflowers had the densest canopy and the shortest read range.

To quantify the canopy density, imaging processing software (MATLAB Image Processing Toolbox, MathWorks, Natick, Massachusetts, USA) was used to calculate canopy closure, or the percentage of the representative overhead image covered by

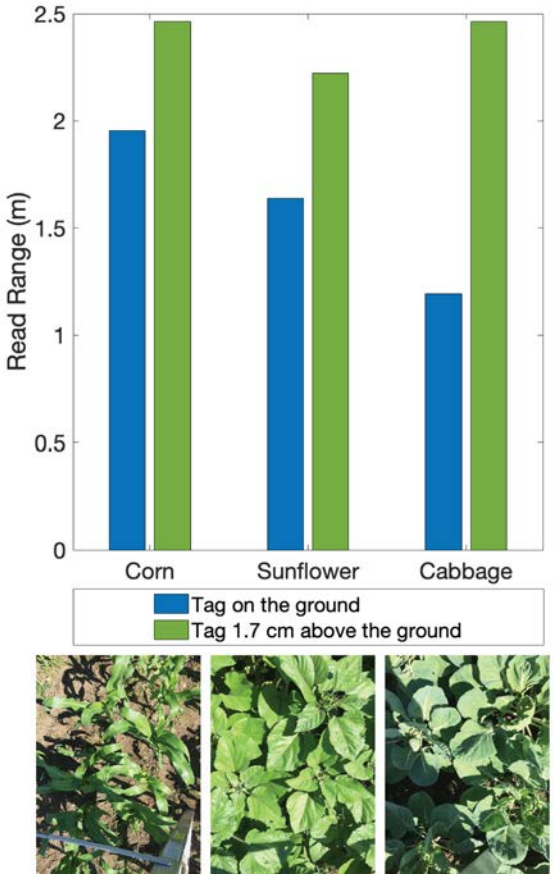

Figure 6.10: Maximum measured read range for tags under three types of crop canopies.

green leaves. The corn had about 43% canopy closure, cabbage 90%, and sunflower 100%. Importantly, read ranges of over 2 m were possible in all three crop types with only 1.7 cm of spacing between the antenna and the soil, even in the dense canopy of the sunflowers.

6.4 Conclusions

Real soil and crop conditions complicate the operation of each component of the biodegradable sensor node, but engineering solutions are available to make functional devices.

Microbial action in soil degrades materials, but beeswax is an effective encapsulant to extend sensor lifetimes to at least 90 days.

Nitrate sensor readings are impacted by soil type and soil moisture level, but do show good linear responses between soil nitrate level and sensor output. More study of soil properties on nitrate sensor operation is needed. The variation seen to date could presently be managed by sensor- and soil-specific calibration at the beginning of an experiment.

Wireless communication links which power passive RFID tags is significantly hampered by wet soil, but adding some space between tag and ground mitigates this problem. Crop canopy is not a detrimental issue for vertical reading

All in all, these field experiments are promising for the future deployment of integrated sensor nodes in real fields.

Chapter 7

Conclusions and Future Directions

This thesis has described the building blocks for and steps towards assembling a printed, biodegradable, passive, wireless soil nitrate sensor node. These parts are: biodegradable materials and appropriate fabrication techniques for working with them, potentiometric nitrate sensors, and antennas for RFID. The biodegradable materials have been used to fabricate biodegradable nitrate sensors and biodegradable RFID antennas. The RFID antennas have been integrated with RFICs. The nitrate sensors have been integrated with low-cost read-out electronics. Materials, nitrate sensors, and RFID communication links have all be demonstrated in field or soil conditions. A few integration steps remain particularly challenging: integration of commercial RFIC with biodegradable materials, and reading potentiometric sensors with an RFIC. These can be solved with further materials study and specific IC design, respectively.

In this future-directions chapter, I discuss three areas of future work and applications. First, the remaining work for integrated fabrication of the biodegradable wireless nitrate sensor node. Second, I explain some of the uses that each of the constituent parts have individually. Finally, I suggest some ways the parts could be combined for impactful deployment, and the advantages and disadvantages to different systems.

7.1 Integrated Fabrication

To date, the functional nitrate sensors and functional RFID antennas have been printed on separate substrates and connected with wires, sometimes with the aid of PCB break-out boards. A streamlined fabrication process is needed to fully realize the benefits of printing. A prototype of a full process flow is illustrated in figure 7.1

and consists of the following steps:

1. Treat wooden substrate with blade-coated beeswax or PCL
2. Laser cut stake pattern from treated wood
3. Screen print zinc
4. Acid treat and dry zinc
5. Screen or stencil print carbon for the ion-selective electrode and silver/silver-chloride for the reference electrode
6. Attach RFID chip using flip-chip
7. Prepare wax encapsulation sheets, cut to shape with windows for nitrate electrodes
8. Adhere wax encapsulation sheets.
9. Dip-coat extra layer of wax on upper portions of stake
10. Drop-cast nitrate sensor membrane and reference membranes.

Although this process was successfully used to make non-functional demonstration samples, the electrical performance and lifetime of functional stakes made this way has not be tested. There is room for improvement in several of these steps.

The order of step 3 could be changed. If a large screen printer is available, multiple sensor nodes could be printed on a single large board and released later, any time before RFID attachment. Printing on pre-cut stakes requires at least coarse alignment in the screen printer, while cutting out pre-printed patterns requires alignment at the laser-cutter. Limited area of screens and screen printers may require printing one sample at a time.

The chip attachment process requires further consideration. The basic steps outlined in section 5.1 provide a framework. The same silver paste, or another commercial conductive epoxy, may provide sufficient electrical connection between the chip and the printed zinc traces. Silver pastes and conductive epoxies are not biodegradable, but neither is the chip. It may be possible to switch this connecting material for additional zinc ink, or re-wetting of pre-patterned zinc ink. The chip itself still represents the bulk of the non-biodegradable mass of the sensor node, and reducing that is an important step towards full biodegradability. A bare silicon die could be used in place of the packaged die used in prototyping. Connecting bare die

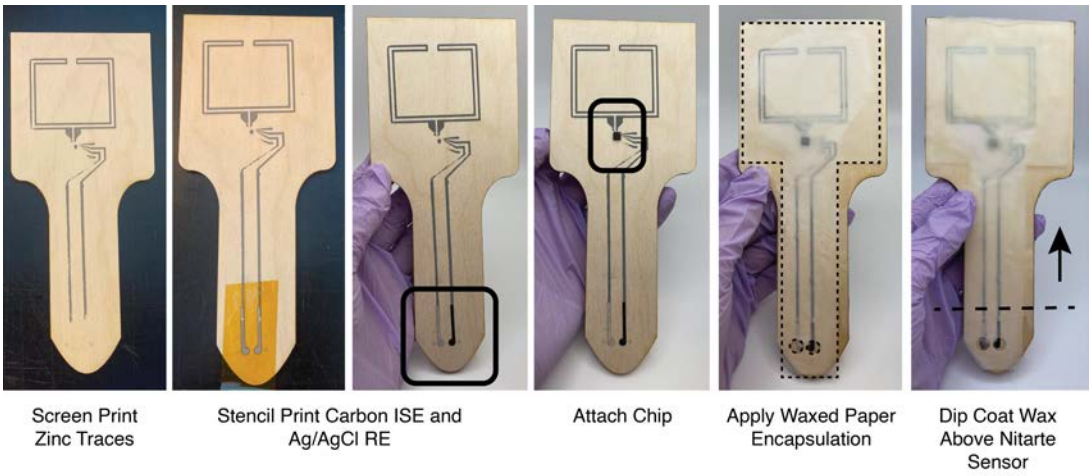

Figure 7.1: A prototype of a process for printing the full sensor node begins with substrate preparation, followed by zinc printing, nitrate sensor electrode printing, chip attachment, and two wax encapsulation steps.

to printed traces requires an entirely different suite of tools and processes than those of section 5.1, and would require research and development.

The wax encapsulation process in particular is an area ready for improvement and creativity. The zinc traces require excellent adhesion between the top encapsulation and the substrate to keep out humidity. The nitrate sensors require open windows over the electrodes to allow electrochemical contact between the sensor membrane and the liquid part of the soil. There are many ways of processing beeswax, most with roots in traditional crafting of everyday objects like candles or bowls. Four wax processing techniques that we have used are dipping, pouring wax into molds, creating thin sheets through dipping wet wood, and creating wax paper by dipping papers. Processing wax in one-step methods–dipping the full sample or using a single mold–provides the best seal of encapsulation to substrate because the exterior coat of wax cools simultaneously. Using prepared sheets of wax or waxed paper allows patterning of windows, but the joint between the sheet and the substrate is not seamless and can lead to leaks, especially when not reinforced by an extra coat of wax. Further work in wax processing or the use of alternative waterproof biodegradable encapsulation materials would improve the fabrication and reliability of biodegradable nitrate sensor nodes.

7.2 Deployment of Parts

As we have seen, the principle scientific and engineering advances that enable printed biodegradable wireless soil nitrate sensor nodes concern biodegradable electronic materials especially high-conductivity zinc, quantifying passive wireless communication in and around soil and plants, and the nitrate sensors. Each of these three areas individually have numerous applications.

Biodegradable Materials

Biodegradable electronics of course have numerous applications, from simply reducing waste generated by consumer electronics to environmental monitoring. The increased lifetime of highly conductive biodegradable zinc is an important building block for any biodegradable device with a desired operational lifetime of more than a few days.

The materials set of wooden stakes, beeswax printing surfaces, zinc conductors, and beeswax encapsulation layers is well suited for a few types of soil moisture sensors. In 2021, Sui et al. reported a capacitive soil moisture sensor using Zinc-PVP with beeswax encapsulation. In order to achieve lifetimes of more than two weeks, a 1 mm thick encapsulation layer was needed, but this thick encapsulation reduced sensitivity and the sensors suffered from drift before their breakdown [156]. The more stable zinc-PCL ink could improve the lifetime of similar capacitive soil moisture sensors while reducing the wax encapsulation thickness required. Similar capacitive sensors can be used to measure water or other liquid levels, or as interactive touch sensors.

Passive RFID

Besides environmental monitoring, the ability to wirelessly communicate with sensor tags can be used for wearable health monitoring devices [157, 158, 159], medical applications [160], smart packaging [161], and vehicular technology [162]. RFID tags are expected to have major impact in the transport of perishable goods [163], supply-chain management [164], and warehouse management [165], especially for high-value products. Dynamic inventory tracking and multi-user quality control could benefit from a network of nodes which only requires the central reader to have an energy source. Passive tags, with a variety of sensors, can allow for distributed, mobile, and interactive sensing.

In the area of environmental monitoring, RFID tags can be used as soil moisture monitors, where the signal strength is an indicator of soil wetness. This has been shown before using non-degradable buried or partially buried devices [152,

120]. Switching from conventional to biodegradable materials could be especially impactful for buried tags to reduce waste and avoid toxic pollution, as buried sensors are likely to be extremely difficult to retrieve. In this use case, the extended lifetime of conductive zinc would be important because sensor placement is relatively labor-intensive, so sensor lifetime needs to be longer than a few days to justify the investment in installation.

Nitrate Sensors

Measuring nitrate in soil in real time is critically important for both agricultural and environmental science applications, but is nearly impossible today because the tools for in-situ nitrate measurement do not exist. Researchers in many areas of life- and earth-sciences need field-deployable nitrate sensors, and do not necessarily require them to be biodegradable or integrated with wireless read-out electronics.

Many researchers already have highly-instrumented field sites. Existing sensor infrastructure might include weather stations, eddy covariance flux towers, gas flux chambers, groundwater well sampling taps, and suction lysimeters for subsurface water sampling. Printed soil nitrate sensors could be added to agricultural research sites to understand how nitrate moves around a field, the scale of spacial variation of nitrate, and the effectiveness of variable-rate application technology. Sensors at different depths in any environment could provide information on nitrate leaching to groundwater. In conjunction with other soil physical and chemical sensors, nitrate sensors could be used to understand conditions which lead to nitrous oxide emissions, or which promote carbon sequestration in soil. These are areas we are beginning to explore now.

Working at highly-instrumented field sites relaxes several technical requirements on the sensors themselves. First, data loggers and power infrastructure exists at research sites. We have already demonstrated reading of printed nitrate sensors with widely-used Campbell Scientific data loggers. Having a reliable way to read the sensors removes concerns related to variation in hand-soldered circuit boards or errors from low-impedance readers used in inexpensive set ups. The powered system can also record data as frequently as desired, which will help us find short-term spikes which would otherwise be missed. Secondly, the presence of research equipment relaxes the biodegradability requirement as routine maintenance is already required for existing equipment. Non-degradable nitrate sensors should still use a carbon solid contact layer, but plastic and Teflon encapsulation can be used to minimize physical breakdown as a cause of sensor drift. Furthermore, conventional wires can be used, so nitrate sensors can be placed at multiple depths with long wires to connect to data logging hubs.

The technical advances in the nitrate sensor itself which are required to enable widespread deployment at research field sites are improved stability over time and further studies of the impact of soil properties on the nitrate sensor.

7.3 Full System Use Cases and Improvements

The system envisioned here–biodegradable sensor nodes which are passive (battery-free), printed, and low-cost–read by an RFID interrogator is technically feasible, but there are a few engineering challenges to overcome for its full realization. Primarily, electronics with high input impedance and amplifier input range suitable for reading potentiometric sensors are needed to integrate the nitrate sensor with the printed RFID tag. Additionally, modifications to the antenna design may be needed to account for loading by long sensor leads. Fundamentally, though, the biodegradable nitrate sensors have been used to read nitrate concentration in soil, printed RFID tags can wirelessly communicate data from attached printed sensors without on-board power, antennas can be made out of biodegradable materials, and wireless communication links are possible from tags slightly above wet soil and under crop canopies. This RFID-enabled system offers the advantages of full biodegradability of the in-soil nodes and extremely low cost of sensor nodes when produced at scale. Reading strategies could offer measurements prior to each fertilizer application, an event which happens a few times per season.

The advantages come with design trade-offs, however. The chief disadvantage of a fully passive sensor node is that no data is collected unless the sensor is being read. This leads to very low temporal resolution. The sensors, biodegradable materials, and antenna designed here could be integrated with a different chip using another protocol in the 915 MHz band–LoRa, ZigBee, or SigFox for example–to create a sensor network with more frequent measurements. Such a system would require innovations in biodegradable power sources such as batteries, microbial fuel cells, photovoltaics, or other energy harvesting devices.

Bibliography

[1] Ken Russel and Leah Sandall. *Corn Breeding: Lessons From the Past*. URL: https://passel2.unl.edu/view/lesson/c3ded390efbf/10.

[2] Alex Escolà, Viacheslav Adamchuk, and ISPA Board. *Precision Ag Definition*. 2019. URL: https://www.ispag.org/about/definition.

[3] David Mulla and Raj Khosla. "Historical Evolution and Recent Advances in Precision Farming". In: *Soil-Specific Farming: Precision Agriculture*. Ed. by Rattan Lal and B.A. Steward. CRC Press, 2016, pp. 1–36.

[4] *Landsat Overview — NASA*.

[5] *Mapping with Drones for Precision Agriculture — Virginia Cooperative Extension - Virginia State University*.

[6] Roberto N. Barbosa. "Crop Yield Monitors". In: *Louisiana State University Agricultural Center* (2012).

[7] M.C. Nolin, S.P. Guertin, and C. Wang. "Within-Field Spatial Variability of Soil Nutrients and Corn Yield in a Montreal Lowlands Clay Soil". In: 2015. DOI: 10.2134/1996.precisionagproc3.c26.

[8] Ruth Kerry and Margaret A Oliver. *Precision Agriculture, 4*. Tech. rep. 278. 2003.

[9] W. K. Jung et al. "Spatial Characteristics of Claypan Soil Properties in an Agricultural Field". In: *Soil Science Society of America Journal* 70.4 (2006). ISSN: 03615995. DOI: 10.2136/sssaj2005.0273.

[10] Qiang Cao et al. "Quantifying spatial variability of indigenous nitrogen supply for precision nitrogen management in small scale farming". In: *Precision Agriculture* 13.1 (2012). ISSN: 13852256. DOI: 10.1007/s11119-011-9244-3.

[11] Francisca López-Granados et al. "Spatial variability of agricultural soil parameters in southern Spain". In: *Plant and Soil* 246.1 (2002). ISSN: 0032079X. DOI: 10.1023/A:1021568415380.

[12] R. Kerry, M. A. Oliver, and Z. L. Frogbrook. "Sampling in Precision Agriculture". In: *Geostatistical Applications for Precision Agriculture* (2010), pp. 35–63. DOI: 10.1007/978-90-481-9133-8{_}2.

[13] J. M. Blonquist, S. B. Jones, and D. A. Robinson. "Precise irrigation scheduling for turfgrass using a subsurface electromagnetic soil moisture sensor". In: *Agricultural Water Management* 84.1-2 (July 2006), pp. 153–165. ISSN: 03783774. DOI: 10.1016/j.agwat.2006.01.014.

[14] Subash Dahal et al. "Variable Rate Nitrogen and Water Management for Irrigated Maize in the Western US". In: 10 (2020). DOI: 10.3390/agronomy10101533.

[15] William R. Raun et al. "Improving nitrogen use efficiency in cereal grain production with optical sensing and variable rate application". In: *Agronomy Journal* 94.4 (2002). ISSN: 00021962. DOI: 10.2134/agronj2002.8150.

[16] David W Dibb. "The Mysteries (Myths) of Nutrient Use Efficiency". In: *Better Crops with Plant Food* 3.84 (2000), pp. 3–5. URL: www.ppi-far.org.

[17] Claine Jones. *Fertilizer Economics*. URL: https://econtools.msuextension.org/nitrogen/springwheat.html.

[18] Anne Bernhard. "The Nitrogen Cycle: Processes, Players, and Human Impact." In: *Nature Education Knowledge* 3.10 (2010).

[19] Marcal Capdevila-Cortada. "Electrifying the Haber–Bosch". In: *Nature Catalysis 2019 2:12* 2.12 (Dec. 2019), pp. 1055–1055. ISSN: 2520-1158. DOI: 10.1038/s41929-019-0414-4.

[20] Seyedehhoma Ghavam et al. "Sustainable Ammonia Production Processes". In: *Frontiers in Energy Research* 9 (Mar. 2021), p. 34. ISSN: 2296598X. DOI: 10.3389/FENRG.2021.580808/BIBTEX.

[21] *Soil Test Interpretations and Fertilizer Recommendations*. 2003. URL: https://bookstore.ksre.ksu.edu/pubs/mf2586.pdf.

[22] Keith Good. *Fertilizer Prices Rise, But Pace Slows • Farm Policy News*. Jan. 2022. URL: https://farmpolicynews.illinois.edu/2022/01/fertilizer-prices-rise-but-pace-slows/.

[23] Kyle P. Messier et al. "Modeling groundwater nitrate exposure in private wells of North Carolina for the Agricultural Health Study". In: *Science of The Total Environment* 655 (Mar. 2019), pp. 512–519. ISSN: 0048-9697. DOI: 10.1016/J.SCITOTENV.2018.11.022.

[24] Mary H. Ward et al. *Drinking water nitrate and human health: An updated review*. 2018. DOI: 10.3390/ijerph15071557.

[25] Christopher J. Gobler et al. "The role of nitrogenous nutrients in the occurrence of harmful algal blooms caused by Cochlodinium polykrikoides in New York estuaries (USA)". In: *Harmful Algae* 17 (May 2012), pp. 64–74. ISSN: 1568-9883. DOI: 10.1016/J.HAL.2012.03.001.

[26] William G. Crumpton, Thomas M. Isenhart, and Paul D. Mitchell. "Nitrate and organic N analyses with second-derivative spectroscopy". In: *Limnology and Oceanography* 37.4 (June 1992), pp. 907–913. ISSN: 1939-5590. DOI: 10.4319/LO.1992.37.4.0907.

[27] A. SEMPERE, J. OLIVER, and C. RAMOS. "Simple determination of nitrate in soils by second-derivative spectroscopy". In: *Journal of Soil Science* 44.4 (Dec. 1993), pp. 633–639. ISSN: 1365-2389. DOI: 10.1111/J.1365-2389.1993.TB02328.X.

[28] Iael Raij Hoffman and Isaya Kisekka. "Evaluating Nitrogen Leaching in Processing Tomatoes for Enhanced Productivity and Sustainability." In: *Proceedings of the ASA, CSSA, SSSA International Annual Meeting*. Salt Lake City, UT, USA: ASA, CSSA, SSSA, Nov. 2021.

[29] Vamsi Talla et al. "LoRa Backscatter: Enabling The Vision of Ubiquitous Connectivity". In: *Proc. ACM Interact. Mob. Wearable Ubiquitous Technol* 1.105 (2017). DOI: 10.1145/3130970. URL: https://doi.org/10.1145/3130970.

[30] Haider Mahmood Jawad et al. *Energy-efficient wireless sensor networks for precision agriculture: A review*. Aug. 2017. DOI: 10.3390/s17081781.

[31] Tamoghna Ojha, Sudip Misra, and Narendra Singh Raghuwanshi. "Wireless sensor networks for agriculture: The state-of-the-art in practice and future challenges". In: *Computers and Electronics in Agriculture* 118 (Oct. 2015), pp. 66–84. ISSN: 0168-1699. DOI: 10.1016/J.COMPAG.2015.08.011.

[32] Haider Mahmood Jawad et al. "Energy-efficient wireless sensor networks for precision agriculture: A review". In: *Sensors (Switzerland)* 17.8 (Aug. 2017). ISSN: 14248220. DOI: 10.3390/S17081781.

[33] Roy Want. "Near field communication". In: *IEEE Pervasive Computing* 10.3 (2011). ISSN: 15361268. DOI: 10.1109/MPRV.2011.55.

[34] Sangkil Kim et al. "Inkjet-printed Sensors on Paper Substrate for Agricultural Applications". In: (2013), pp. 866–869.

[35] Jasmine Jan et al. "Flexible Blade-Coated Optoelectronic Devices: Dual Functionality via Simultaneous Deposition". In: *Advanced Functional Materials* (2022), p. 2112343. ISSN: 1616-3028. DOI: 10.1002/ADFM.202112343.

[36] Donggeon Han et al. "Flexible Blade-Coated Multicolor Polymer Light-Emitting Diodes for Optoelectronic Sensors". In: *Advanced Materials* 29.22 (June 2017), p. 1606206. ISSN: 1521-4095. DOI: 10.1002/ADMA.201606206.

[37] Vasileios Lakafosis et al. "Progress towards the first wireless sensor networks consisting of inkjet-printed, paper-based RFID-enabled sensor tags". In: *Proceedings of the IEEE* 98.9 (2010), pp. 1601–1609. ISSN: 00189219. DOI: 10.1109/JPROC.2010.2049622.

[38] Yasser Khan et al. "A New Frontier of Printed Electronics: Flexible Hybrid Electronics". In: *Advanced Materials* 32.15 (Apr. 2020). ISSN: 15214095. DOI: 10.1002/ADMA.201905279.

[39] Arno Thielens et al. "Fabrication and Characterization of Flexible Spray-Coated Antennas". In: *IEEE Access* 6 (2018), pp. 62050–62061. ISSN: 21693536. DOI: 10.1109/ACCESS.2018.2876286.

[40] Nagarajan Palavesam et al. "Roll-to-roll processing of film substrates for hybrid integrated flexible electronics". In: (2018). DOI: 10.1088/2058-8585/aaaa04. URL: https://doi.org/10.1088/2058-8585/aaaa04.

[41] Irfan Mir and D. Kumar. "Recent advances in isotropic conductive adhesives for electronics packaging applications". In: *International Journal of Adhesion and Adhesives* 28.7 (Oct. 2008), pp. 362–371. ISSN: 0143-7496. DOI: 10.1016/J.IJADHADH.2007.10.004. URL: https://www.sciencedirect.com/science/article/pii/S0143749607001029.

[42] Jian Lin et al. "Laser-induced porous graphene films from commercial polymers". In: *Nature Communications 2014 5:1* 5.1 (Dec. 2014), pp. 1–8. ISSN: 2041-1723. DOI: 10.1038/ncomms6714.

[43] Laure V. Kayser and Darren J. Lipomi. "Stretchable Conductive Polymers and Composites Based on PEDOT and PEDOT:PSS". In: *Advanced Materials* 31.10 (Mar. 2019), p. 1806133. ISSN: 1521-4095. DOI: 10.1002/ADMA.201806133.

[44] Madhur Atreya et al. "Poly(lactic acid)-Based Ink for Biodegradable Printed Electronics with Conductivity Enhanced through Solvent Aging". In: *ACS Applied Materials and Interfaces* 12.20 (May 2020), pp. 23494–23501. ISSN: 19448252. DOI: 10.1021/acsami.0c05196.

[45] Xian Huang et al. "Biodegradable Materials for Multilayer Transient Printed Circuit Boards". In: *Advanced Materials* 26.43 (Nov. 2014), pp. 7371–7377. ISSN: 1521-4095. DOI: 10.1002/ADMA.201403164.

[46] Tao Zhang et al. "Electrical interconnects fabricated from biodegradable conductive polymer composites". In: *IEEE Transactions on Components, Packaging and Manufacturing Technology* 9.5 (May 2019), pp. 822–829. ISSN: 21563985. DOI: 10.1109/TCPMT.2019.2905154.

[47] Kyung Sub Kim et al. "Biodegradable Molybdenum/Polybutylene Adipate Terephthalate Conductive Paste for Flexible and Stretchable Transient Electronics". In: *Advanced Materials Technologies* 7.2 (Feb. 2022), p. 2001297. ISSN: 2365-709X. DOI: 10.1002/ADMT.202001297.

[48] Bikram K Mahajan et al. "Mechanically Milled Irregular Zinc Nanoparticles for Printable Bioresorbable Electronics". In: *Small* 13.17 (May 2017), p. 1700065. ISSN: 1613-6829. DOI: 10.1002/SMLL.201700065.

[49] Wan Shou et al. "Low-Cost Manufacturing of Bioresorbable Conductors by Evaporation–Condensation-Mediated Laser Printing and Sintering of Zn Nanoparticles". In: *Advanced Materials* 29.26 (July 2017), p. 1700172. ISSN: 1521-4095. DOI: 10.1002/ADMA.201700172.

[50] Yoon Kyeung Lee et al. "Room Temperature Electrochemical Sintering of Zn Microparticles and Its Use in Printable Conducting Inks for Bioresorbable Electronics". In: *Advanced Materials* 29.38 (Oct. 2017). ISSN: 15214095. DOI: 10.1002/adma.201702665.

[51] Subimal Majee et al. "Low temperature chemical sintering of inkjet-printed Zn nanoparticles for highly conductive flexible electronic components". In: *npj Flexible Electronics* 5.1 (Dec. 2021). ISSN: 23974621. DOI: 10.1038/s41528-021-00111-1.

[52] Beatriz C. Almeida, Pedro Figueiredo, and Alexandra T.P. Carvalho. "Polycaprolactone Enzymatic Hydrolysis: A Mechanistic Study". In: *ACS Omega* 4.4 (Apr. 2019), pp. 6769–6774. ISSN: 24701343. DOI: 10.1021/ACSOMEGA.9B00345/ASSET/IMAGES/LARGE/AO-2019-00345J{_}0005.JPEG.

[53] Ludmila Vanharova, Marketa Julinova, and Roman Slavik. "PVP Based Materials: Biodegradation in Different Environments". In: *Ecological Chemistry and Engineering S* 24.2 (June 2017), pp. 299–309. ISSN: 18986196. DOI: 10.1515/ECES-2017-0021.

[54] B. Jirgensons. "Solubility and fractionation of polyvinylpyrrolidone". In: *Journal of Polymer Science* 8.5 (May 1952), pp. 519–527. ISSN: 1542-6238. DOI: 10.1002/POL.1952.120080508.

[55] Ariagna L. Rivera-Briso and Ángel Serrano-Aroca. "Poly(3-Hydroxybutyrate-co-3-Hydroxyvalerate): Enhancement Strategies for Advanced Applications". In: *Polymers* 10.7 (July 2018). ISSN: 20734360. DOI: 10.3390/POLYM10070732.

[56] Yuanpeng Wang et al. "Biosynthesis and Thermal Properties of PHBV Produced from Levulinic Acid by Ralstonia eutropha". In: *PLoS ONE* 8.4 (Apr. 2013). ISSN: 19326203. DOI: 10.1371/JOURNAL.PONE.0060318.

[57] A. P. Tulloch. "The composition of beeswax and other waxes secreted by insects". In: *Lipids 1969 5:2* 5.2 (Feb. 1970), pp. 247–258. ISSN: 1558-9307. DOI: 10.1007/BF02532476.

[58] A. P. Tulloch. "Beeswax: Structure of the esters and their component hydroxy acids and diols". In: *Chemistry and Physics of Lipids* 6.3 (1971). ISSN: 00093084. DOI: 10.1016/0009-3084(71)90063-6.

[59] W. F. Tinto, T. O. Elufioye, and J. Roach. "Waxes". In: *Pharmacognosy: Fundamentals, Applications and Strategy* (Jan. 2017), pp. 443–455. DOI: 10.1016/B978-0-12-802104-0.00022-6.

[60] Filippo Fratini et al. *Beeswax: A minireview of its antimicrobial activity and its application in medicine*. 2016. DOI: 10.1016/j.apjtm.2016.07.003.

[61] Vivian R. Feig, Helen Tran, and Zhenan Bao. "Biodegradable Polymeric Materials in Degradable Electronic Devices". In: *ACS Central Science* 4.3 (2018). ISSN: 23747951. DOI: 10.1021/acscentsci.7b00595.

[62] Subash Dahal et al. "Degradability of biodegradable soil moisture sensor components and their effect on maize (Zea mays l.) growth". In: *Sensors (Switzerland)* 20.21 (Nov. 2020), pp. 1–13. ISSN: 14248220. DOI: 10.3390/s20216154.

[63] Yongkun Sui et al. "A Reactive Inkjet Printing Process for Fabricating Biodegradable Conductive Zinc Structures". In: *Advanced Engineering Materials* (July 2022), p. 2200529. ISSN: 1438-1656. DOI: 10.1002/ADEM.202200529.

[64] Steven Abbott. *HSP Basics — Practical Solubility Science — Prof Steven Abbott*. URL: https://www.stevenabbott.co.uk/practical-solubility/hsp-basics.php.

[65] Michal Bartnikowski et al. "Degradation mechanisms of polycaprolactone in the context of chemistry, geometry and environment". In: *Progress in Polymer Science* 96 (Sept. 2019), pp. 1–20. ISSN: 0079-6700. DOI: 10.1016/J.PROGPOLYMSCI.2019.05.004.

[66] Nils Jürgensen et al. "Biodegradable Polycaprolactone as Ion Solvating Polymer for Solution-Processed Light-Emitting Electrochemical Cells". In: *Scientific Reports 2016 6:1* 6.1 (Nov. 2016), pp. 1–7. ISSN: 2045-2322. DOI: 10.1038/srep36643.

[67] Beth A Miller-Chou and Jack L Koenig. "A review of polymer dissolution". In: *Profess in Polymer Science* 28 (2003), pp. 1223–1270. DOI: 10.1016/S0079-6700(03)00045-5.

[68] Denis Prat et al. "CHEM21 selection guide of classical- and less classical-solvents". In: *Green Chemistry* 18.1 (Dec. 2015), pp. 288–296. ISSN: 1463-9270. DOI: 10.1039/C5GC01008J. URL: https://pubs.rsc.org/en/content/articlehtml/2016/gc/c5gc01008j%20https://pubs.rsc.org/en/content/articlelanding/2016/gc/c5gc01008j.

[69] Steven Abbott. *How to be a great Screen printer*. Macdermid Autotype Limited, 2008. ISBN: 9780955122019.

[70] Kaushik Jayasayee et al. "Cold sintering as a cost-effective process to manufacture porous zinc electrodes for rechargeable zinc-air batteries". In: *Processes* 8.5 (May 2020). ISSN: 22279717. DOI: 10.3390/PR8050592.

[71] Subimal Majee et al. "Low temperature chemical sintering of inkjet-printed Zn nanoparticles for highly conductive flexible electronic components". In: *npj Flexible Electronics* 5.1 (Dec. 2021). ISSN: 23974621. DOI: 10.1038/s41528-021-00111-1.

[72] Carol L. Baumbauer et al. "Printed Potentiometric Nitrate Sensors for Use in Soil". In: *Sensors 2022, Vol. 22, Page 4095* 22.11 (May 2022), p. 4095. ISSN: 1424-8220. DOI: 10.3390/S22114095.

[73] G J Moody, R B Oke, and J D R Thomas. *A Calcium-sensitive Electrode Based on a L'iquid Ion Exchanger in a Poly(viny1 chloride) Matrix*. Tech. rep. 1970, pp. 910–918.

[74] R. D. Armstrong and G. Horvai. "Properties of PVC based membranes used in ion-selective electrodes". In: *Electrochimica Acta* 35.1 (Jan. 1990), pp. 1–7. ISSN: 0013-4686. DOI: 10.1016/0013-4686(90)85028-L.

[75] Lianlian Wang et al. "Fabrication and characterization of a fluorescent sensor based on Rh 6G-functionlized silica nanoparticles for nitrite ion detection". In: *Sensors and Actuators, B: Chemical* 171-172 (Aug. 2012), pp. 946–953. ISSN: 09254005. DOI: 10.1016/j.snb.2012.06.008.

[76] Manuel Gutiérrez et al. "Electronic tongue for the determination of alkaline ions using a screen-printed potentiometric sensor array". In: *Microchimica Acta* 163.1-2 (Sept. 2008), pp. 81–88. ISSN: 00263672. DOI: 10.1007/s00604-007-0894-9.

[77] Juliane R. Sempionatto et al. *Wearable Chemical Sensors: Emerging Systems for On-Body Analytical Chemistry*. 2019. DOI: 10.1021/acs.analchem.9b04668.

[78] Nipapan Ruecha et al. "Fully Inkjet-Printed Paper-Based Potentiometric Ion-Sensing Devices". In: *Analytical Chemistry* 89.19 (Oct. 2017), pp. 10608–10616. ISSN: 15206882. DOI: 10.1021/acs.analchem.7b03177.

[79] Van Anh T. Dam and Marcel A.G. Zevenbergen. "Low Cost Nitrate Sensor for Agricultural Applications". In: *EUROSENSORS XXXIII* (June 2019).

[80] Shuto Osaki et al. "Investigation of polyurethane matrix membranes for salivary nitrate isfets to prevent the drift". In: *Sensors (Switzerland)* 19.12 (June 2019). ISSN: 14248220. DOI: 10.3390/s19122713.

[81] Yuzhou Shao, Yibin Ying, and Jianfeng Ping. "Recent advances in solid-contact ion-selective electrodes: functional materials, transduction mechanisms, and development trends". In: *Chemical Society Reviews* 49.13 (July 2020), pp. 4405–4465. ISSN: 14604744. DOI: 10.1039/C9CS00587K.

[82] Philippe Bühlmann and Li D. Chen. "Ion-Selective Electrodes with Ionophore-Doped Sensing Membranes". In: Wiley, 2012, p. 3978. ISBN: 9780470746400.

[83] BY P T Gilbert. "The Use of Silver-Silver Chloride Reference Electrodes in Dilute Solutions". In: *Discuss. Faraday SOc.* 1 (1947), pp. 320–328.

[84] Marios Sophocleous and John K. Atkinson. *A review of screen-printed silver/silver chloride (Ag/AgCl) reference electrodes potentially suitable for environmental potentiometric sensors*. Nov. 2017. DOI: 10.1016/j.sna.2017.10.013.

[85] R. Goldy. *Anions and Cations in Plants, Oh My! But Why do We Care?* 2013.

[86] Yingzheng Fan et al. "Toward long-term accurate and continuous monitoring of nitrate in wastewater using poly (tetrafluoroethylene) (PTFE)Solid-state ion-selective electrodes (S-ISEs)". In: *ACS Sensors* 5.10 (Oct. 2020), pp. 3182–3193. ISSN: 23793694. DOI: 10.1021/ACSSENSORS.0C01422/ASSET/IMAGES/LARGE/SE0C01422{_}0007.JPEG.

[87] Jittima Choosang et al. "Simultaneous detection of ammonium and nitrate in environmental samples using on ion-selective electrode and comparison with portable colorimetric assays". In: *Sensors (Switzerland)* 18.10 (Oct. 2018). ISSN: 14248220. DOI: 10.3390/s18103555.

[88] Xiaofan Jiang et al. *Wireless Sensor Network Utilizing Flexible Nitrate Sensors for Smart Farming; Wireless Sensor Network Utilizing Flexible Nitrate Sensors for Smart Farming*. 2019. ISBN: 9781728116341.

[89] Nate T. Garland et al. "Flexible Laser-Induced Graphene for Nitrogen Sensing in Soil". In: *ACS Applied Materials and Interfaces* 10.45 (Nov. 2018), pp. 39124–39133. ISSN: 19448252. DOI: 10.1021/acsami.8b10991.

[90] Md Azahar Ali et al. "Continuous Monitoring of Soil Nitrate Using a Miniature Sensor with Poly(3-octyl-thiophene) and Molybdenum Disulfide Nanocomposite". In: *ACS Applied Materials and Interfaces* 11.32 (Aug. 2019), pp. 29195–29206. ISSN: 19448252. DOI: 10.1021/acsami.9b07120.

[91] Wenzhi Tang et al. "All-solid-state nitrate-selective electrode and its application in drinking water". In: *Electrochimica Acta* 81 (Oct. 2012), pp. 186–190. ISSN: 00134686. DOI: 10.1016/j.electacta.2012.07.073.

[92] Lei Zhang, Zhengying Wei, and Pengcheng Liu. "An all-solid-state NO3- ion-selective electrode with gold nanoparticles solid contact layer and molecularly imprinted polymer membrane". In: *PLOS ONE* 15.10 (Oct. 2020), e0240173. ISSN: 1932-6203. DOI: 10.1371/JOURNAL.PONE.0240173.

[93] Ming Chen et al. "An All-Solid-State Nitrate Ion-Selective Electrode with Nanohybrids Composite Films for In-Situ Soil Nutrient Monitoring". In: *Sensors 2020, Vol. 20, Page 2270* 20.8 (Apr. 2020), p. 2270. ISSN: 1424-8220. DOI: 10.3390/S20082270.

[94] Magdalena Pik, Robert Piech, and Beata Paczosa-Bator. "All-solid-state nitrate selective electrode with graphene/tetrathiafulvalene nanocomposite as high redox and double layer capacitance solid contact". In: *Electrochimica Acta* 210 (Aug. 2016), pp. 407–414. ISSN: 0013-4686. DOI: 10.1016/J.ELECTACTA.2016.05.170.

[95] Karolina Pietrzak and Cecylia Wardak. "Comparative study of nitrate all solid state ion-selective electrode based on multiwalled carbon nanotubes-ionic liquid nanocomposite". In: *Sensors and Actuators B: Chemical* 348 (Dec. 2021). ISSN: 09254005. DOI: 10.1016/j.snb.2021.130720.

[96] Tatyana A. Bendikov, Juyoul Kim, and Thomas C. Harmon. "Development and environmental application of a nitrate selective microsensor based on doped polypyrrole films". In: *Sensors and Actuators B: Chemical* 106.2 (May 2005), pp. 512–517. ISSN: 0925-4005. DOI: 10.1016/J.SNB.2004.07.018.

[97] Donald Hornek et al. "Soil Test Interpretation Guide ". In: *Oregon State University Extension* (July 2011).

[98] Jinbo Hu, Andreas Stein, and Philippe Bühlmann. *Rational design of all-solid-state ion-selective electrodes and reference electrodes*. Feb. 2016. DOI: 10.1016/j.trac.2015.11.004.

[99] Celeste R. Rousseau and Philippe Bühlmann. *Calibration-free potentiometric sensing with solid-contact ion-selective electrodes*. July 2021. DOI: 10.1016/j.trac.2021.116277.

[100] Alla M. Zamarayeva et al. *Optimization of printed sensors to monitor sodium, ammonium, and lactate in sweat*. 2020. DOI: 10.1063/5.0014836.

[101] Robert W. Cattrall. *Chemical sensors*. Oxford University Press, 1997, p. 74. ISBN: 9780198500902.

[102] Yoshio Umezawa et al. "Potentiometric selectivity coefficients of ion-selective electrodes part I. Inorganic cations (technical report)". In: *Pure and Applied Chemistry* 72.10 (Jan. 2000), pp. 1851–2082. ISSN: 00334545. DOI: 10.1351/PAC200072101851/MACHINEREADABLECITATION/RIS.

[103] Tyler L. Anthony and Whendee L. Silver. "Mineralogical associations with soil carbon in managed wetland soils". In: *Global Change Biology* 26.11 (Nov. 2020), pp. 6555–6567. ISSN: 1365-2486. DOI: 10.1111/GCB.15309.

[104] Tyler L. Anthony and Whendee L. Silver. "Hot moments drive extreme nitrous oxide and methane emissions from agricultural peatlands". In: *Global Change Biology* 27.20 (Oct. 2021), pp. 5141–5153. ISSN: 1365-2486. DOI: 10.1111/GCB.15802.

[105] Monia Fibbioli et al. "Potential drifts of solid-contacted ion-selective electrodes due to zero-current ion fluxes through the sensor membrane". In: *Electroanalysis* 12.16 (2000). ISSN: 10400397. DOI: 10.1002/1521-4109(200011)12:16<1286::AID-ELAN1286>3.0.CO;2-Q.

[106] Hongjie Jiang et al. "A biodegradable sensor housed in 3D printed porous tube for in-situ soil nitrate detection". In: *2018 Solid-State Sensors, Actuators and Microsystems Workshop, Hilton Head 2018*. Transducer Research Foundation, 2018, pp. 148–151. ISBN: 9781940470030. DOI: 10.31438/trf.hh2018.42.

[107] Constantine A. Balanis. "Antenna Theory: Analysis and Design, 4th Edition — Wiley". In: (2016), p. 1104.

[108] C.L. Baumbauer et al. "Printed, flexible, compact UHF-RFID sensor tags enabled by hybrid electronics". In: *Scientific Reports* 10.1 (2020). ISSN: 20452322. DOI: 10.1038/s41598-020-73471-9.

[109] Fawwaz Ulaby, Eric Michielssen, and Umberto Ravaioli. *Fundamentals of Applied Electromagnetics*. 6th ed. Prentice Hall, 2010.

[110] Edward J. Rothwell and Raoul O. Ouedraogo. *Antenna miniaturization: Definitions, concepts, and a review with emphasis on metamaterials*. 2014. DOI: 10.1080/09205071.2014.972470.

[111] Sangkil Kim et al. "Monopole antenna with inkjet-printed EBG array on paper substrate for wearable applications". In: *IEEE Antennas and Wireless Propagation Letters* 11 (2012). ISSN: 15361225. DOI: 10.1109/LAWP.2012.2203291.

[112] Arno Thielens et al. "Fabrication and Characterization of Flexible Spray-Coated Antennas". In: *IEEE Access* 6 (2018), pp. 62050–62061. ISSN: 21693536. DOI: 10.1109/ACCESS.2018.2876286.

[113] Rushi Vyas et al. "Paper-based RFID-enabled wireless platforms for sensing applications". In: *IEEE Transactions on Microwave Theory and Techniques*. Vol. 57. 1. 2009. DOI: 10.1109/TMTT.2009.2017317.

[114] Amin Rida et al. *Conductive inkjet-printed antennas on flexible low-cost paper-based substrates for RFID and WSN applications*. 2009. DOI: 10.1109/MAP.2009.5251188.

[115] Dong-Youn Shin, Yongshik Lee, and Chung Hwan Kim. "Performance characterization of screen printed radio frequency identification antennas with silver nanopaste". In: *Thin Solid Films* 517.21 (Sept. 2009), pp. 6112–6118. ISSN: 0040-6090. DOI: 10.1016/J.TSF.2009.05.019. URL: https://www.sciencedirect.com/science/article/pii/S0040609009009626?via%3Dihub.

[116] Jari Suikkola et al. "Screen-Printing Fabrication and Characterization of Stretchable Electronics". In: *Scientific Reports 2016 6:1* 6.1 (May 2016), pp. 1–8. ISSN: 2045-2322. DOI: 10.1038/srep25784.

[117] M. A. Ziai and J. C. Batchelor. "A prototype passive UHF RFID transfer tattoo tag". In: *Proceedings of the 5th European Conference on Antennas and Propagation, EUCAP 2011*. 2011.

[118] Lingnan Song et al. "Stretchable and reversibly deformable radio frequency antennas based on silver nanowires". In: *ACS Applied Materials and Interfaces* 6.6 (2014). ISSN: 19448252. DOI: 10.1021/am405972e.

[119] Hannu Sillanpaa et al. *Inkjet Printed Wireless Biosensors on Stretchable Substrate*. Tech. rep. 2014. DOI: 10.1109/ICEP.2014.6826704.

[120] Masud A. Aziz et al. "A conformal CPW folded slot antenna array printed on a Kapton substrate". In: *Proceedings of 6th European Conference on Antennas and Propagation, EuCAP 2012*. 2012. DOI: 10.1109/EuCAP.2012.6206028.

[121] Lei Wang et al. "A flexible modified dipole antenna printed on PET film". In: *2012 IEEE Asia-Pacific Conference on Antennas and Propagation, APCAP 2012 - Proceedings*. 2012. DOI: 10.1109/APCAP.2012.6333246.

[122] Li Yang et al. "RFID tag and RF structures on a paper substrate using inkjet-printing technology". In: *IEEE Transactions on Microwave Theory and Techniques*. Vol. 55. 12. 2007. DOI: 10.1109/TMTT.2007.909886.

[123] Pablo Escobedo et al. "Passive UHF RFID Tag for Multispectral Assessment". In: *Sensors 2016, Vol. 16, Page 1085* 16.7 (July 2016), p. 1085. ISSN: 1424-8220. DOI: 10.3390/S16071085.

[124] José Fernández-Salmerón et al. "Passive UHF RFID Tag with Multiple Sensing Capabilities". In: *Sensors 2015, Vol. 15, Pages 26769-26782* 15.10 (Oct. 2015), pp. 26769–26782. ISSN: 1424-8220. DOI: 10.3390/S151026769.

[125] Dimitris E. Anagnostou et al. "A direct-write printed antenna on paper-based organic substrate for flexible displays and WLAN applications". In: *IEEE/OSA Journal of Display Technology* 6.11 (2010). ISSN: 1551319X. DOI: 10.1109/JDT.2010.2045474.

[126] Saud M. Saeed, Constantine A. Balanis, and Craig R. Birtcher. "Inkjet-printed flexible reconfigurable antenna for conformal WLAN/WiMAX wireless devices". In: *IEEE Antennas and Wireless Propagation Letters* 15 (2016). ISSN: 15361225. DOI: 10.1109/LAWP.2016.2547338.

[127] Haider R. Khaleel et al. "Flexible printed monopole antennas for WLAN applications". In: *IEEE Antennas and Propagation Society, AP-S International Symposium (Digest)*. 2011. DOI: 10.1109/APS.2011.5996536.

[128] Sana Ahmed et al. "A Compact Kapton-Based Inkjet-Printed Multiband Antenna for Flexible Wireless Devices". In: *IEEE Antennas and Wireless Propagation Letters* 14 (2015). ISSN: 15361225. DOI: 10.1109/LAWP.2015.2424681.

[129] Hattan F. Abutarboush and Atif Shamim. "Paper-based inkjet-printed tri-band U-slot monopole antenna for wireless applications". In: *IEEE Antennas and Wireless Propagation Letters* 11 (2012). ISSN: 15361225. DOI: 10.1109/LAWP.2012.2223751.

[130] Haider R. Raad et al. "Flexible and compact AMC based antenna for telemedicine applications". In: *IEEE Transactions on Antennas and Propagation* 61.2 (2013). ISSN: 0018926X. DOI: 10.1109/TAP.2012.2223449.

[131] Ting Leng et al. "Graphene Nanoflakes Printed Flexible Meandered-Line Dipole Antenna on Paper Substrate for Low-Cost RFID and Sensing Applications". In: *IEEE Antennas and Wireless Propagation Letters* 15 (2016). ISSN: 15361225. DOI: 10.1109/LAWP.2016.2518746.

[132] Li Yang et al. "A novel conformal RFID-enabled module utilizing inkjet-printed antennas and carbon nanotubes for gas-detection applications". In: *IEEE Antennas and Wireless Propagation Letters* 8 (2009). ISSN: 15361225. DOI: 10.1109/LAWP.2009.2024104.

[133] Hattan F. Abutarboush and Atif Shamim. "Conformal and green electronics: A wideband inkjet printed antenna on paper substrate". In: *2013 7th European Conference on Antennas and Propagation, EuCAP 2013*. 2013.

[134] Maggie Yihong Chen et al. "Conformal Ink-Jet Printed C-Band Phased-Array Antenna Incorporating Carbon Nanotube Field-Effect Transistor Based Reconfigurable True-Time Delay Lines". In: *IEEE Transactions on Microwave Theory and Techniques* 60.1 (2011). DOI: 10.1109/TMTT.2011.2173209.

[135] Rod Waterhouse. *Printed Antennas for Wireless Communications*. Wiley, 2007.

[136] Toni Björninen et al. *Advances in Antenna Designs for UHF RFID Tags Mountable on Conductive Items*. Tech. rep. 1. 2014. DOI: 10.1109/MAP.2014.6821761.

[137] Hongli Zhu et al. "A gravure printed antenna on shape-stable transparent nanopaper". In: *Nanoscale* 6.15 (2014). ISSN: 20403372. DOI: 10.1039/c4nr02036g.

[138] Ravina Singh, Eric Singh, and Hari Singh Nalwa. "Inkjet printed nanomaterial based flexible radio frequency identification (RFID) tag sensors for the internet of nano things". In: *RSC Advances* 7.77 (Oct. 2017), pp. 48597–48630. ISSN: 20462069. DOI: 10.1039/C7RA07191D.

[139] A. Ali Babar et al. "Inkjet-printable UHF RFID tag antenna on a flexible ceramic-polymer composite substrate". In: *IEEE MTT-S International Microwave Symposium Digest*. 2012. DOI: 10.1109/MWSYM.2012.6259566.

[140] Masaya Nogi et al. "Foldable nanopaper antennas for origami electronics". In: *Nanoscale* 5.10 (2013). ISSN: 20403372. DOI: 10.1039/c3nr00231d.

[141] Matthew Giorgis Anderson et al. "Ultralow-power radio frequency beamformer using transmission-line transformers and tunable passives". In: *IEEE Microwave and Wireless Components Letters* 29.2 (2019). ISSN: 15311309. DOI: 10.1109/LMWC.2018.2886628.

[142] Gaetano Marrocco. "The art of UHF RFID antenna design: Impedance-matching and size-reduction techniques". In: *IEEE Antennas and Propagation Magazine* 50.1 (Feb. 2008), pp. 66–79. ISSN: 10459243. DOI: 10.1109/MAP.2008.4494504.

[143] Ruo Zhou Li et al. "Direct writing on paper of foldable capacitive touch pads with silver nanowire inks". In: *ACS Applied Materials and Interfaces* 6.23 (2014). ISSN: 19448252. DOI: 10.1021/am506987w.

[144] Md Taibur Rahman et al. "Microscale additive manufacturing and modeling of interdigitated capacitive touch sensors". In: *Sensors and Actuators, A: Physical* 248 (2016). ISSN: 09244247. DOI: 10.1016/j.sna.2016.07.014.

[145] Aaron D. Mazzeo et al. "Paper-based, capacitive touch pads". In: *Advanced Materials* 24.21 (June 2012), pp. 2850–2856. ISSN: 09359648. DOI: 10.1002/ADMA.201200137.

[146] Christopher H Fry and Stephen EM Langley. *ION-SELECTIVE ELECTRODES FOR BIOLOGICAL SYSTEMS*. Harwood Academic Publishers, 2005, pp. 81–93. ISBN: 9058231070.

[147] Carol A Clausen. "Wood Handbook, Chapter 14: Biodeterioration of Wood". In: (2010).

[148] C. Bauer-Reich et al. "An Investigation of the Viability of UHF RFID for Subsurface Soil Sensors". In: *IEEE*. June 2014, p. 638. ISBN: 9781479947744.

[149] Jeff Frolik et al. "Effects of Soil Characteristics on Passive Wireless Sensor Interrogation". In: *IEEE Sensors Journal* 18.8 (Apr. 2018), pp. 3454–3460. ISSN: 1530437X. DOI: 10.1109/JSEN.2018.2810132.

[150] H. R. Bogena et al. "Hybrid Wireless Underground Sensor Networks: Quantification of Signal Attenuation in Soil". In: *Vadose Zone Journal* 8.3 (Aug. 2009), pp. 755–761. ISSN: 15391663. DOI: 10.2136/vzj2008.0138.

[151] Martti T. Hallikainen et al. "Microwave Dielectric Behavior of Wet Soil-Part I: Empirical Models and Experimental Observations". In: *IEEE Transactions on Geoscience and Remote Sensing* GE-23.1 (1985), pp. 25–34. ISSN: 15580644. DOI: 10.1109/TGRS.1985.289497.

[152] Rafael Aroca et al. "Application of Standard EPC/GEN2 UHF RFID Tags as Soil Moisture Sensors". In: MDPI AG, Nov. 2016, p. 10. DOI: 10.3390/ecsa-3-s5001.

[153] Siyu Li and Hongju Gao. "Propagation characteristics of 2.4GHz wireless channel in cornfields". In: *International Conference on Communication Technology Proceedings, ICCT*. 2011, pp. 136–140. ISBN: 9781612843070. DOI: 10.1109/ICCT.2011.6157849.

[154] Z Li, N Wang, and T Hong. "RF Propagation Patterns at 915 MHz and 2.4 GHz Bands for in-field Wireless Sensor Networks". In: *Transactions of the ASABE* 56.2 (2013), pp. 787–796. ISSN: 2151-0032.

[155] Felipe P. Correia et al. "Path loss modeling at UHF band for Wireless Sensor Network deployment in a vineyard". In: *2014 31th URSI General Assembly and Scientific Symposium, URSI GASS 2014*. Institute of Electrical and Electronics Engineers Inc., Oct. 2014. ISBN: 9781467352253. DOI: 10.1109/URSIGASS.2014.6929677.

[156] Yongkun Sui et al. "Controlled Biodegradation of an Additively Fabricated Capacitive Soil Moisture Sensor". In: (2021). DOI: 10.1021/acssuschemeng.0c07615.

[157] Jan M. Rabaey. "The Human Intranet–Where Swarms and Humans Meet". In: *IEEE Pervasive Computing* 14.1 (Jan. 2015), pp. 78–83. ISSN: 1536-1268. DOI: 10.1109/MPRV.2015.20. URL: http://ieeexplore.ieee.org/document/7030200/.

[158] Morteza Amjadi et al. *Stretchable, Skin-Mountable, and Wearable Strain Sensors and Their Potential Applications: A Review*. 2016. DOI: 10.1002/adfm.201504755.

[159] Matteo Stoppa and Alessandro Chiolerio. *Wearable electronics and smart textiles: A critical review*. 2014. DOI: 10.3390/s140711957.

[160] Yasser Khan et al. "Monitoring of Vital Signs with Flexible and Wearable Medical Devices". In: *Advanced Materials* 28.22 (June 2016), pp. 4373–4395. ISSN: 09359648. DOI: 10.1002/adma.201504366. URL: http://doi.wiley.com/10.1002/adma.201504366.

[161] P. Escobedo et al. "Flexible Passive near Field Communication Tag for Multigas Sensing". In: *Analytical Chemistry* 89.3 (2017). ISSN: 15206882. DOI: 10.1021/acs.analchem.6b03901.

[162] Ralf Zichner and Reinhard R. Baumann. "Roll-to-roll screen printed radio frequency identification transponder antennas for vehicle tracking systems". In: *Japanese Journal of Applied Physics* 52.5 PART 2 (2013). ISSN: 00214922. DOI: 10.7567/JJAP.52.05DC24.

[163] Alexander Ilic, Thorsten Staake, and Elgar Fleisch. "Using sensor information to reduce the carbon footprint of perishable goods". In: *IEEE Pervasive Computing* 8.1 (2009). ISSN: 15361268. DOI: 10.1109/MPRV.2009.20.

[164] Rebecca Angeles. "Rfid technologies: Supply-Chain applications and implementation issues". In: *Information Systems Management* 22.1 (2005). ISSN: 10580530. DOI: 10.1201/1078/44912.22.1.20051201/85739.7.

[165] James C. Chen et al. "Warehouse management with lean and RFID application: A case study". In: *International Journal of Advanced Manufacturing Technology* 69.1-4 (2013). ISSN: 14333015. DOI: 10.1007/s00170-013-5016-8.